$\pi^{\pm} - h^{\pm}$ correlation in $d - Au$ and $p - p$ collisions at $\sqrt{s_{NN}} = 200$ GeV

Jiangyong Jia,Brian Cole

October 18, 2004

Abstract

We present the study of jet fragmentation properties in $d - Au$ and $p - p$ collisions through two particle correlation technique. Azimuth correlation functions are built by correlating non-identified charged particles ($0.4 < p_T < 5$ GeV/c) with their associated high p_T pions. From these correlation functions, we extract the jet width, P_{out} and x_E distribution. Mean values are then deduced for the parton transverse momentum k_T and for jet fragmentation momentum j_T. Results are compared between $d - Au$ and $p - p$; no significant differences are observed within the uncertainties.

Contents

1 Introduction

The two particle correlation method allows one to measure the properties of the di-jet production. The spread of the hadrons around the jet axis and the relative orientation of the two jets can be characterized by the jet fragmentation momentum j_T and the di-jet transverse momentum k_T; the jet fragmentation function can be accessed by measuring the conditional yield.

In previous analysis note[1], we have shown that the following cut is required to select background free charged pions in PbSc,

- $quality == 31 || quality == 63$

- $fabs(pc3sdz) < 3 \&\& fabs(pc3sd\phi) < 3 \&\& fabs(emcsdz) < 3 \&\& fabs(emcsd\phi) < 3$

- $N_{PMT} \geq 0$

- $e > 0.3 + 0.15 p_T$

- $prob < 0.2$

As we shall discuss in section, this cut can be generalized to include PbGl, and also should be slightly different for the three types of nanoDSTs, i.e. CNT_Photon, CNT_Electron and CNT_Minbias, in order to maximize the trigger statistics.

By combining the trigger pion and low p_T charged hadrons, we build the correlation functions and extract the conditional yield according to the procedures described in analysis note 312[2]. The conditional yield is closely related to the jet fragmentation function, while the structure in the correlation function carries information on the kinematics of the underlying parton-parton scattering, k_T, and of the jet fragmentation process, j_T. The conditional yield extraction is discussed in Section, there we also developed a statistical method to measure the P_{out} and x_E distribution. To deduce the j_T and k_T, we used the framework discussed in analysis note[3]. The j_T, k_T results and limitations are discussed in Section.

Some of the preliminary results from this analysis was presented in Quark Matter 2004 [12]. For completeness, we include it as an appendix.

2 Cuts

2.1 Trigger particle selection

2.1.1 dispersion cut

The prob variable was not tuned for PbGl, so we have to use a different variable. One of such variable is the dispersion variable, which characterize the spread of the towers belonging to the same cluster: $dispz$ in the z direction, and $dispy$ in the azimuth direction. We defined a normalized dispersion variable $dispn$,

$$dispn = \frac{max(dispz, dispy)}{\sigma_{disp}} \tag{1}$$

where σ_{disp} is calculated from the angle of incidence ϕ at the EMCal panel according to

$$\sigma_{disp} = 0.27 - 0.0145\phi + 0.00218\phi^2 \tag{2}$$

In principle, the dispersion variables can be used at both the PbSc and PbGl. In Fig.1, the p_T distribution of pion candidates selected by $prob < 0.2$ or $disp > 0.4$ are shown in the left panel for PbSc from CNT_Electron. One notice that both cuts gives comparable results, with about factor of 3 rejection around 6 GeV/c. In the left panel, we show the dispersion cut at the PbGl. The same cut $disp > 0.6$ only have factor of 2 rejection at 6 GeV/c. That means that the dispersion cut is more effective for rejecting background at PbSc than at PbGl. For that reason, we also show the distribution with a stronger $dispn$ cut in Fig.1b: $dispb > 0.6$. This cut is comparable to the $dispb > 0.4$ cut at PbSc.
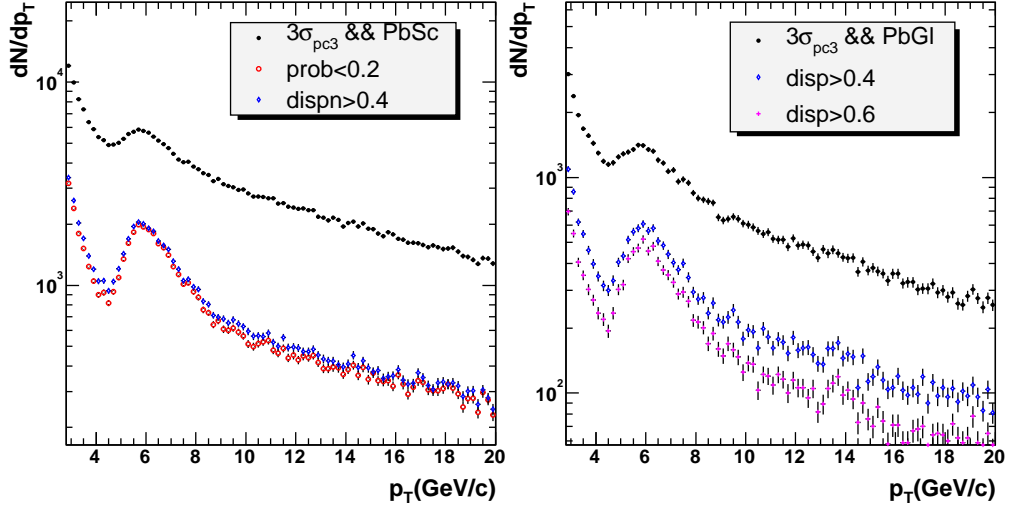

Figure 1: a). Pion candidates in Electron triggered data(CNT_Electron) at PbSc with only $n0 > 0$ and 3 σ matching cut at PC3 (black), with $prob < 0.2$ cut(red) and with $dispn > 0.4$(blue) cut. b) Pion candidates in Electron triggered data(CNT_Electron) at PbGl with only $n0 > 0$ and 3 σ matching cut at PC3 (black), $dispn > 0.4$(blue) cut and with $dispn > 0.6$(magenta) cut.

Fig.2 shows the azimuth distribution of all pion candidate between 5 to 8 GeV/c with $dispn > 0.4$. Since most of the background tracks are rejected with this cut with in this p_T range, thee azimuth distribution reflects mostly the distribution of the signals. Fig.2 indicates that there is no significant difference in the pion efficiency between PbSc and PbGl.

We repeat the same study for CNT_Photon nanodst. The results are shown in Fig.3,Fig.4. Comparing the two panels in Fig.3, we notice that the background level in PbSc is less than PbGl. Also in the left panel of Fig.4, the density of pion candidates in PbGl is much less than that for PbSc. All these, we believe, are caused by the fact that hadronic shower in PbGl is weaker than that in PbSc. Since CNT_Photon requires a fairly large energy cut in the Level-1. The pion candidates firing the trigger at PbGl are greatly reduced. The relative less shower energy for charged pions at PbGl also means relatively more conversion
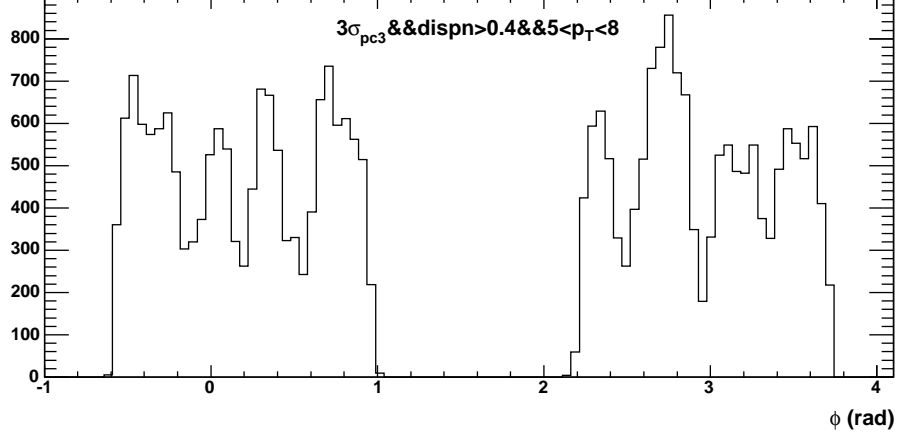
Figure 2: The azimuth distribution of pion candidates with $dispn > 0.4$ from 5 to 8 GeV/c in p_T.

background, because the electron and photons always deposit their full energy in either PbSc or PbGl.
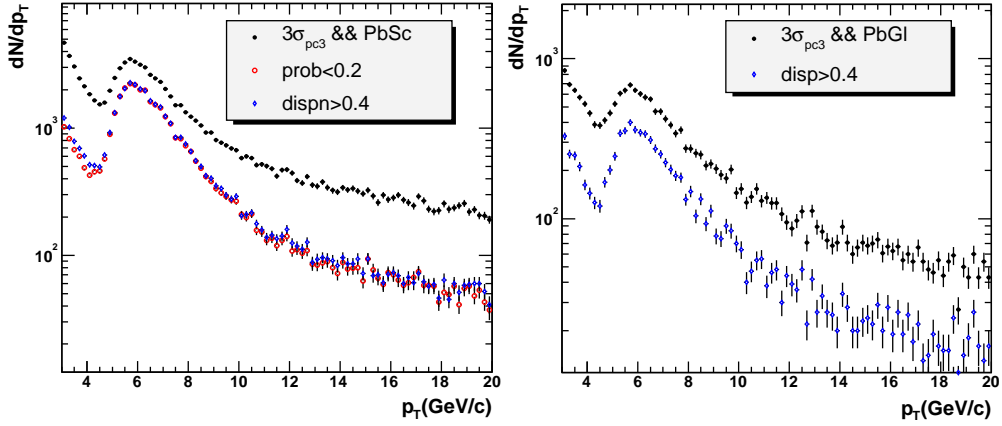

Figure 3: a). Pion candidates in photon triggered data(CNT_Photon) at PbSc with only $n0 > 0$ and 3 σ matching cut at PC3 (black), with $prob < 0.2$ cut(red) and with $dispn > 0.4$(blue) cut. b) Pion candidates in photon triggered data(CNT_Photon) at PbGl with only $n0 > 0$ and 3 σ matching cut at PC3 (black) and $dispn > 0.4$ cut (blue).

Based on this study, we decided to use $dispn > 0.6$ to select charged pions at PbGl.

2.1.2 quality cut

In our current analysis, we have expanded the criteria on selecting the associated particles to include also the low quality tracks(those tracks that were reconstructed at only one x layer). The worsening of the momentum resolution is not a problem because of the much shallower jet fragmentation spectra.
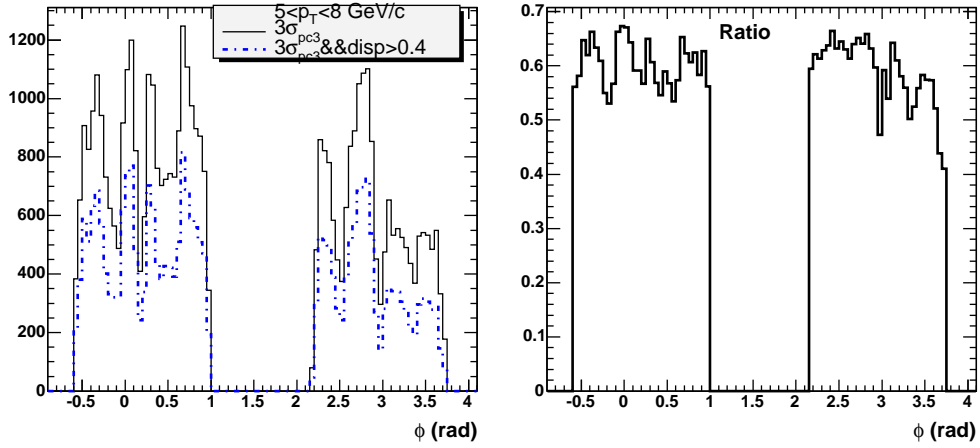
5

Figure 4: a) The azimuth distribution of pion candidates with $n0 > 0,3\sigma$ PC3 matching cut(black) and with in addition $dispn > 0.4$ cut(blue) from 5 to 8 GeV/c in p_T. b) The ratio of blue to black as function of azimuth.

We can use Fig.67 as an example, it can be parameterized by a powerlaw function as shown by Fig.5. Also shown in blue is the inclusive charged hadron spectra. One clearly see that the CY spectra is much more flatter than that for inclusive charged hadrons. We can use this spectra shape to study the momentum smearing effect. We know from RUN2 analysis that the momentum resolution of high quality track is about 1% and the low quality is about 3%[1]. By smearing the fitted spectra shape by the 3% momentum resolution according to

$$\frac{\Delta p}{p} \simeq 0.03 \times p \tag{3}$$

We obtain a output spectra, the deviation of the output spectra to the fitted spectra shall reflects the smearing effect. Fig.6 shows the results of such study. Our conclusion from this study is that the momentum resolution effect on low quality track in the jet fragmentation function is negligible due to the much more flatter spectra shape comparing that for the inclusive spectra.

Due to the same reason, the problem of high p_T background at $p_T > 5$ GeV/c is less an issue. We know from previous dAu [4] and pp [5] analysis that the amount of background at 5 GeV/c is about 30% of the inclusive spectra. Since most of the background comes from low p_T, the high p_T level at high p_T depends mostly on the yield at low p_T. So from Figure.67, the amount background would be only a few percent at 5 GeV/c. However, the feed down background background is contributed from all p_T ranges, and the amount of background would be more sensitive to the actual CY spectra shape. This background comes mostly from K_s and Λ, and is less than 5% independent of p_T.

By including the low quality tracks for the associated particles, we gains about 25% more pairs, and the acceptance becomes more uniform. We can also include the low quality tracks in the trigger selection. The reason is because, we use the RICH to select high p_T pions, it serves as natural cut off for the momentum smearing contribution coming from

---

[1]this can also easily obtain by looking at the width of the DC α angle distribution from zero field data
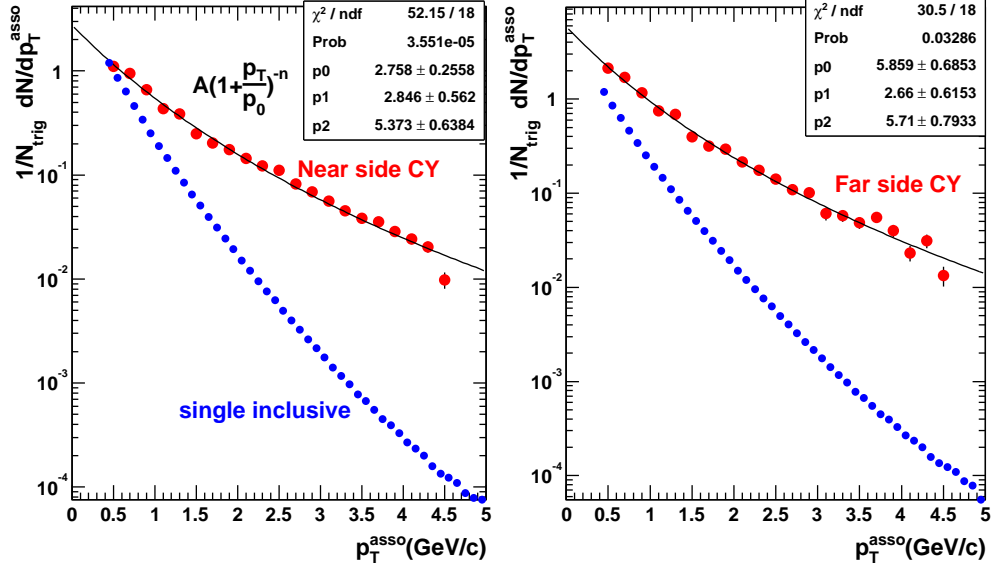
Figure 5: Parameterization of the near side CY (left panel) and far side CY(right panel) together with the inclusive charged hadron yield in $d - Au$ minimum bias collisions.
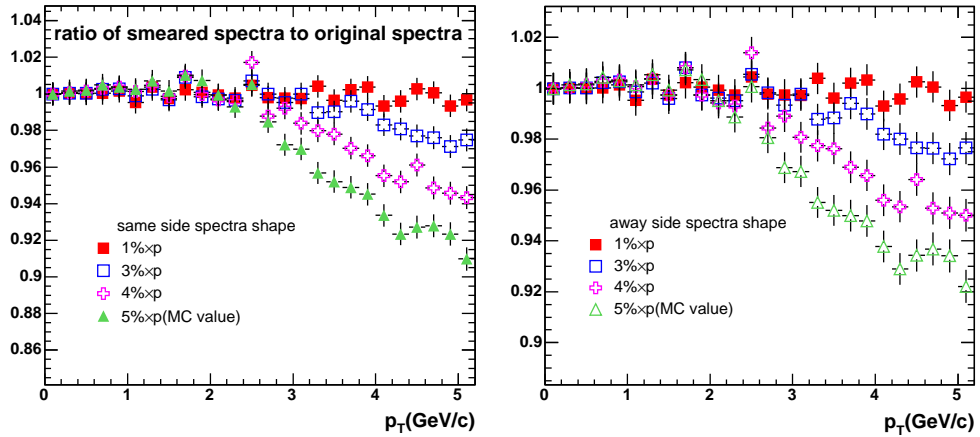

Figure 6: The ratio of the smeared spectra to the input spectra. The input spectra in the left panel is the fit to the near side fragmentation spectra; The input spectra in the right panel is the fit to the away side fragmentation spectra.

$p_T < 5$ GeV/c. In other words, although a low pt track can become > 5 GeV/c track due to momentum smearing, it will be rejected by requiring a RICH hit. So only the smearing at $p_T > 5$ GeV/c where the pion start to fire RICH becomes important. Since the p_T spectra become very flat at $p_T > 5$ GeV/c due to the power law tail, the smearing effect is not a big effect. In this analysis, we always study the results for with and without low quality tracks for the trigger pion. Since the difference is small between the two, we include low quality tracks for better statistical error.

2.1.3 Combining the statistics from 3 nanodsts

After obtaining the background free high p_T pions, we study their correlations with low p_T charged hadrons. The advantage with correlation analysis is that, one does not need to known exactly the efficiency in triggering on the high p_T pion. However, if an event contains a high p_T pion but it is fired by a different particle, then this event can not be used in order to reduce trigger bias. As shown in Fig. 7, both Electron trigger and Photon trigger can catch a significant fraction of high p_T pions. The fact that the ratio of electron triggered pions to the total pions is close to 1, indicates that almost all pions candidates does fires the trigger.

However, Fig. 7 indicates that only a fraction of pion candidates in CNT_Electron fires the photon trigger. This fraction is quite high, it goes from about 60% around 6 GeV/c to about 80% around 15 GeV/c. Similarly we also found that only a fraction of pion candidates in CNT_Photon fires the electron trigger as indicated in Fig.8, but this overlap is somewhat smaller than CNT_Electron. So combining the two triggered data can greatly increase the statistics for correlation analysis.
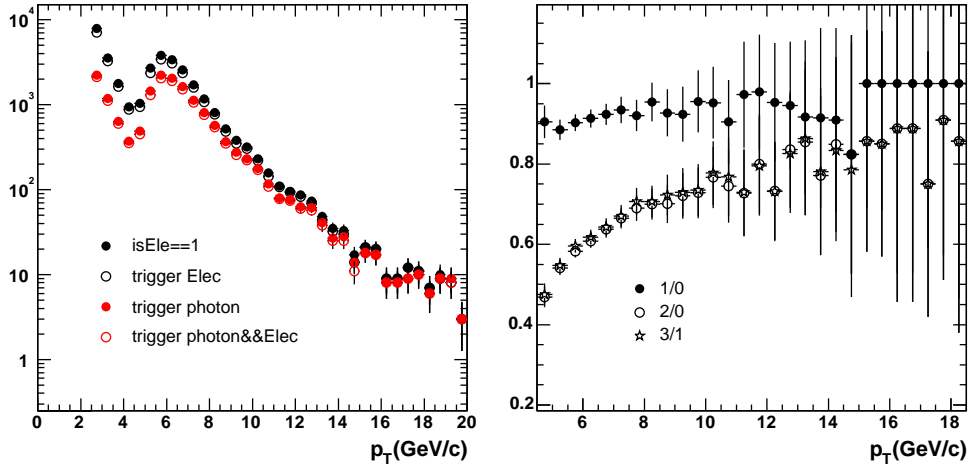

Figure 7: a). Pion candidates in Electron triggered data(CNT_Electron) b). The fraction of high p_T pions that actually fire the trigger(close marker), and the fraction that fired the Photon trigger.

In Fig. 9left panel, we show the additional pion statistics one gains by including three gamma triggered events (in open markers). The gain in statistics relative to Electron triggered data is plotted in the right panel(the open markers). The net gain is about 70% around 5 GeV/c and decreases to 40% at $p_T > 10$ GeV/c.

If we use sector number to represent the PbGl and PbSc , $sec = 0, 1$ for PbGl and $2 \leq sec \leq = 7$ for PbSc. The final cuts we use for selecting trigger charged pions are:

- $N_{PMT} \geq 0$

- $quality > 7$

- $fabs(pc3sdz) < 3 \&\& fabs(pc3sd\phi) < 3 \&\& fabs(emcsdz) < 3 \&\& fabs(emcsd\phi) < 3$
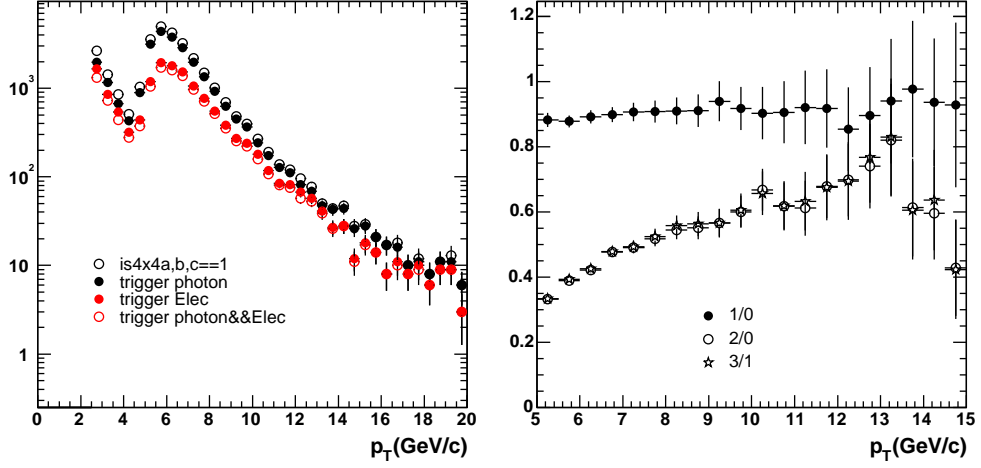
8

Figure 8: a). Pion candidates in Photon triggered data(CNT_Photon). b). The fraction of high p_T pions that actually fire the trigger(close marker), and the fraction that fired the Electron trigger.
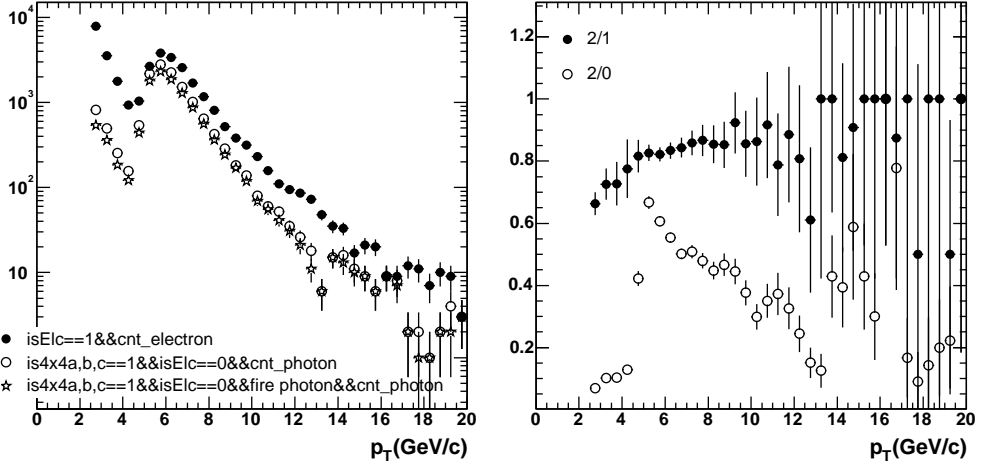

Figure 9: a). Pion statistics from CNT_Electron only(solid marker), additional high p_T pions in CNT_Photon that is not included in CNT_Electron(open circle) and additional high p_T pions in CNT_Photon that actually fires the Gamma trigger(open star). b). Trigger bias for the additional pions(open star/open circle), and the additional statistics relative to CNT_Electron statistics(open star/solid marker).

- $(prob < 0.2\&\&sec > 1)||(dispn > 0.6\&\&sec < 2)$

- 1. $e > 0.3 + 0.15p_T$ for CNT_Photon
  2. $p_T \leq 8||(p_T > 8\&\&p_T \leq 12\&\&e > 0.3 + 0.1p_T)||(p_T > 12\&\&e > 0.3 + 0.15p_T)$ for CNT_Electron or CNT_Minbias

Notice that we have used a p_T dependent energy cut for CNT_Photon. This is because a fairly strong energy cut has been applied at Level-1. Although that energy cut (2.1 or

2.7 GeV) is constant and also suffer from pedestal effect. It is a fairly strong rejection on background at low p_T region. And the offline sliding cut is only needed at fairly high p_T.

2.2 Associated particle selection

In this analysis, the associated particles are chosen to includes all charged hadrons below the trigger threshold $p_T < 5GeV/c$.

- $quality > 7$

- $fabs(pc3sdz) < 3\&\&fabs(pc3sd\phi) < 3$

We have chosen to include also the low quality tracks in our analysis, this will not cause a big background or momentum smearing problem because the associated particle spectra is much less steeper than the inclusive spectra as we will see in section

2.3 Pair cuts

In correlation analysis, the pair efficiency in the foreground distribution and mixed distribution is different for close pairs[3]. These differences are mainly due to two track resolution, ghost etc, which distorts the pair distribution at small angles which can not be reproduced by event mixing. In general, pair cuts are used to cut out those regions in $\Delta\phi$ and $\Delta\eta$ for which the differences between foreground and mix distribution are large.

Typically, the following pair cuts was avocated[6, 7]:

- $|\Delta\phi| < 0.008\&\&\Delta pc1 > 7\&\&\Delta pc3 > 15$

This cut was developed for $Au - Au$ collisions and was suppose to reject the ghost tracks in the DC and close tracks that shares the PC1 or PC3 hits. For ghost removal, 8 mili-radian is too big. I believe the window should be determined by the two track resolution which is $150\mu m$ which corresponds to 0.1 mili-radian. For low quality tracks it could happen that the one track can be reconstructed as two low quality tracks in high multiplicity environment, but 1 mili radian cut should be sufficient. In peripheral $Au - Au$, $d - Au$ or $p - p$ collisions where the detector occupancy is low, the cuts on PC1 and PC3 can also be loosen substantially. Recall that the purpose of PC1 PC3 pair cuts is to remove the hit sharing effects, because hit sharing is believe to reduce the tracking efficiency. But in fact if the hits are not shared at either PC1 or PC3, the track would be correctly reconstructed. So this cut can be loosen to $\Delta pc1 > 7||\Delta pc3 > 15$.

Fig. 10 shows the loss in pair acceptance estimated for the default pair cuts. This is done by applying pair cuts on the mixing distribution, then the ratio between with and with out pair cut gives the pair efficiency. There is significant efficiency loss at small $\Delta\phi$ and small $\Delta\eta$, upto 30%. Fig. 11 shows the relative pair efficiency for $\Delta pc1 > 7\&\&\Delta pc3 > 15$ only. The strip along $\Delta\phi$ around $\Delta\phi = 0$ disappears, but the spike around $\Delta\phi = 0$ and $\Delta\eta = 0$ still remain. When we requires $\Delta pc1 > 7||\Delta pc3 > 15$ condition, the relative efficiency loss is reduce to less than 10% as indicated by Fig. 12. So in our analysis, the pair cut is:
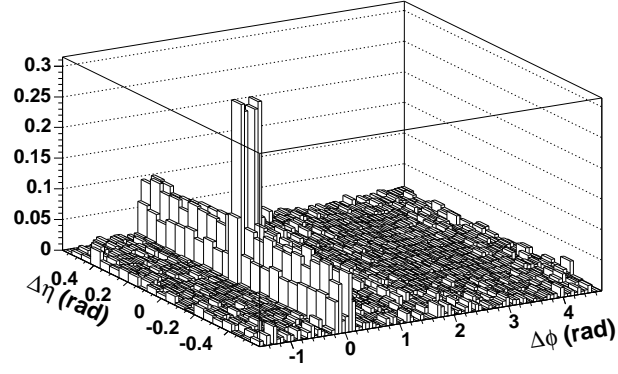
- $\Delta pc1 > 7||\Delta pc3 > 15$

Figure 10: Relative pair efficiency loss as function of $\Delta\phi$ and $\Delta\eta$ with a pair cut of $|\Delta\phi| < 0.008\&\&\Delta pc1 > 7\&\&\Delta pc3 > 15$.
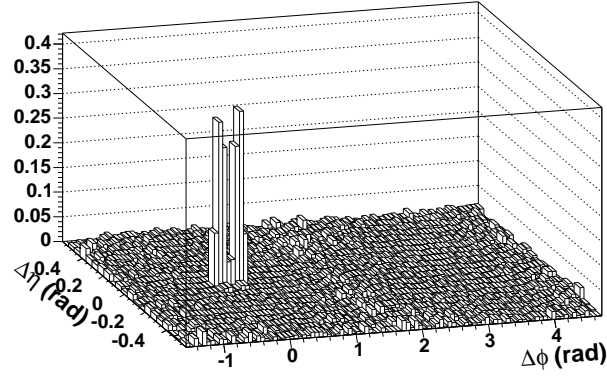

Figure 11: Relative pair efficiency loss as function of $\Delta\phi$ and $\Delta\eta$ with a pair cut of $\Delta pc1 > 7\&\&\Delta pc3 > 15$.

2.4 The p_T ranges for trigger and associated particles

In order to perform a detailed study of the jet fragmentation and also due to limited statistics, we divide the trigger and associated particles into many p_T bins. We made 2 type of studies, in the first study, we chose coarse bins for trigger particles and fine bin for associated particle

- Trigger 5 - 10, 10-16, 5-16 GeV/c.

- associated 0.4-0.6, 0.6-0.8, 0.8-1.0, 1.0-1.5, 1.5-2.0, 2-2.5, 2.5-3.0, 3.0-4.0, 4.0-5.0, 3.0-4.5, 2.0-4.0 GeV/c.
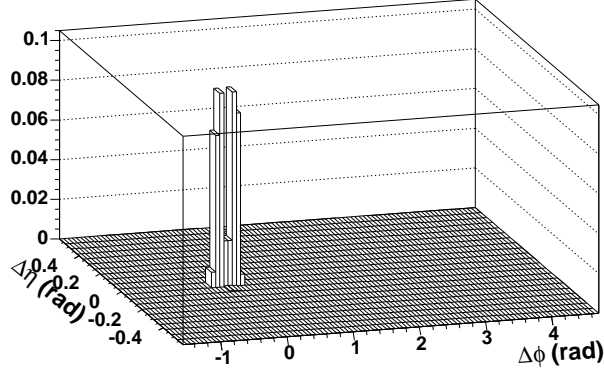
Figure 12: Relative pair efficiency loss as function of $\Delta\phi$ and $\Delta\eta$ with a pair cut of $\Delta pc1 > 7||\Delta pc3 > 15$.

This selection allows us to extract the fragmentation function and to study the p_T dependence of j_T.

In the second study, we chose fine bins for trigger particles and coarse bins for associated particles

- Trigger 5-6, 6-7, 7-8, 8-10, 10-12, 12-16 GeV/c.

- associated 0.4-0.6, 0.6-0.8, 0.8-1.0, 1.0-2.0, 2.0-3.0, 2-4.5, 3.0-4.5 GeV/c.

This selection allows us to study the scale dependence of the fragmentation function and to study the p_T dependence of k_T.

2.5 Effect of cuts on pair acceptance

Before jumping into extraction of physics quantities. Let's look in some details on the event mixing. Fig. 13 shows the mix background $\Delta\phi$ distribution for seed1 and part1 selection. Clearly one see some structures in the mix distributions and the distribution are not symmetric around 0 and π. Presumably, there are two reasons for the irregularities. The asymmetry is caused by the fact the tracks are ordered in the nanoDSTs according to the momentum(as a result of the hough space search), which can be solved by randomize the sign of $\Delta\phi$. As shown by the cross marker in Fig. 13. The small structures are caused by the dead keystones in the DC. In fact, when one apply track quality cut for the partner tracks, the irregularities are magnified(see the lower 2 sets of curves) because the dead area is more sharp.

This effect can be better illustrated if one looks seed ϕ_{DC} dependence of $\Delta\phi$(Fig. 14) and $\Delta\phi_{DC}$(Fig. 15). Fig. 15 is plotted for positive and negative partner tracks separately. Clearly one can see that the holes in Fig. 15 is caused by DC dead area, which leads to almost doubled holes in Fig. 14 because the bend in the magnetic field are opposite for different charges.
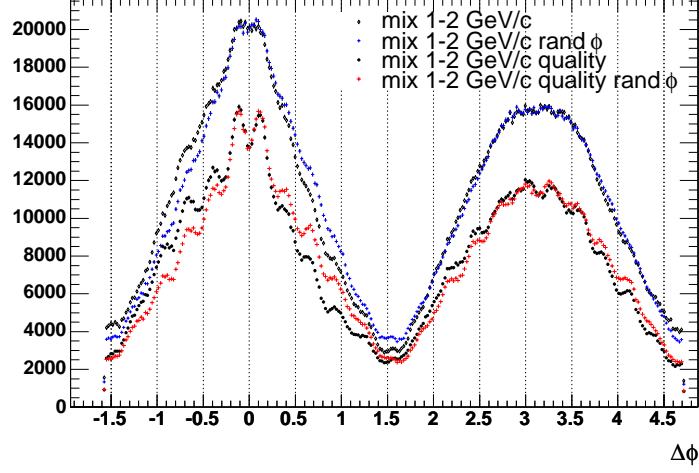
Figure 13: Mix background distribution for seed1 and partner tracks within 1-2 GeV/c. The black markers represents the $\Delta\phi$ distribution before randomization. The colored markers are after randomization. The top curves is for all quality partner tracks, the lower curves are for high quality partner tracks. The structures in the lower curves are caused by DC dead areas, which become much weaker if one use all quality tracks as shown by the top curves.
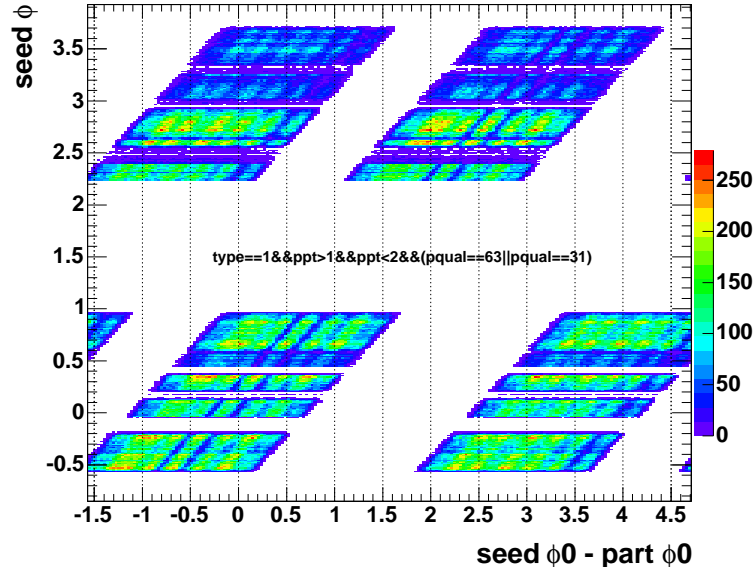

Figure 14: Trigger ϕ at Drift Chamber vs the $\Delta\phi$ at the vertex.

We can see that uniform acceptance is very important for correlation studies. Of cause, if there is any structures in the mix background it should also be there for the foreground, however, the structures will make the correlation function more prone to statistical fluctuations etc. That is also one of the reason to relax the quality cut on the DC tracks in addition
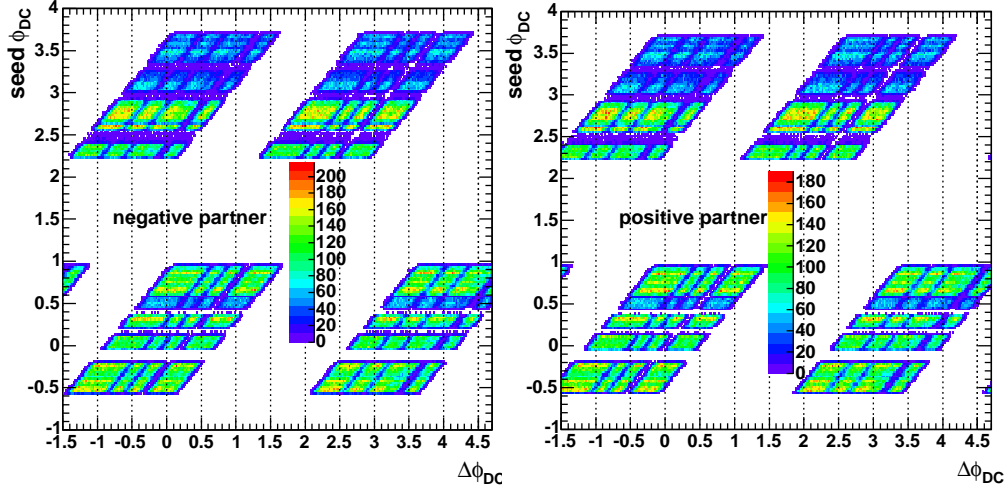
Figure 15: Trigger ϕ at Drift Chamber vs the $\Delta\phi$ at the Drift Chamber. left is for negative partner tracks, right is for positive partner tracks.

to gaining more statistics.

3 Correlation function

As discussed in analysis note 313, the correction function in our analysis is constructed as

$$C(\Delta\phi, \Delta\eta) \;\; = \;\; \frac{\frac{1}{N_{trigs}}\frac{dN^{fg}}{d\Delta\phi d\Delta\eta}}{\frac{1}{N_{events}}\frac{dN^{mix}}{d\Delta\phi d\Delta\eta}} \tag{4}$$

in two dimension and

$$C(\Delta\phi) \;\; = \;\; \frac{\frac{1}{N_{trigs}}\frac{dN^{fg}}{d\Delta\phi}}{\frac{1}{N_{events}}\frac{dN^{mix}}{d\Delta\phi}} \tag{5}$$

in one dimension. N_{trigs} is the total number of trigger particles. N_{events} is the total number of mixed events, which is the product of the number of triggers and the number of mixed events per trigger:

$$N_{events} = N_{trigs} \times N_{mix-per-trigger} \tag{6}$$

Correlation function is the intermediate step towards the conditional yield. In some sense, it's normalization is arbitrary. Our definition has the advantage that it is straight forward to determine the background level. If the background level in foreground and mix is equal, the value of the correlation function around $\pi/2$ would be one (assuming jet signal at $\pi/2$ is negligible).

3.1 2D correlation function

Fig.16 shows the foreground distribution (left panel), mixing distribution (middle) and correlation function(right) as function of $\Delta\phi$ and $\Delta\eta$. We notice a few things: 1) the mixing distribution has a shoulder structures, instead of a triangle. The reason is not clear. 2) There is a distinctive jet correlation peak around $\Delta\phi = 0$ and $\Delta\eta = 0$, the away side peaks around $\Delta\phi = \pi$, but is almost flat along the $\Delta\eta$. 3) CF has large statistical fluctuation at large $\Delta\eta$.
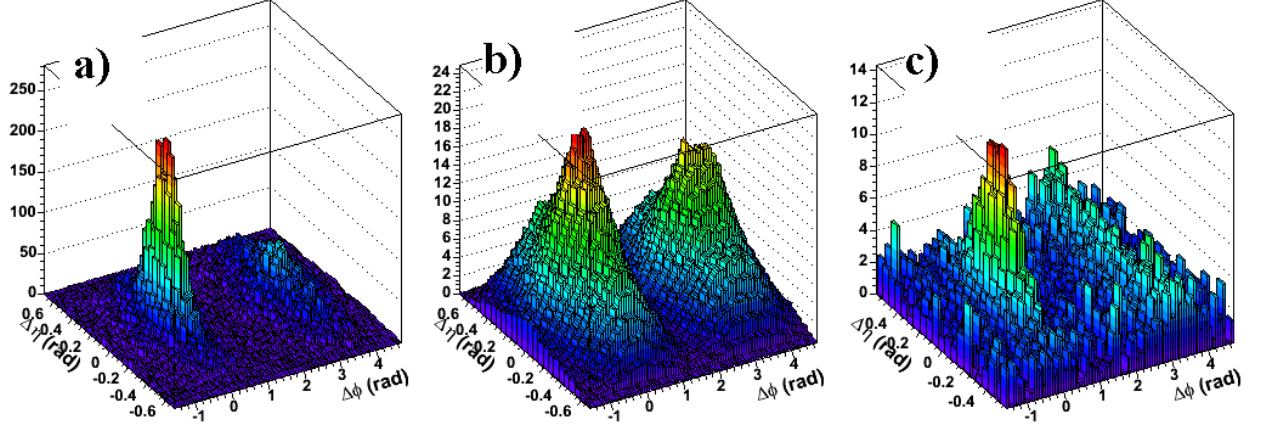

Figure 16: The foreground distribution (left panel), mixing distribution (middle) and correlation function(right) as function of $\Delta\phi$ and $\Delta\eta$. The trigger tracks are charged pions between 5 and 10 GeV/c, the associated tracks are charged tracks above 1 GeV/c.

Fig.17 shows the projection of the 2D CF onto $\Delta\phi$ (left panel), onto $\Delta\eta$ for $|\Delta\phi| < 1.57$ (middle panel) and onto $\Delta\eta$ for $\Delta\phi > 1.57$ (right panel). The projection onto $\Delta\phi$ has no constraint on the range of $\Delta\eta$. The large fluctuation in the left panel comes from the integration at large $\Delta\eta$. We also noticed that the width in $\Delta\eta$(middle panel) is narrower than in $\Delta\phi$(near side peak in the left panel), the reason for this is under investigation.

Fig.18 shows the projection of the 2D CF onto $\Delta\phi$ for four different $\Delta\eta$ integration ranges: $|\Delta\eta| < 0.7$(top left),$|\Delta\eta| < 0.5$(top right), $|\Delta\eta| < 0.4$(bottom left) and $|\Delta\eta| < 0.3$(bottom right). Clearly, as one narrows the $|\Delta\eta|$ below 0.5, the fluctuation in the top left panel is reduced. The widths are consistent among the four panels. The near side yield changes very little as expected and the away side yield decreases almost linearly, the later is consistent with constant correlation strength in the away side.

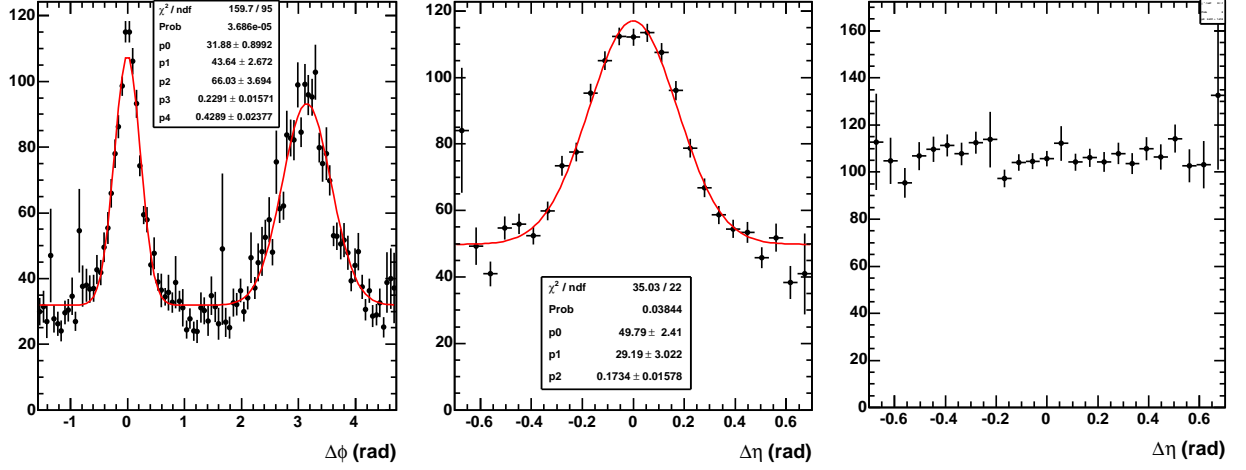Figure 17: The projection of the 2D CF onto $\Delta\phi$ (left panel), onto $\Delta\eta$ for $|\Delta\phi| < 1.57$ (middle panel) and onto $\Delta\eta$ for $\Delta\phi > 1.57$ (right panel). The trigger tracks are charged pions between 5 and 10 GeV/c, the associated tracks are charged tracks above 1 GeV/c.
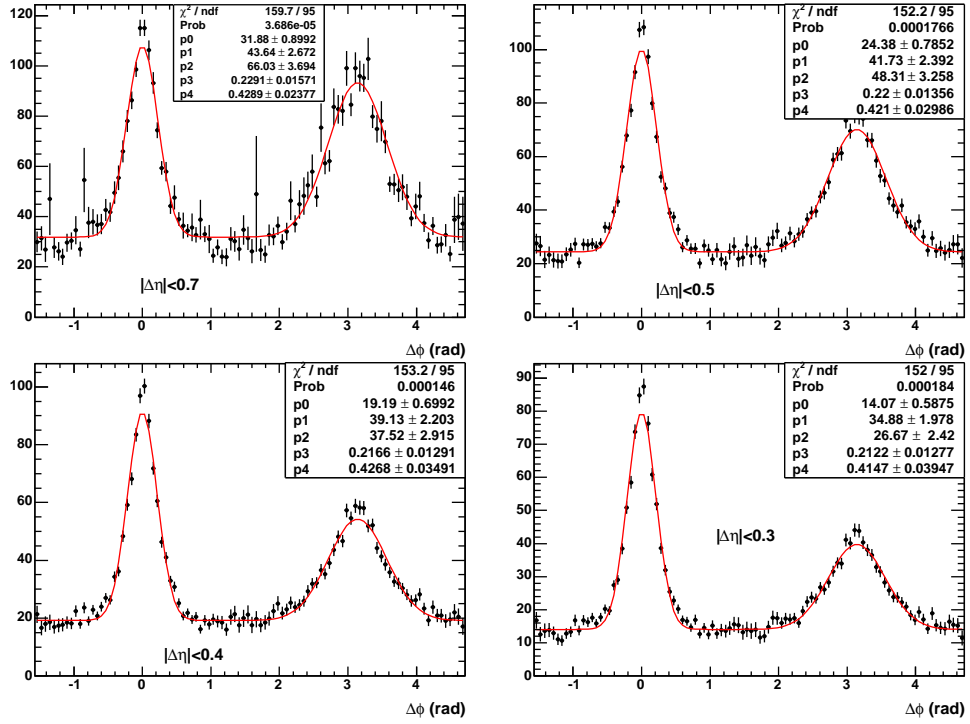

Figure 18: The projection of the 2D CF onto $\Delta\phi$ for four different $\Delta\eta$ integration ranges: $|\Delta\eta| < 0.7$(top left),$|\Delta\eta| < 0.5$(top right), $|\Delta\eta| < 0.4$(bottom left) and $|\Delta\eta| < 0.3$(bottom right).

16

3.2 1D correlation function

Similarly, the 1D correlation function defined according to Eq.5 is plotted in Fig.19. There are threes column of panels. In the left column, the top panel show the foreground (upper histogram) and mixed background(lower histogram) distributions and the bottom panel show the CF which is the ratio of the two. The red curve in the top panel is the a loglikelihood fit on the forground distribution using following function

$$fgr(\phi) = (p_0 + p_1 e^{-\frac{\phi^2}{2\sigma_N^2}} + p_2 e^{-\frac{(\phi-\pi)^2}{2\sigma_F^2}}) \times bkg(\phi) \tag{7}$$

where the integral of $bkg(\phi)$ is constrained by the mix background distribution. Here since we measure the background using event mixing technique, we assume the background is fixed in the fit. Using loglikelihood fit also treat the statistical error correctly in low statistic limits. The red curve in the bottom panel is the same fit function obtained from the fit in the top panel. The middle column (right column) basically are similar to the left panel except that they are for the 1D distribution in $\Delta\eta$ for $|\Delta\phi| < 1.57$ ($\Delta\phi > 1.57$). Similar to 2D correlation function, the shoulder structure shows up in $\Delta\eta$ around 0.4 and -0.4.
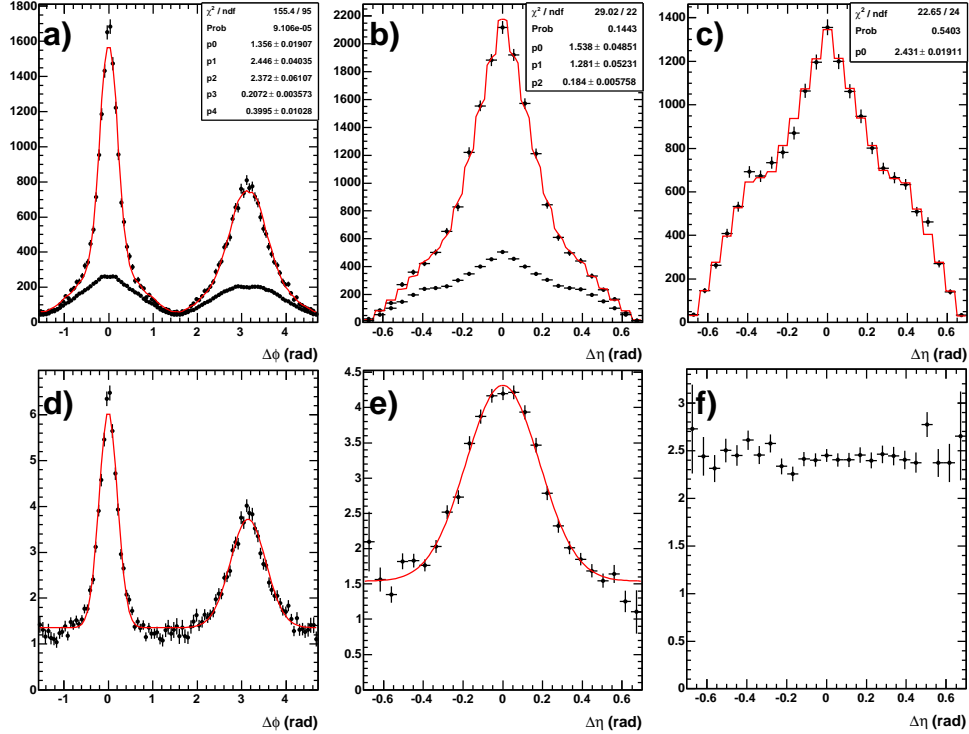

Figure 19: In the left column, the top panel show the foreground (upper histogram) and mixed background(lower histogram) distributions and the bottom panel show the CF which is the ratio of the two. The red curve on the top panel is simultaneous fit to both foreground and mix background. And the resulting double gauss function is also plotted in the bottom. The middle column (right column) basically are similar to the left panel except that they are for the 1D distribution in $\Delta\eta$ for $|\Delta\phi| < 1.57$ ($\Delta\phi > 1.57$).

17

4 Yield analysis

4.1 Conditional yield

The jet fragmentation function, $D(z)$ or $D(p_T)$, represents the associated yield per jet,

$$D(z) \quad = \quad \frac{1}{N_{jet}}\frac{dN_{asso}}{dz}, \qquad or \tag{8}$$

$$D(p_T) \quad = \quad \frac{1}{N_{jet}}\frac{dN_{asso}}{dp_T} \tag{9}$$

where

$$D(p_T) \quad = \quad \frac{1}{p_{T,jet}}D(z) \tag{10}$$

when the jet energy is fixed.

Two particle correlation requires at least two particle from the same jet. Their distribution can be described by the di-hadron fragmentation function,

$$D(z_1, z_2) = \frac{1}{N_{jet}}\frac{d^2N_h}{dz_1 dz_2} \tag{11}$$

The conditional fragmentation function, where the p_T of one particle is fixed, can be written as,

$$\frac{D(z_1, z_2)}{D(z_1)} = \frac{1}{N_{jet}}\frac{d^2N_h}{dz_1 dz_2}\bigg/ \frac{1}{N_{jet}}\frac{dN_h}{dz_1} \tag{12}$$

The two particle correlation method extract jet signal results from the correlation between two particles from the same jet, it measures the associated yield per trigger particle or conditional yield (CY),

$$CY(x_E) \quad = \quad \frac{1}{N_{trig}}\frac{dN_h}{dx_E} \approx z_{trig}D(z), \quad where \tag{13}$$

$$x_E \quad = \quad \frac{z}{z_{trig}} \tag{14}$$

clearly, the CY is closely related to the conditional fragmentation function.

$$\frac{D(z_1, z_2)}{D(z_1)} = CY(z_1, z_2) \tag{15}$$

In analysis note 313, we derived the formula for the conditional yield,

$$\frac{1}{N_a}\left(\frac{dN_0^{fg}}{d\Delta\phi} - \lambda\frac{dN_0^{mix}}{d\Delta\phi}\right) \quad = \quad \frac{1}{N\prime_a\epsilon_{asso}}\frac{dN^{fg}/d\Delta\phi - \lambda dN^{mix}/d\Delta\phi}{\frac{\Omega_{\Delta\phi}dN^{mix}/d\Delta\phi}{\int d\Delta\phi dN^{mix}/d\Delta\phi}} \tag{16}$$

where

$$\epsilon_{asso} = A_{\Delta\eta}K\prime_{ab}\epsilon_{single}\frac{k^{fg}(\Delta\phi)}{k^{mix}(\Delta\phi)} \tag{17}$$

$$A_{\Delta\eta} = \frac{I_\eta}{R_{\Delta\eta}\Omega_{\Delta\eta}} = \frac{\int d\Delta\eta Acc(\Delta\eta)jet\_shape(\Delta\eta)}{\int d\Delta\eta Acc(\Delta\eta)} \tag{18}$$

$A_{\Delta\eta}$ is the total fraction of the jet yield in limited $\Delta\eta$ window. It can be divided into three parts. $I_\eta = \frac{\Omega_{\Delta\eta}}{\int d\Delta\eta Acc(\Delta\eta)}$ is the normalization factor in $\Delta\eta$ (the inverse of average pair efficiency). Since pair acceptance Acc is almost triangle, i.e

$$Acc(\Delta\eta) \propto \frac{\Omega_{\Delta\eta} - 2\Delta\eta}{\Omega_{\Delta\eta}}, \tag{19}$$

I_{eta} is very close to 2. $K\prime_{ab}, k^{fg}$ and k^{mix} are factors related to pair cuts. ϵ_{single} represents the single particle efficiency for 2π azimuth and ONE unit pseudo-rapidity. $R_{\Delta\eta}$ is the fraction of jet pairs within $\Delta\eta$ acceptance, and $\Omega_{\Delta\eta} = 1.4$ is the total pair phase space. If we ignore the pair cuts, Eq.17 can be simplified to,

$$\epsilon_{asso} = A_{\Delta\eta}\epsilon_{single} \approx \frac{I_\eta\epsilon_{single}}{1.4R_{\Delta\eta}} \tag{20}$$

If we further assume that the pair acceptance is triangle in $\Delta\eta$, Eq.20 can then be simplified to

$$\epsilon_{asso} = A_{\Delta\eta}\epsilon_{single} \approx \frac{\epsilon_{single}}{0.7R_{\Delta\eta}} \tag{21}$$

$R_{\Delta\eta}$ can be written down analytically, Since the near side correlation has a well behaved peak around $\Delta\eta = 0$, we correct the near side yield to the full jet yield assuming the shape of the jet shape is gauss and the widths are equal in $\Delta\phi$ and $\Delta\eta$. In the away side, the jet signal is much broader than the PHENIX acceptance, so we instead correct the yield to $|\Delta\eta| < 0.7$ assuming that the jet correlation strength is constant in this range. The formula for $R_{\Delta\eta}$ is,

$$R_{\Delta\eta} = \begin{cases} \dfrac{1}{2\int_0^{0.5\Omega_{\Delta\eta}} d\Delta\eta\frac{1}{\sqrt{2\pi}\sigma}e^{-\frac{\Delta\eta^2}{2\sigma^2}}\left[\frac{\Omega_{\Delta\eta}-2\Delta\eta}{\Omega_{\Delta\eta}}\right]} & \text{for near side} \\[4mm] \dfrac{\Omega_{\Delta\eta}}{2\int_0^{0.5\Omega_{\Delta\eta}} d\Delta\eta\left[\frac{\Omega_{\Delta\eta}-2\Delta\eta}{\Omega_{\Delta\eta}}\right]} = 2 & \text{for away side} \end{cases}, \tag{22}$$

In $\pi^{\pm} - h$ analysis, we construct the CFs for different for trigger and associated p_T ranges. We then obtain the raw conditional yield using either a fitting or a subtraction procedure. Finally, the raw conditional yield is corrected according to Eq.21 to obtain the true yield: we can evaluate $A_{\Delta\eta}$ directly according to Eq.18 via event mixing, or we can evaluate analytically by calculating $R_{\Delta\eta}$.

4.2 Raw yield

4.2.1 Traditional method

As discussed in section, the raw conditional yield is extracted by a simultaneous fit of the foreground and mixing distributions. We shall discuss it again for completeness. Fig.20 shows various histograms obtained for $5 < p_{T,trig} < 10$ GeV/c and $1.5 < p_{T,asso} < 2$ GeV/c. The left panel shows the foreground $\Delta\phi$ distribution(black) and mix distribution(blue), together with the simultaneous loglikelihood fit according to Eq.7. The middle panel shows the CF which is ratio of the black to blue, together with the double gauss function, the constant level, p_0, reflects the background level in the foreground relative to that given by mixed distribution. The right panel gives,

$$\frac{1}{N_{trig}} \frac{dN^{fg}/d\Delta\phi}{\frac{2\pi dN^{mix}/d\Delta\phi}{\int d\Delta\phi dN^{mix}/d\Delta\phi}} \tag{23}$$

Which is obtained by dividing the foreground distribution by the normalized mix distribution(to 2π) and the number of triggers, N_{trig}. So the CY is what left after subtracting the flat background. In principle, we could do an absolute background subtraction technique as done in analysis note [7], but since there is no elliptic flow contribution. The fitting procedure is better.
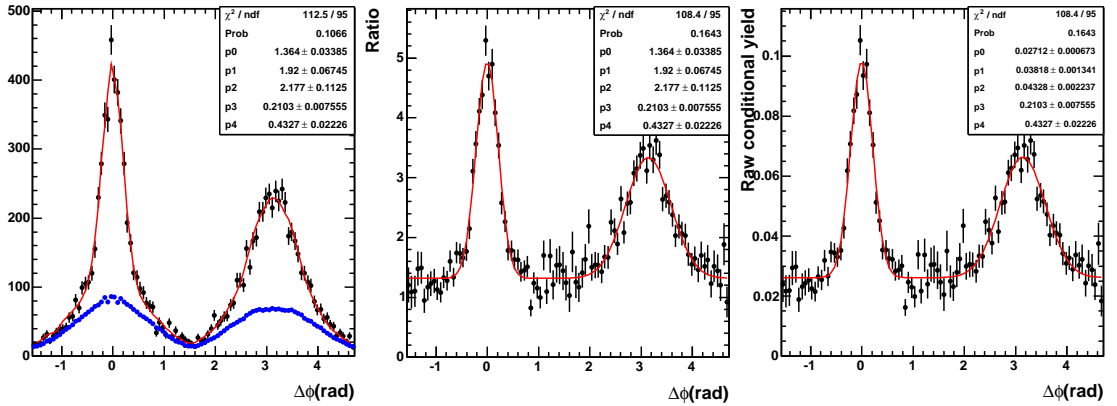
Figure 20: The illustration of the procedure to obtain the raw conditional yield, with $5 < p_{T,trig} < 10$ GeV/c and $1.5 < p_{T,asso} < 2$ GeV/c. Left panel show the foreground (upper histogram) and mixed background(lower histogram) distributions. The red curve is simultaneous loglikelihood fit to both foreground and mix background. The middle panel shows the CF and the right panel shows the raw conditional yield. The functions are obtained by rescaling the double gauss term determined from the simultaneous loglikelihood fit in left panel.

The above procedure can only give one data point for each combination of trigger and associated particle p_T ranges. To plot the CY as function of $p_{T,asso}$, one have to correct for finite bin width. In addition, if one want to obtain the x_E or p_{out} distribution, one have

to calculate them separately for each combination. The larger the p_T ranges, the larger the error on mean p_T, x_E or p_{out}.

4.2.2 Statistical method

To overcome the limitation of the traditional methods, we have developed a statistical method to extract the CY. This methods gives the distribution as function of $p_{T,asso}$, x_E or p_{out} directly, so the uncertainties due to the bin shift correction are eliminated.

As we have argued in analysis note 313, the normalized mixing distribution reflects the pair efficiency function $\epsilon(\Delta\phi)$. The dividing procedure in middle panel of Fig.20 is equivalent to dividing each foreground pair by the corresponding efficiency. So equivalently, if we know the $\epsilon(\Delta\phi)$, we can calculate the CY as function of any variable X in the following way.

For foreground:

> *foreach{foreground pair}{*
> *calculate $\Delta\phi$;*
> *read $\epsilon(\Delta\phi)$ from mix distribution;*
> *fill $\Delta\phi$ histogram: $h_{fg} \rightarrow Fill(X, 1/\epsilon(\Delta\phi))$*
> *}*

Similarly for mixed pairs:

> *foreach{mixed pair}{*
> *calculate $\Delta\phi$;*
> *read $\epsilon(\Delta\phi)$ from mix distribution;*
> *fill $\Delta\phi$ histogram: $h_{mix} \rightarrow Fill(X, 1/\epsilon(\Delta\phi))$*
> *}*

The signal `DISTRIBUTION`(instead of a number) is obtained as,

$$h_{signal} = h_{fg} - \lambda h_{mix} \tag{24}$$

Where λ is the pedestal level in the foreground which is determined from the fit.

Apparently, if X represents $\Delta\phi$, h_{mix} will be a constant histogram, and h_{fg} would be identical to the histogram in the right panel of Fig.20. In our analysis, the three most important variables are $p_{T,asso}$,x_E and p_{out}.

We shall use x_E as an example, Fig.21 shows the x_E distribution limited to the near side $|\Delta\phi| < \pi/2$. The p_T ranges are $5 < p_{T,trig} < 10$ GeV/c and $1.5 < p_{T,asso} < 2$ GeV/c. The foreground and scaled background x_E distributions are shown in red and blue. And the difference, which gives the signal, is shown in magenta.

We repeat this exercise for different associated p_T bins, while keeping the trigger p_T range fixed. And repeat the subtraction procedure for each bin. The results are shown in Fig.22. Similar procedure can also be applied for the away side x_E distribution ($\Delta\phi > \pi/2$) and is shown in Fig.23, the x_E value for away side is negative. As these two figures clearly demonstrated, the x_E distributions have significant overlap between different associated p_T bins. Due to this overlap, the mean x_E value from the final x_E spectra is very different from the mean x_E value for individual p_T bin, unless one have very narrow trigger p_T bin. Being able to determine the x_E value more precisely is the primary advantage of our statistical method over the traditional methods.
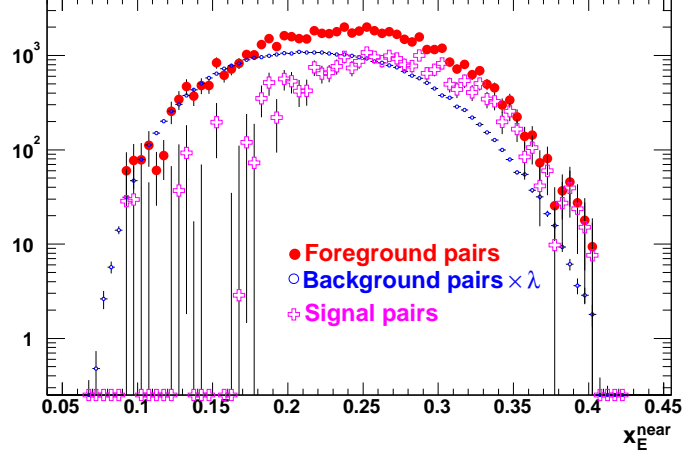
Figure 21: The x_E distribution for foreground (red), mix scaled by the pedestal λ(blue) and the signal(magenta) for p_T ranges of $5 < p_{T,trig} < 10$ GeV/c and $1.5 < p_{T,asso} < 2$ GeV/c.
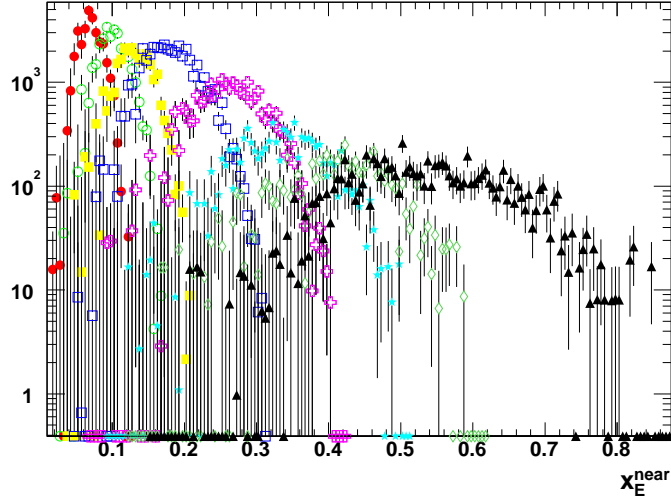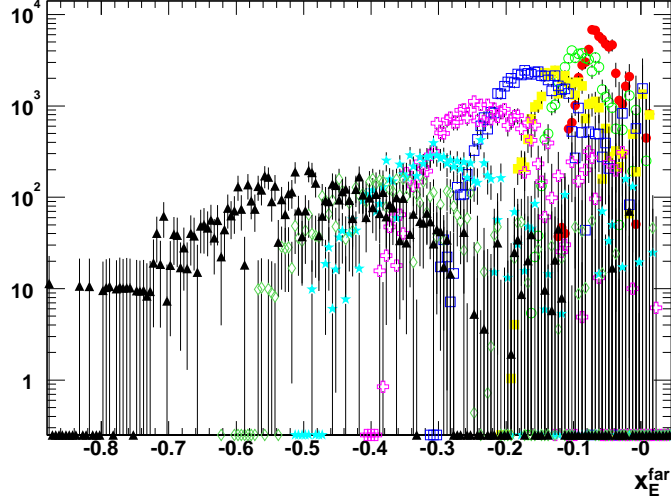

Figure 22: The background subtracted x_E distribution at the near side ($|\Delta\phi| < \pi/2$) for 7 associated p_T ranges, the trigger p_T range is fixed, $5 < p_{T,trig} < 10$ GeV/c.
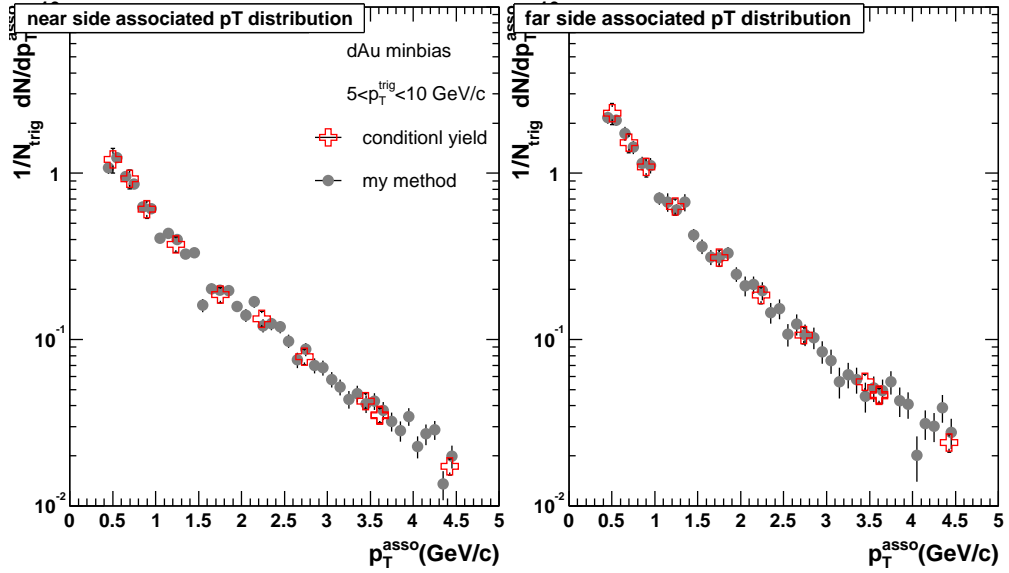
Fig.24 compares the near side CY(left panel) and far side CY(right panel) extracted from the two different methods. The statistical methods gives more data points but the overall yield are consistent with each other.

Figure 23: The background subtracted x_E distribution at the far side ($\Delta\phi > \pi/2$) for 7 associated p_T ranges, the trigger p_T range is fixed, $5 < p_{T,trig} < 10$ GeV/c.

Figure 24: Comparison of the CY extracted using the traditional fitting method(open crosses) and statistical method(filled circles). The left panel shows the near side CY and the right panel shows the away side CY. The trigger p_T is from 5-10 GeV/c

4.3 Efficiency determination

To get the final distribution, we have to determine the efficiency factor ϵ_{single} as illustrated in Eq.21. Instead of finding the efficiency from scratch which involves detailed simulation study, we take advantage of the fact that the inclusive charged hadron spectra has been

23

finalized in PHENIX for both $p - p$[5] and $d - Au$[4, 8, 9]. We calculate the efficiency factor backwards,

$$\epsilon_{single} = \frac{(dN/dp_T)_{raw}}{(dN/dp_T d\eta)_{corrected} \times \epsilon_{trigbias}} \tag{25}$$

The advantage is obvious, the only thing we need to do is to determine the raw spectra and we have to correct the measured spectra by the trigger bias. Everything else, including the systematical errors, are given automatically from the corrected spectra.

Fig.25 shows the single particle efficiency calculated in this way for several different cuts for $d - Au$ minimum bias collisions. In Fig.26, we compare the efficiency for centrality selected $d - Au$ collisions and $p - p$ collisions. The difference between all three curves (central $d - Au$, peripheral $d - Au$ and $p - p$) are about 10% of the efficiency.
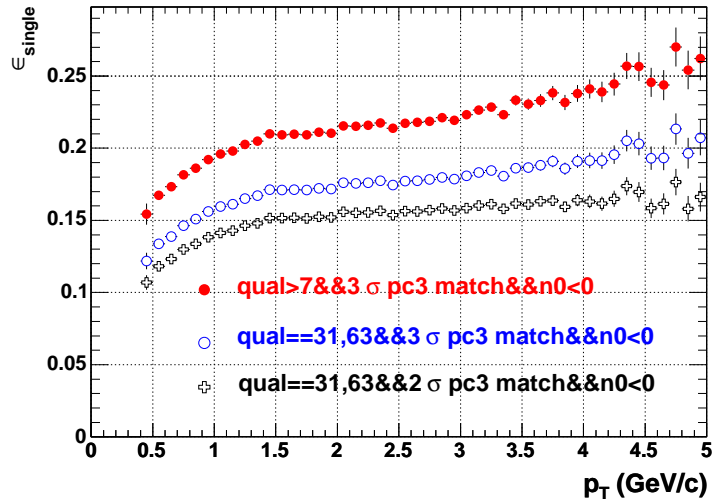
Figure 25: The charged hadron efficiency as function of p_T for three different cuts.

The systematic error can be obtained from the corresponding analysis note. Table.1 summarize the systematic errors from $p - p$ and $d - Au$.

Several thing we want to point here, 1)In analysis note 276, the dead area(1%) and time variation(4.4%) for $p - p$ is the same as the active area correction for $d - Au$, we combine them and also call it active area. 2) Analysis note 276 did not quote the uncertainty on momentum scale, but it should be similar to $d - Au$. 3) analysis note 202 for $d - Au$ didn't correct for feeddown while $p - p$ have. Because of all these differences, it is hard to factorize out the uncertainties that are common between $d - Au$ and $p - p$. 4) we haven't include the uncertain on bbcbias because it is centrality and collisions system dependent. For simplicity, we simply treat the errors of the two as independent. 5) As we pointed before, the systematic error for CY efficiency could be different from the efficiency for single inclusive particle due to the difference in the spectra shape. Here, everything was quoted for single inclusive, but in the final systematic error table, we converted the numbers to that for associated hadrons.
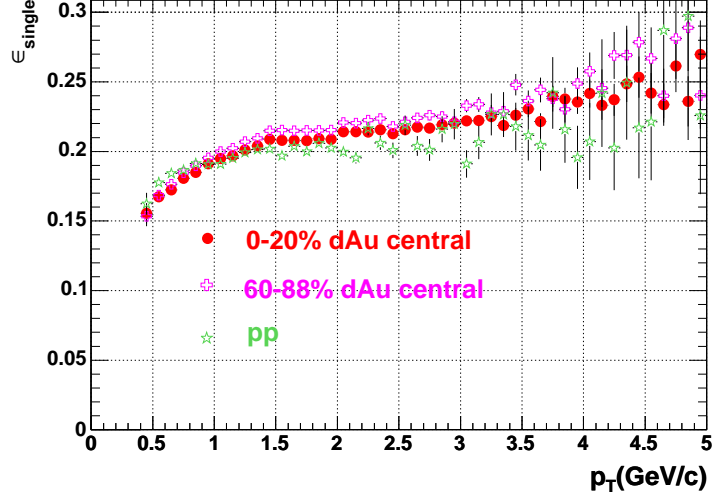
Figure 26: The charged hadron efficiency as function of p_T for 0-20% central $d - Au$ 60-88% peripheral $d - Au$ and $p - p$ collisions.

$d - Au$				
Error source	p_T indepen.	$< 4 GeV/c$	4 GeV/c	5 GeV/c
PC3 match		4%		
Active area		5%		
Monte Carlo		6.7%	6.2%	6.2%
p smearing	$1.1\% \pm 0.15\%(dp/p)$	-	$\ll 1\%$	$< 1\%$
p scale	1.039 ± 0.007	$< 5.5\%$	5.5%	5.8%
Background subtraction		$< 1\%$	1%	3%
total		10.8%		
$p - p$				
Error source	p_T indepen.	$< 4 GeV/c$	4 GeV/c	5 GeV/c
Match		4%		
Active area (time variation)		4.4%		
feeddown correction		7%		
p smearing	$1.1\% \pm 0.15\%(dp/p)$	-	$\ll 1\%$	$< 1\%$
Background subtraction		$< 1\%$	1%	3%
total		9.2%		

Table 1: The systematic errors for single inclusive efficiency correction.

4.4 Systematic error due to the fitting procedure

In the process of extracting the CY, we have assumed that the shape of the correlation function can be described by a constant plus double gauss. In low p_T region, the near side

and far side peak might become broad enough that they start to overlap with each other. When this happens the constant become correlated with the gauss shapes. We estimate the systematic error by varying the fitted constant by 1 σ and calculate the change in the resulting yield. Fig.27 shows an example of the correlation function and corresponding fitted parameter at small associated p_T. The amount of change in extracted yield change by about 15% when we vary the constant level by one σ. We evaluate this systematic error as function of $p_{T,asso}$, it is 15% at $p_T < 1$ GeV/c, and become negligible at $p_T > 2$ GeV/c. We plot this error at the near side as function of x_E (left) and p_T (right) in Fig.28 for $d - Au$ minbias (solid circles) and $p - p$ (open circles).
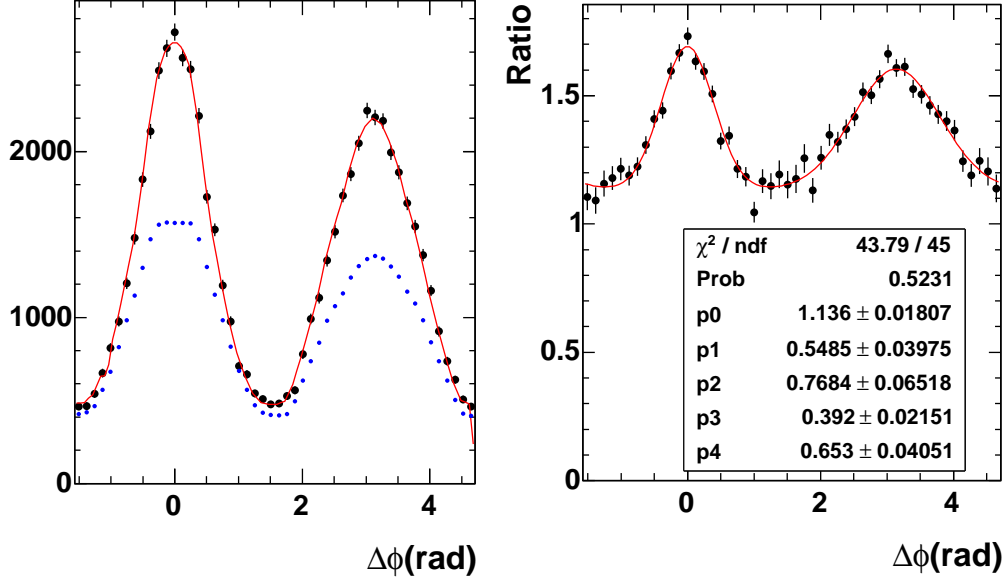
Figure 27: left figure: foreground and mixed distribution together with the simultaneous fit. right figure: the ratio of the two. Plotted for $5 < p_{T,trig} < 10$ GeV/c and $0.4 < p_{T,asso} < 1$ GeV/c.

The uncertainty of the constant background in correlation function is more important at the tail of the gauss peaks. Thus this systematic uncertainty is more important for the p_{out} distribution than anything else. A small change in the background level would leads to a large change of the tail of p_{out} distribution. This is shown in Fig.29 for near side (left) and far side (right). The error increase as function of p_{out}. The error itself also fluctuate a lot, caused by the fluctuation in statistics of the original p_{out} spectra. The error for $p - p$ is smaller than that for $d - Au$, presumably is due to the fact that the combinatoric background level in $d - Au$ is much larger than that in $p - p$.
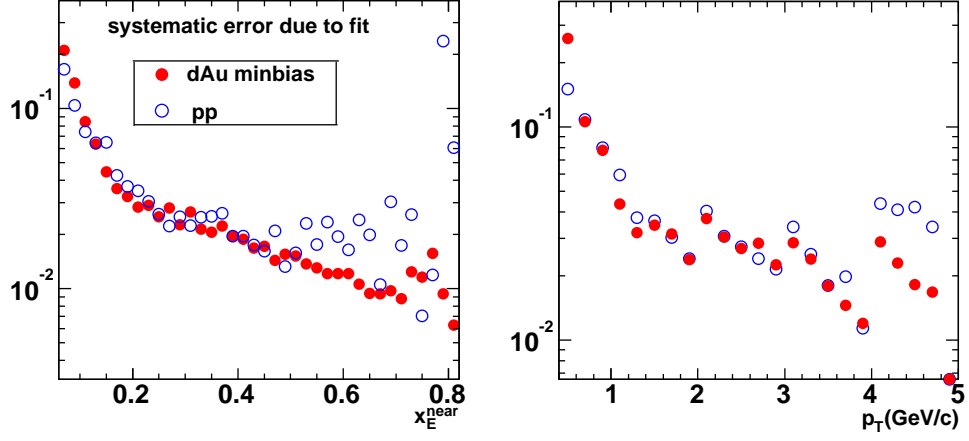
Figure 28: The systematic error due to the fitting procedure as function of x_E (left panel) and p_T (right panel) at the near side.
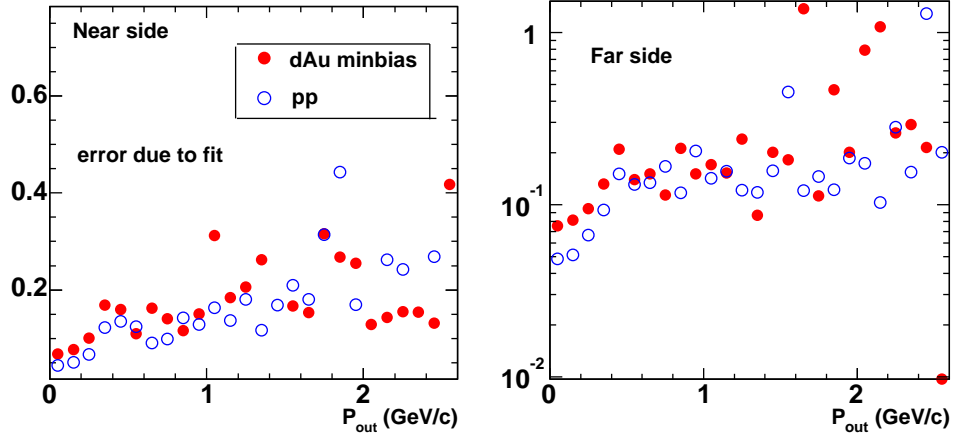
Figure 29: The systematic error due to the fitting procedure as function of p_{out} for near side (near side) and far side (right panel). The result for dAu is shown as solid circles, that for pp is shown as open circles.

4.5 Verifying the CY formulism

4.5.1 PHENIX acceptance

Due to the limited PHENIX acceptance, it is very important to crosscheck the correctness of the CY formula. The typical single particle acceptance/efficinecy for different vertex ranges ($|z| < 5cm$, $z > 20cm$ and $z < -20cm$) is shown in Fig.30. All tracks were selected requiring $quality > 7$ and $3\,\sigma$ matching at PC3. The hole in the middle is caused by the gap between north and south in PC3, the dropping at the edge of η is caused by the worsening of the tracking efficiency of the DC.
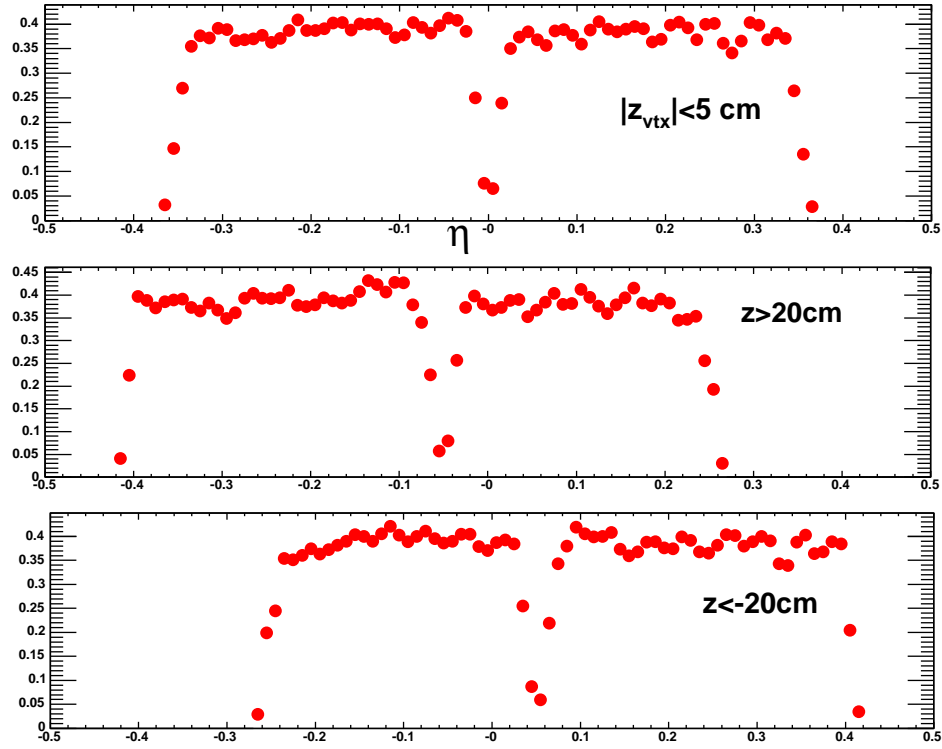
Figure 30: single particle acceptance+ efficiency as function of η from PISA simulation for three different vertex ranges: $|zvertex| < 5cm$ in top panel, $20 < zvertex < 30cm$ in middle panel and $-30 < zvertex < -20cm$ in bottom panel.

Since the locations for the hole and the edges in pseudo-rapidity depends on the vertex, the overall single particle acceptance/efficiency distribution in η averaged over all vertex locations are quite different from each individual plot, as shown in Fig.31. The hole is become wider but less deep, the edges are also smeared out.

Fig.32 shows the comparison of the pair distributions from event mixing for 10cm vertex bins(fill circles and open boxes) and for no vertex matching requirement(open circles), compared with triangle shape expected from ideal acceptance(solid line). All four histograms have the same integral. There are several features in the comparison, first, there is a flat shoulder structure around $|\Delta\eta| = 0.3$ when vertex matching is required. This shoulder was also seen in the real data(Fig.19) and is caused by the hole in the middle of η acceptance. The shoulder in simulation is narrower than those in real data, which is due to the fact that hole in real detector is wider. Since event mixing requires the matching vertexes, the pair distribution should be very close to what is shown by close circles. However, one does notice that all three mixing vertex ranges gives very similar pair acceptance almost independent of the mixing vertex ranges, which means the pair distribution is not very sensitive to the shape of the single particle distribution. The main difference is in the tail and the peaks.

Before continue with the testing of the CY formulism, Fig.33 shows the two dimensional single particle acceptance in PHENIX. The average efficiency in 1 unit of pseudo-rapidity

28
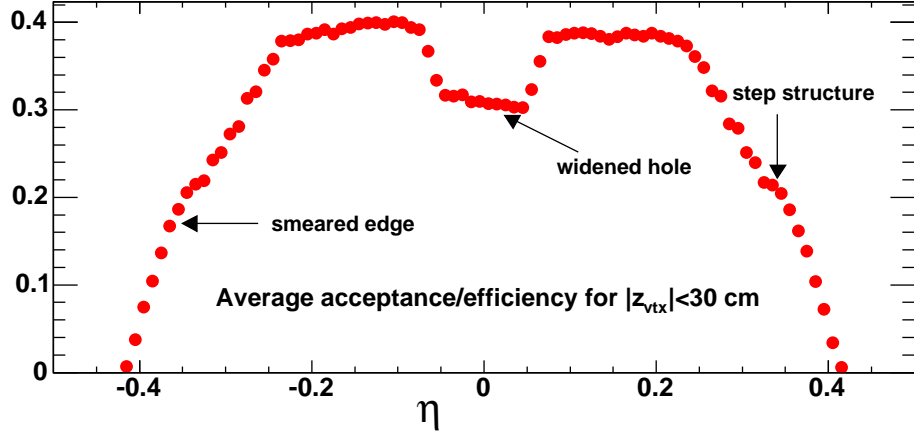
Figure 31: single particle acceptance+ efficiency as function of η from PISA simulation for vertex from -30 to 30 cm.
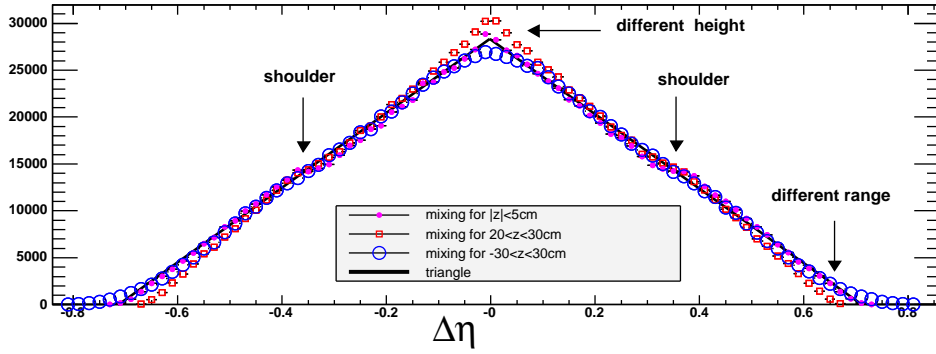
Figure 32: pair distribution from event mixing with different vertex ranges.

and 2π in azimuth is found to be

$$\epsilon_{single} = 0.256 \tag{26}$$

In the following, this histogram is used as the PHENIX acceptance filter in following study of the CY.

4.5.2 Verifying with simple simulation

In our first study, we generate 1 million jet events uniformly in $|\eta| < 1$ and 2π in azimuth. Each event have two particles, 1 leading particle of 20 GeV/c, and an associated particle from 0.4-5 GeV/c. The associated particle is smeared around the jet direction according to a j_T value of 400 MeV/c:

$$\phi_{asso} = \phi_{jet} + ran- > Gaus(0, 0.4)/p_{asso}; \tag{27}$$
$$\phi_{eta} = \eta_{jet} + ran- > Gaus(0, 0.4)/p_{asso};$$

29
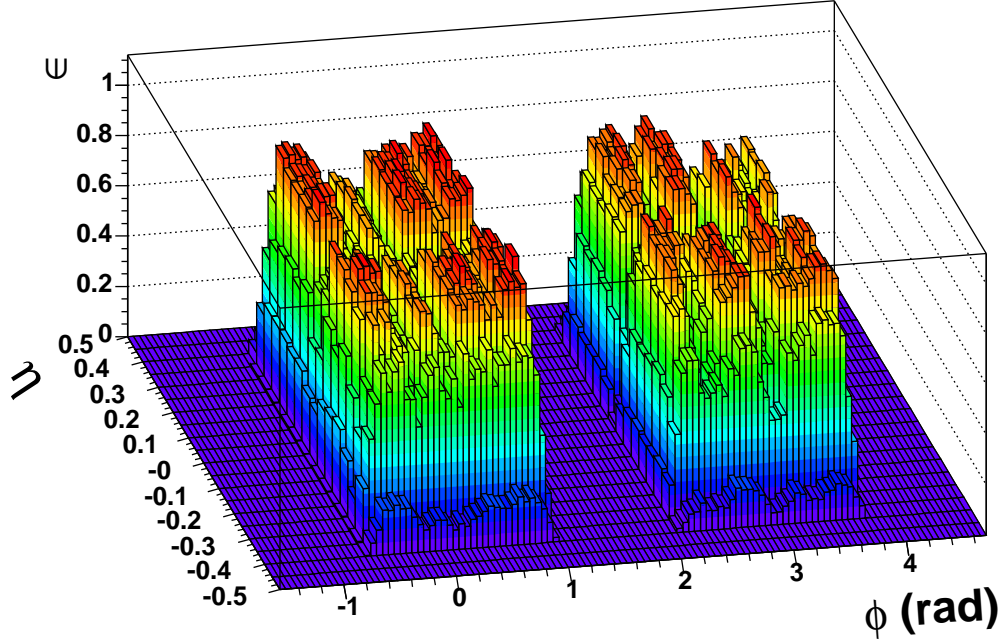
Figure 33: PHENIX single particle acceptance.

We test each pair of trigger and associated particle with the PHENIX acceptance filter shown in Fig.33, and only keeps those that passes the test. We then construct the foreground and mixed distribution via the standard procedure, then use the CY formula to extract the yield, we use $\epsilon_{single} = 0.256$ as the efficiency of the associated particles. Since each generated jet has only 1 associated particle, the expected CY is 1.

Fig.34 shows the correlation function and raw CY extracted for associated $p_T = 1$ GeV/c. There is only near side correlation by construction. Fig.35 shows a summery of the corrected yield as function of correlation width for several associated particle p_T selections. As one can see, our procedure give the jet width very accurately, it also recovers the CY within 5% of the true yield.

The conclusion from this study is that, knowing exactly the jet shape and how much conditional yield we put in, we can recover both width and CY within 5%.

4.5.3 Verifying with pythia simulation

Our next step is to test the acceptance filter with a more realistic Monte carlo program – Pythia 6.134 with CTEQ set 5L (LO) structure functions. We generate 1 million pythia events, each with a > 6 GeV/c charged pions and filter the events through the PHENIX acceptance filter. As an approximation, we ignore the p_T dependence of acceptance.

Similar to previous test, we extract the CY for $\pi\pm - h^\pm$ with and without PHENIX acceptance, requiring the trigger pion have a $7.5 < p_T < 10$ GeV/c. The comparison of the CY and width is shown in Fig.36. In the near side, the corrected yield(top left panel)

30
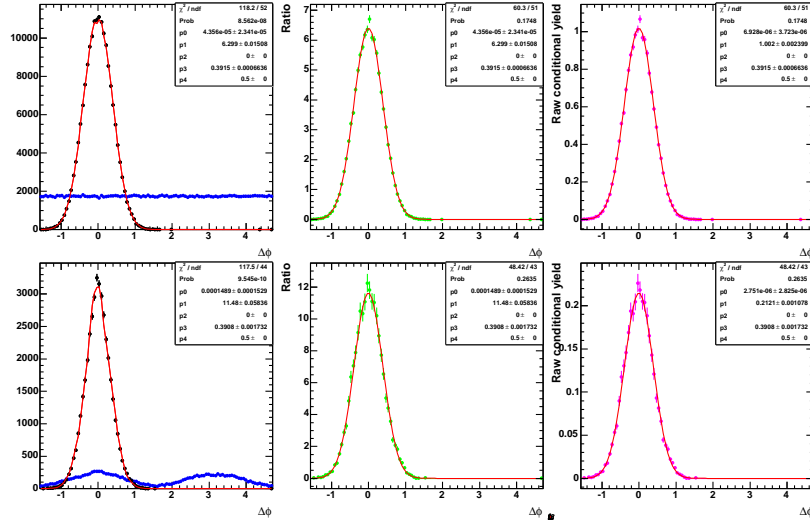
Figure 34: Top row is without acceptance filter, bottom row is with PHENIX acceptance filter. Left panel shows the foreground(black) and mix distribution(blue), middle panel shows the correlation function, the right panel shows the raw CY(the second parameter of the fit).
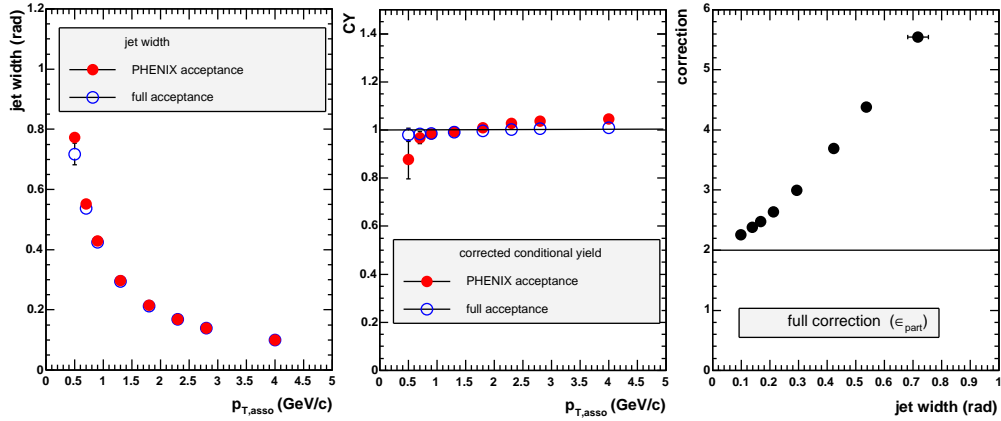
Figure 35: The jet width (left), CY(middle) as function of associated p_T. The filled circle stand for the values determined without acceptance filter, the open circles represents the values obtained with the PHENIX acceptance filter. The right panel shows the correction factor on CY as function of jet width.

and width(bottom left panel) are compared with those extracted without acceptance filter. In the away side, the yield with acceptance filter corrected back to $|\Delta\eta| < 0.7$ is compared with expected yield in the top right panel. The bottom right panel compares three different away side jet widths: width with no constrains on the pair acceptance, width requiring $|\Delta\eta| < 0.7$ and width with PHENIX acceptance filter. The data with acceptance filter are always indicated by the filled circles while the expected yield or width are indicated with either open circles or open crosses.

The difference between the data sets can be better seen by plotting the ratios, which are
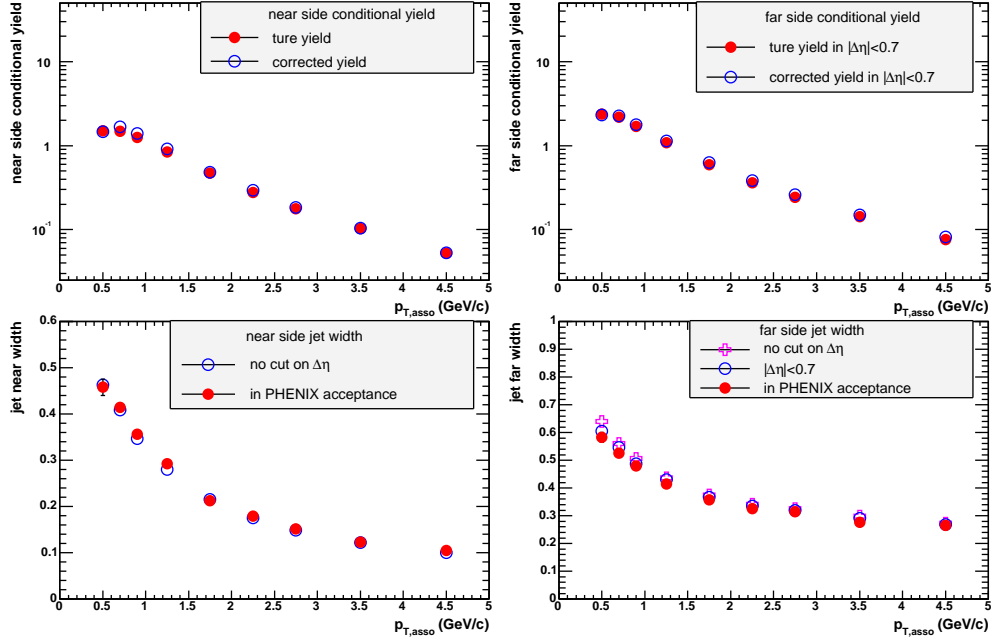
Figure 36: The comparison of near side yield (top left panel), near side width (bottom left panel), far side yield(top right panel) and far side width (bottom right panel). The open circles represents the quantities calculated with PHENIX acceptance filter.

shown in Fig.37. The yields agrees within 10% and the widths agrees within 5%. There are some systematic trends in the differences. In particular, the away side jet width seems to depend on the integration range in $\Delta\eta$. The larger the $\Delta\eta$ range, the bigger the away side jet width. This could be real physics rather than artifact of the our procedure. Also one can notice that there are some systematic trend in the comparison of the yield at low $p_{T,asso}$, this might indicate that the gauss assumption is not very good when the extrapolation is big.

The conclusion from this study is that given that the pythia describe correctly all the physics (including the jet shape, the shape of the underlying background), a gauss extrapolation and event mixing procedure can reproduce the CY within 10% and the width within 5% for both near and far side.

4.5.4 Verifying with full PISA simulation

In real data analysis, the PHENIX acceptance is more complicated than just a pure acceptance filter. Several things need to be taken into account: 1) pair cuts; 2) decay and feeddown; 3) background in the triggers. The only way to estimate these effects are through full Geant simulation of the PHENIX detectors.

Under the standard pair curs, the pair efficiency, $k(\Delta\phi, \Delta\eta)$, should be identical between foreground and mixed background. Thus if we extract the CY from two dimensional correlation function, pair cut correction cancels between foreground and mixed background. However, in one dimensional correlation function, there remains a finite correction that we need to take into account. According to analysis note 311, to first order, the pair correction
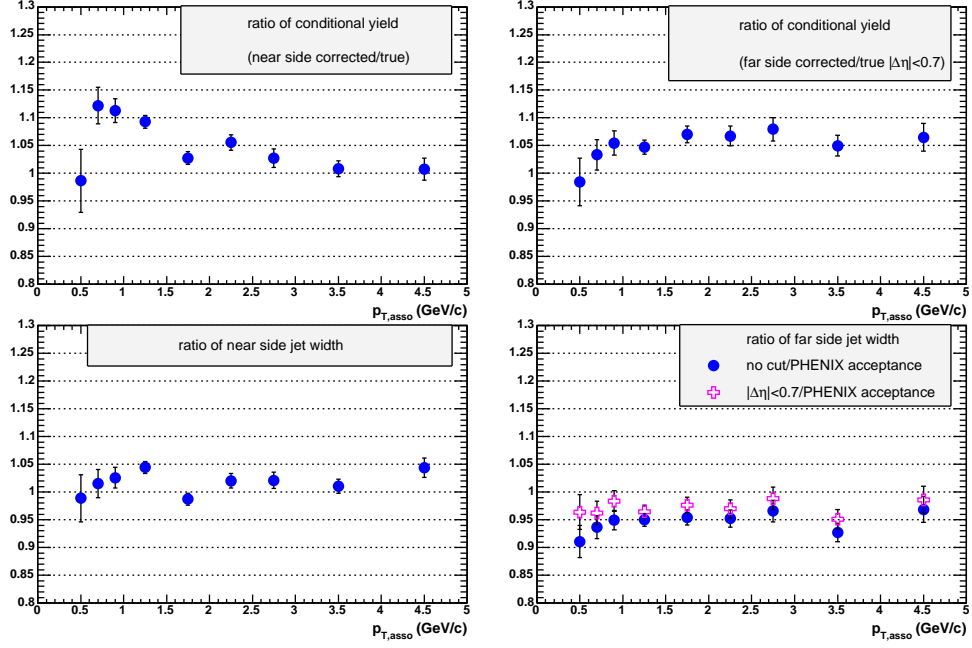
Figure 37: The ratio of the corrected yield or width to those without acceptance filter.

can be calculated as,

$$\epsilon_{pair} = \frac{\int g(\Delta\phi)d\Delta\phi}{\int k_{mix}(\Delta\phi)/k_{fg}(\Delta\phi)g(\Delta\phi)d\Delta\phi} \qquad (28)$$

where $g(\Delta\phi)$ is the jet shape in $\Delta\phi$, which we assume to be gauss, $k_{mix}(\Delta\phi)$ and $k_{fg}(\Delta\phi)$ are the weighted average of the pair cut in $\Delta\eta$ for mixing background and foreground, respectively:

$$\begin{aligned}
\frac{1}{k^{fg}(\Delta\phi)} &= \frac{\int d\Delta\eta \frac{1}{k(\Delta\phi,\Delta\eta)}\frac{dN^{fg}}{d\Delta\phi d\Delta\eta}}{\int d\Delta\eta \frac{dN^{fg}}{d\Delta\phi d\Delta\eta}} \\
\frac{1}{k^{mix}(\Delta\phi)} &= \frac{\int d\Delta\eta \frac{1}{k(\Delta\phi,\Delta\eta)}\frac{dN^{mix}}{d\Delta\phi d\Delta\eta}}{\int d\Delta\eta \frac{dN^{mix}}{d\Delta\phi d\Delta\eta}}
\end{aligned} \qquad (29)$$

ϵ_{pair} can be calculated straightforwardly from the mixing distribution, $\frac{dN^{mix}}{d\Delta\phi d\Delta\eta}$, which can be measured directly, and foreground distribution, which can be approximated with a double gauss function,

$$\frac{dN^{fg}}{d\Delta\phi d\Delta\eta} \propto e^{-\frac{\Delta\phi^2+\Delta\eta^2}{2\sigma^2}} \qquad (30)$$

One example of the pair correction for trigger $7.5 < p_T < 10 GeV/c$ and associated $4 < p_T < 5 GeV/c$ is shown in Fig.38. The similar plot for associated $2 < p_T < 2.5 GeV/c$ is shown in Fig.39. The shape difference between the two corrections can be easily understood if
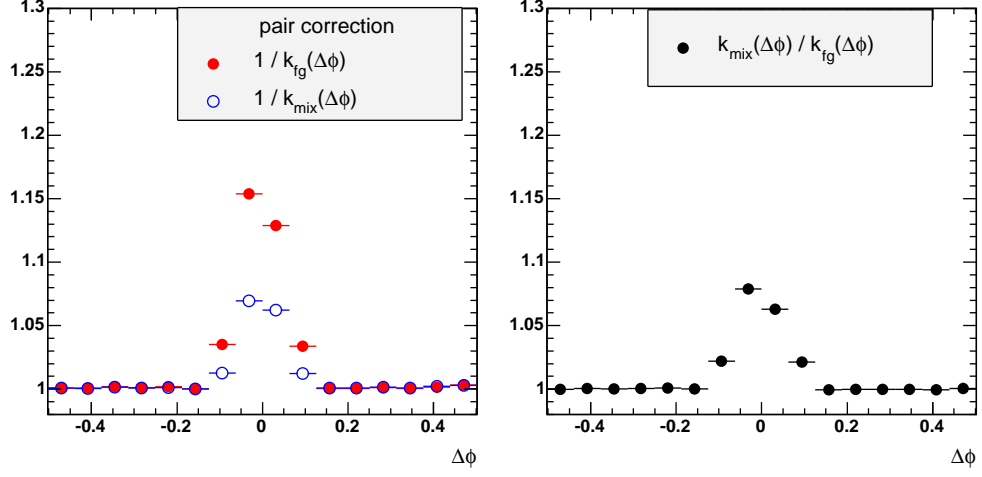
Figure 38: Left panel shows $\Delta\eta$ averaged pair cut correction for mixed background(open circles) and foreground(filled circles). Right panel shows the ratio of the two. The trigger p_T is $7.5 < p_T < 10 GeV/c$, and the associated particle p_T is $4 < p_T < 5 GeV/c$.
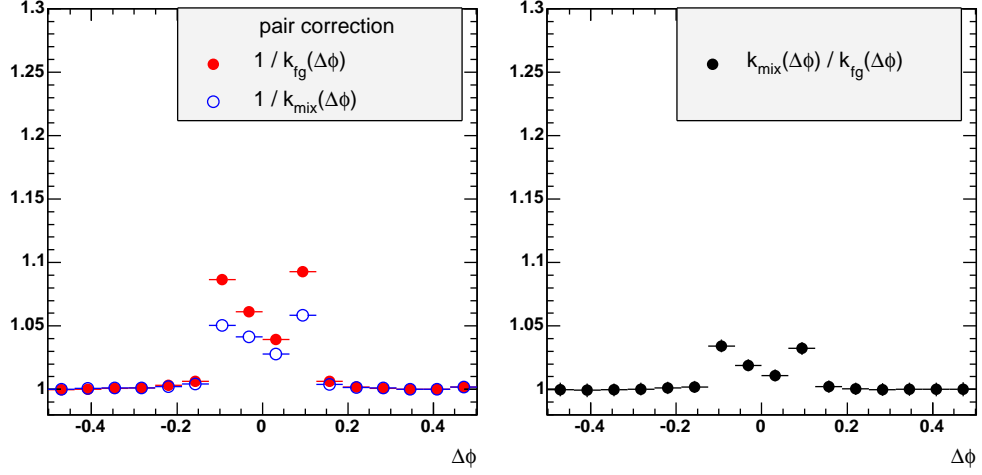
Figure 39: Left panel shows $\Delta\eta$ averaged pair cut correction for mixed background(open circles) and foreground(filled circles). Right panel shows the ratio of the two. The trigger p_T is $7.5 < p_T < 10 GeV/c$, and the associated particle p_T is $2 < p_T < 2.5 GeV/c$.

the bending of the tracks in azimuth direction is taken into account. The bending is roughly inversely proportional to the momentum. So at low p_T, one see two peaks corresponding to two different charges. At high p_T, the bending become negligible and the two peaks merge with each other.

From these figures, we can calculate the correction due to the pair cuts from Eq.28. The results is shown in Fig.40.

Fig.41 shows the CY and width derived from CNT from the PISA simulation and track reconstruction, compared with the true yield and width for $\pi^\pm - h^\pm$ correlation. THe correlation due to pair cuts have been applied. The agreement is excellent, except for the near

34
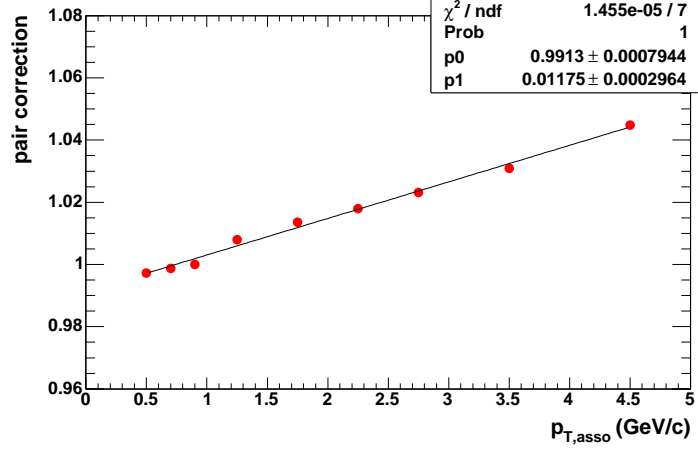
Figure 40: The overall pair cut correction ϵ_{pair} as function of associated particle p_T.
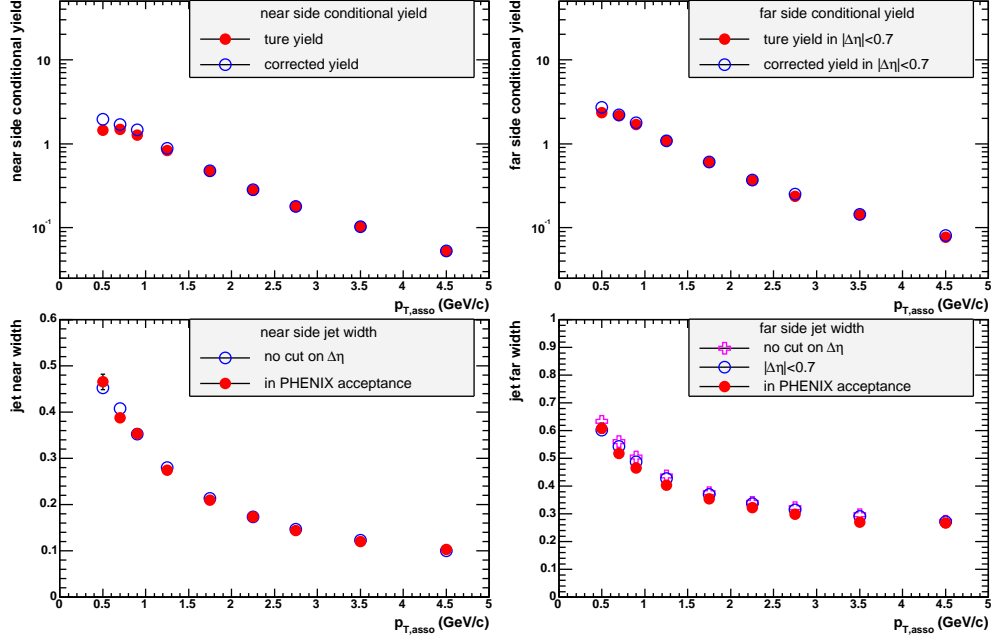
Figure 41: The comparison of near side yield (top left panel), near side width (bottom left panel), far side yield(top right panel) and far side width (bottom right panel). The open circles represents the quantities derived from the CNT created after the full PHENIX response chain.

side CY at low $p_{T,asso}$. Is this due to resonance contribution? don't know yet but will check later.

The conclusion from this study is that with realistic detector responses, our procedure can reproduce the width within 5% for both near and far side and can reproduce the near side CY at $p_T > 1$ GeV/c and far side CY within 7%. For CY at $p_T < 1$ GeV/c, a p_T
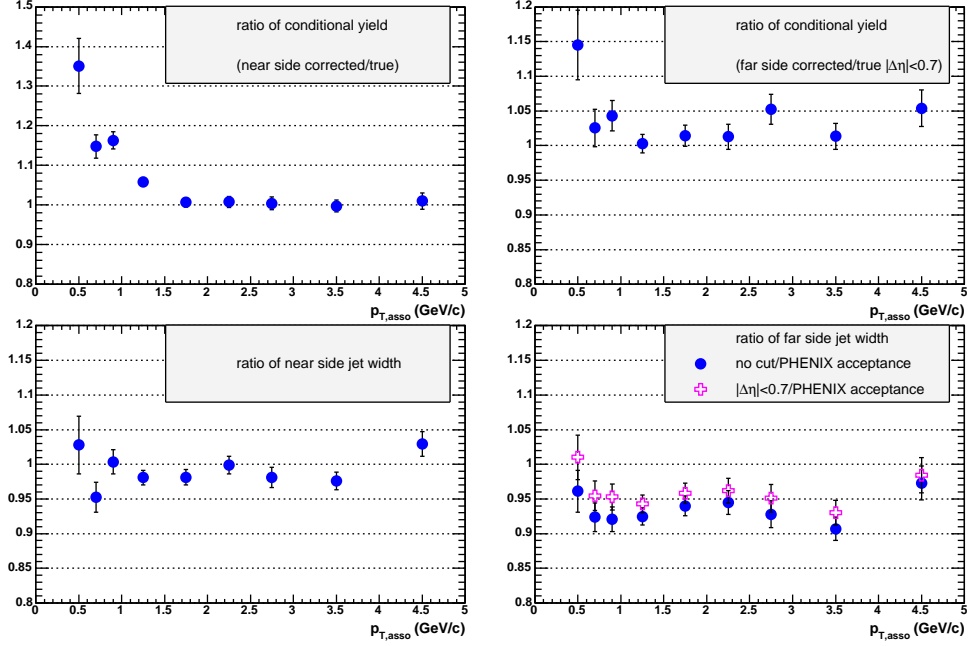
Figure 42: The ratio of the corrected yield or width to those without acceptance filter.

dependent correction is needed.

4.5.5   PHENIX acceptance in $\Delta\eta$

As discussed in Section.3.1 and section4.5.1, PHENIX pair acceptance in $\Delta\eta$ is not a perfect triangle. Instead it is an parallelogram plus a triangle. Comparing Fig.19 with Fig.32, we see that simulation underpredicts the deviation from the pure triangular shape. In this section, we study the amount of correction due to this deviation.

The amount of correction can be easily calculated based on Eq.28. Right panel of Fig.43 shows the correction as function of jet width when the displacement between triangle and parallelogram is 0.1 rad(left panel). Fig.44 shows the same thing except that the displacement is 0.15 radian. We see the deviation of the ϵ_{pair} is maximum around 0.15 radian jet width and reach 1 for infinitely narrow jet width and infinitely wide jet width. So our conclusion is that if one use ideal triangle as approximations of the pair acceptance in $\Delta\eta$, the maximum error would be 5%. In our analysis, we do not use triangular approximation, we always use the realistic pair shape in calculating the ϵ_{pair}.

4.6   Trigger bias

See Jan's analysis note and consult with Nathan.

4.7   Systematic errors

Table2 summarize the list of systematic errors on the CY. The error on single particle correction is obtained from Table. 1. It has two parts, the normalization error includes the

36
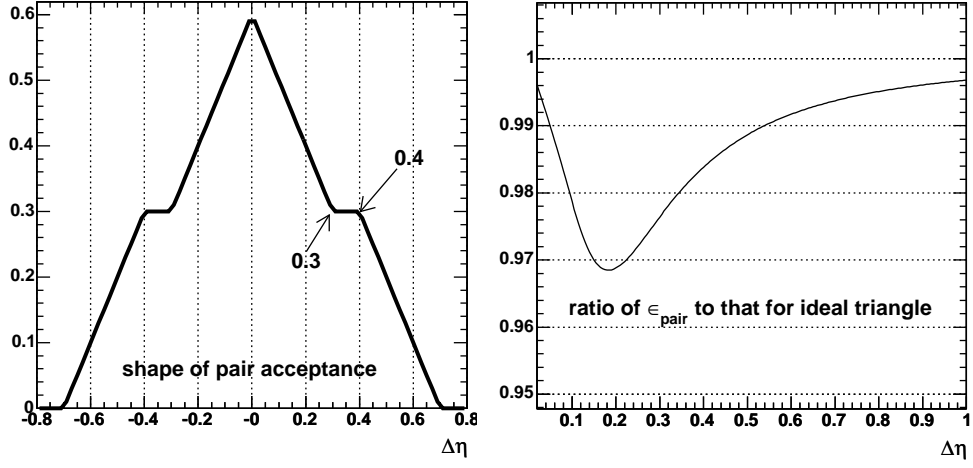
Figure 43: left panel shows the pair acceptance function when the upper edge of parallelogram is 0.8rad and the bottom edge of the triangle is 0.6 rad, right panel shows fractional difference of ϵ_{pair} from that for ideal triangular shape.
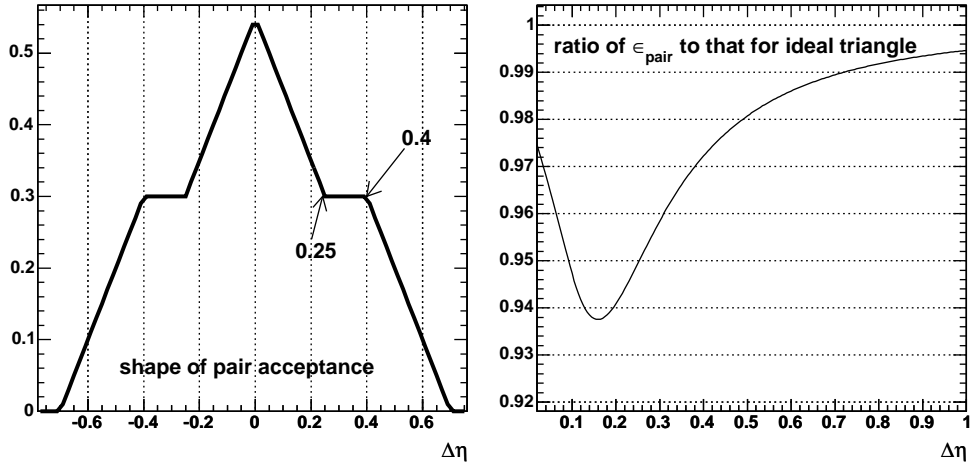
Figure 44: left panel shows the pair acceptance function when the upper edge of parallelogram is 0.8rad and the bottom edge of the triangle is 0.5 rad, right panel shows fractional difference of ϵ_{pair} from that for ideal triangular shape.

Error source	p_T indepen.	$< 1GeV/c$	2 GeV/c	4 GeV/c
single particle ϵ_{single}				
normalization	6.5%			
p smearing(reso+scale)	3%			
centrality dependent part				
centrality dep background	5%			
background				
trigger pion background	5%			
associated hadron background	2%			
error from formula				
pair cuts		1%	3%	4%
MC near side yield		20%	6%	6%
MC far side yield	6%			
error on the fit		15%	3%	1%

Table 2: Summary of the systematic errors on the CY.

error on PC3 matching and active area. The p smearing error include contribution from momentum resolution and momentum scale, which we have reevaluated based on the shape of the CY. The centrality dependent part of the systematic error is taken from analysis note 311 [1]. The error due to the trigger background is also obtained from analysis note 311, the error on the associated particle background was also reevaluated based on the shape of CY. The error on formula includes contribution from our study in Section4.5. It include the error on the pair cuts and error on the CY.

Figure.45 shows the total systematic error as function of x_E and $p_{T,asso}$ for the near side and far side. Similarly Figure.46 shows the total systematic error as function of p_{out} for the near side and far side.
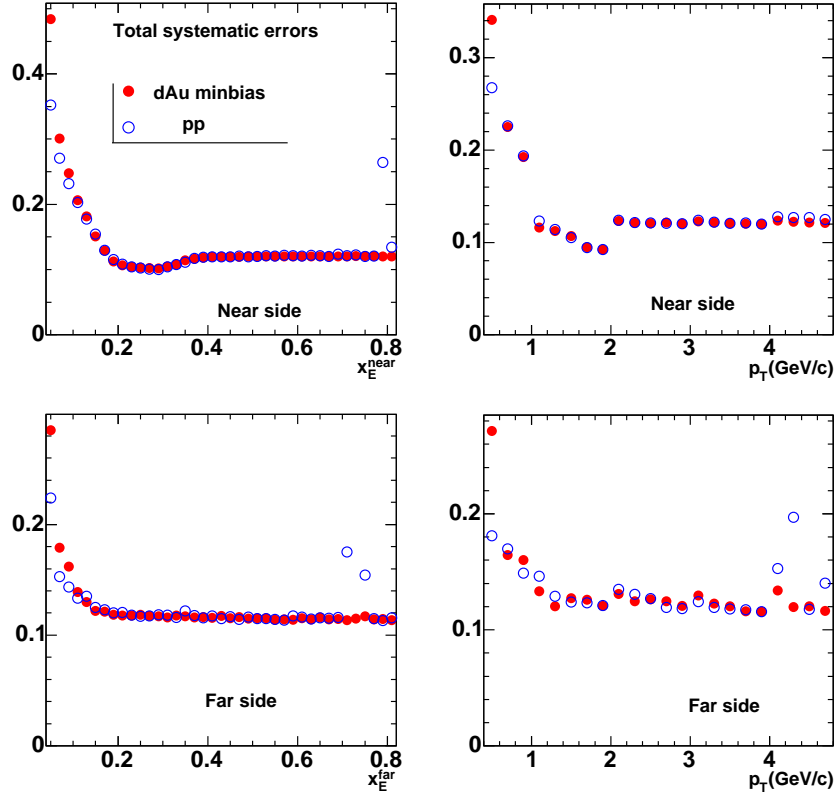
Figure 45: The total systematic error as function of $p_{T,asso}$ for x_E and $p_{T,asso}$ for both near side and far side (right panel). The result for dAu is shown as solid circles, that for pp is shown as open circles.
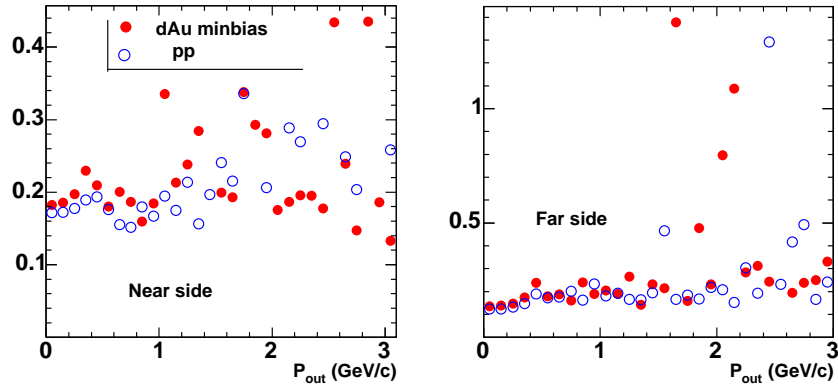
Figure 46: The total systematic error as function of p_{out} for both near side and far side (right panel). The result for dAu is shown as solid circles, that for pp is shown as open circles.

5 j_T, k_T analysis

5.1 P_{out} width

p_{out} value was calculated for each foreground or mix pair, and weighted by the correction for pair efficiency. We extract the p_{out} distributions for two $\Delta\phi$ ranges, $|\Delta\phi| < \pi/2$ for near side p_{out} distribution and $\Delta\phi > \pi/2$ for away side p_{out} distribution. Fig.47 illustrate the procedure for $|\Delta\phi| < \pi/2$. The trigger and associated particle p_T are $5 < p_{T,trig} < 10$ GeV/c and $1.5 < p_{T,asso} < 2$ GeV/c. The left panel shows the raw foreground(black) and mix(blue) distribution, the middle panel shows the pair efficiency corrected foreground(black) and mix(blue) distribution. The curve in both panels are simultaneous loglikelihood fit to foreground and mix according to

$$foreground(p_{out}) = (\lambda + \frac{yield}{\sqrt{2\pi}\sigma}e^{-\frac{p_{out}^2}{2\sigma^2}}) \times mix(p_{out}) \tag{31}$$

The right panel shows the extracted p_{out} distribution after subtracting the mix background from the middle panel. The curve is simply the gauss function obtained from the fit in the middle panel.
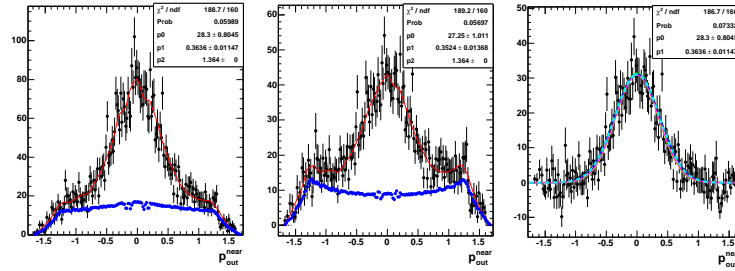
Figure 47: Extraction of p_{out} distribution for $|\Delta\phi| < \pi/2$, the trigger and associated particle p_T are $5 < p_{T,trig} < 10$ GeV/c and $1.5 < p_{T,asso} < 2$ GeV/c, respectively. The left panel shows the raw foreground(black) and mix(blue) distribution, the middle panel shows the pair efficiency corrected foreground(black) and mix(blue) distribution. The right panel shows the extracted p_{out} distribution after subtracting the mix background. The curve on the left and middle panels are simultaneous loglikelihood fit to foreground and mix.

Despite the significant difference between the shape of the background in this figure and that in the standard correlation function in $\Delta\phi$ (see example Fig.20), they should have the same amount of jet signal. Thus the CY extracted from Fig.47 should be the same as the same side yield from Fig.20. Indeed they are the same.

5.2   Comparison among formulas

In analysis note 312, we have argued that p_{out} is more directly related to the j_T and k_T. There we have derived two sets of formula:

SET1: The formulae for j_T, k_T using directly measured p_{out} RMS values are,

$$j_{T_y,1D} = \frac{\langle p_{out,N,1D} \rangle}{\sqrt{\langle 1 + x_h^2 - 2x_{j,trig}^2 \rangle}} \tag{32}$$

$$(k_{T_y} z_{trig})_{1D} = \sqrt{\frac{\langle p_{out,F,1D} \rangle^2 - \langle p_{out,N,1D} \rangle^2 \langle 1 - x_{k,trig}^2 \rangle}{2 \langle x_h^2 - x_{j,trig}^2 (1 + x_h^2 - 2x_{j,trig}^2) \rangle}} \tag{33}$$

SET2: The formulae for j_T, k_T using directly measured correlation width are,

$$j_{T_y,1D} = \sqrt{\frac{\langle p_{T,asso}^2 \rangle (sin\sigma_N^2 - \sigma_N^4)}{\langle 1 + x_h^2 - 2x_{j,trig}^2 \rangle}} \tag{34}$$

$$(k_{T_y} z_{trig})_{1D} = \sqrt{p_{T,asso}^2} \sqrt{\frac{(sin\sigma_F^2 - \sigma_F^4 + 16/9\sigma_F^6 - 8\sigma_F^{10}) - (sin\sigma_N^2 - \sigma_N^4)\langle 1 - x_{k,trig}^2 \rangle}{2 \langle x_h^2 - x_{j,trig}^2 (1 + x_h^2 - 2x_{j,trig}^2) \rangle}} \tag{35}$$

There is also the standard formula used by Jan in ppg029 [13],
SET3:

$$j_{T_y,1D} = \frac{\langle p_{T,asso} \rangle \langle p_{T,trig} \rangle \sigma_N}{\sqrt{\langle p_{T,asso} \rangle^2 + \langle p_{T,asso} \rangle^2}} = \frac{\langle p_T \rangle \sigma_N}{\sqrt{1 + x_h^2}} \tag{36}$$

$$(k_{T_y} z_{trig})_{1D} = \frac{\sqrt{\frac{\pi}{2}} \langle p_T \rangle}{\sqrt{2} x_h} \sqrt{sin^2 \sqrt{\frac{2}{\pi}} \sigma_F - (1 + x_h^2)sin^2 \frac{\sigma_N}{\sqrt{\pi}}} \tag{37}$$

To make detailed comparison of these three different sets of formula's, we use pythia simulation. The advantage is that we have much more statistics than real data to tell even a small difference.

Fig.48 shows the comparison of the three different sets of formulas. The j_T and zk_T 1D RMS value are plotted as function of associated particle p_T. The trigger p_T is always from 5 to 10 GeV/c. The overall agreements are pretty good. The differences in j_T are less than 5% at $p_{T,asso} > 1$ GeV/c, there is a sizable difference in zk_T value on the order of 5-15%. The rising trend in zk_T is due to the trigger bias effect which we will discuss in Section5.4.

5.3 Systematic errors on j_T and zk_T

In calculating the j_T and zk_T using formula Eq.32-37, we have to propagate the errors on every quantity used in the calculation to the final j_T, zk_T values. For example, for SET1 we need to propagate the error on p_{out}, x_h, and $p_{T,trig}$ (since $x_{j,trig} = j_T/p_{T,trig}$)

Fig.49- Fig.51 show the j_T and zk_T as function of $p_{T,asso}$ for $5 < p_{T,trig} < 10$ GeV/c from real data. Different sources of errors are shown in the bottom panels of each figure. The errors on p_{out} or the jet width were just from the fit. For errors on other quantities like x_h or $p_{T,trig}$, their RMS values are used as the errors.

In addition to the errors related to the formula that were included point by point through the error propagation procedure, there are other sources of systematic errors that need to
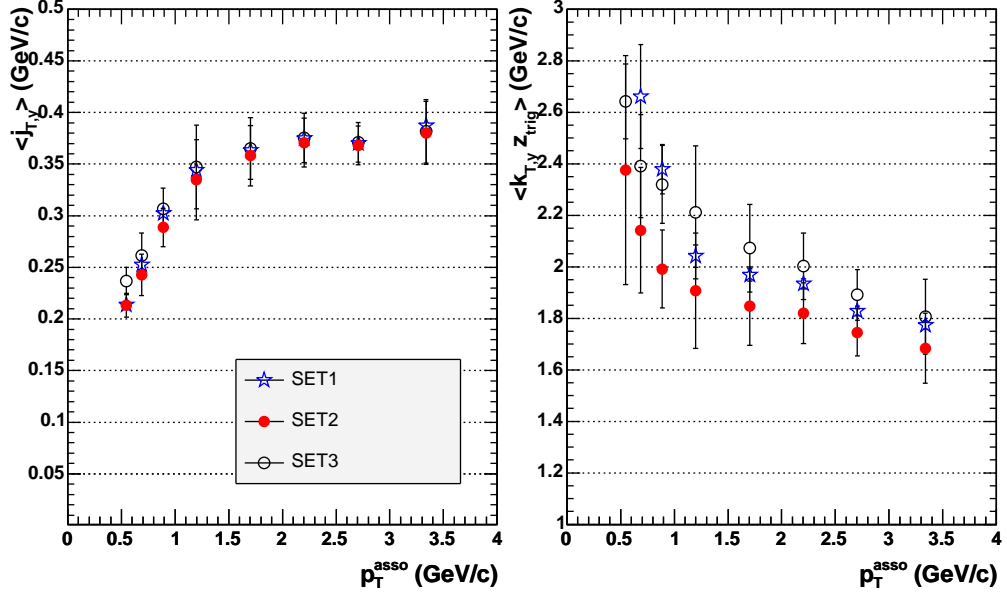
Figure 48: The extracted j_T, k_T from pythia simulation for three sets of formulas(see text)
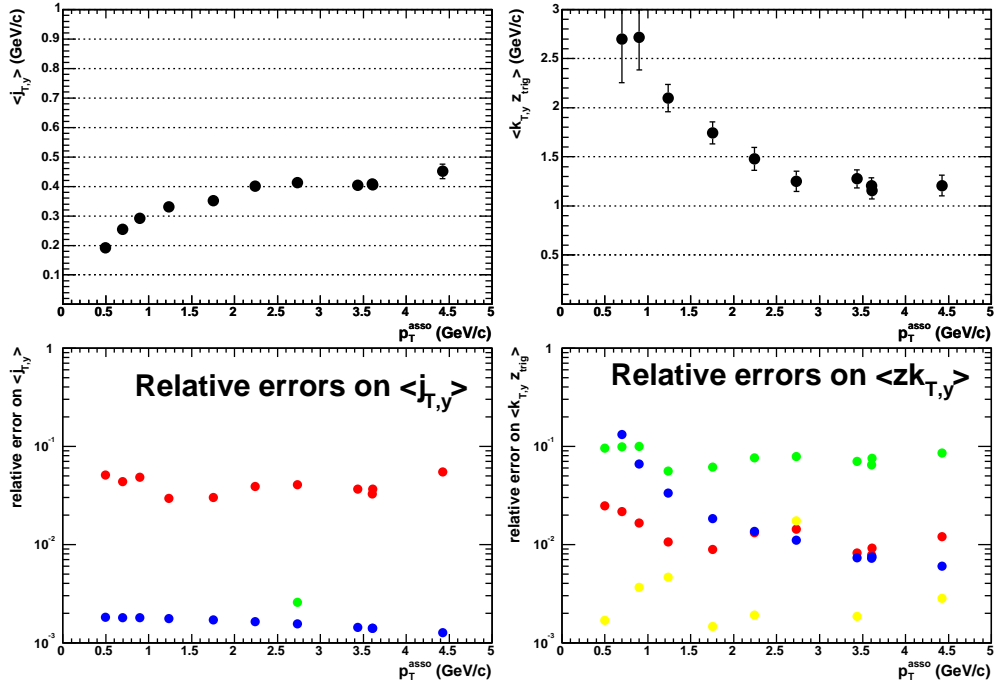
Figure 49: Example of the error propagation for using SET1 formula in deriving the j_T and zk_T. The extracted j_T(top left panel) and corresponding three different type of errors (bottom left panel) propagated from the formula. The extracted zk_T(top right panel) and corresponding four different types of errors (bottom right panel) propagated from the formula.
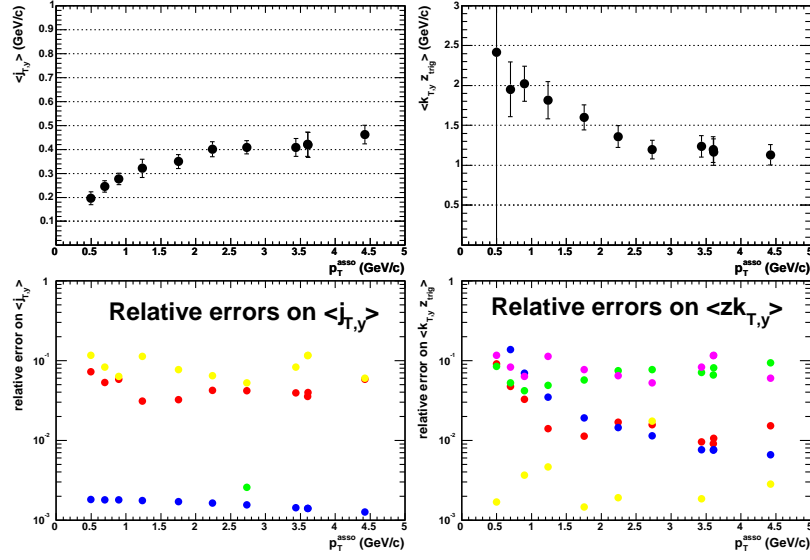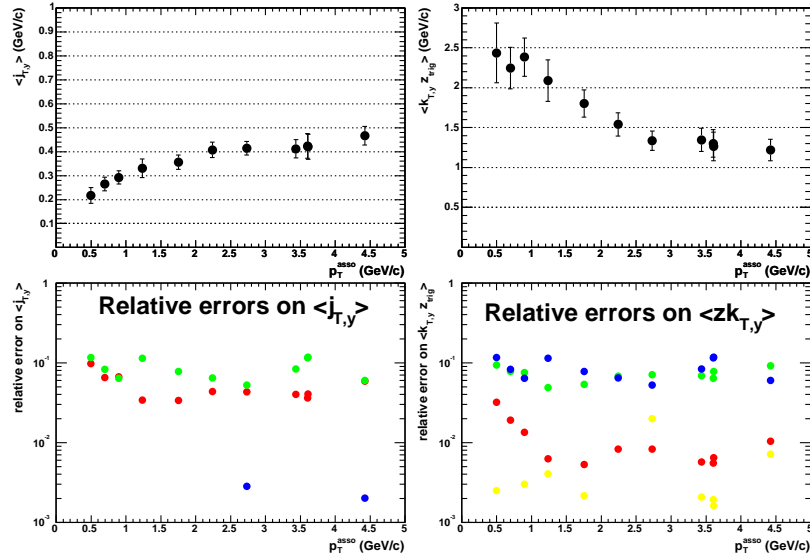
Figure 50: Example of the error propagation for using SET2 formula in deriving the j_T and zk_T. The extracted j_T(top left panel) and corresponding three different type of errors (bottom left panel) propagated from the formula. The extracted zk_T(top right panel) and corresponding four different types of errors (bottom right panel) propagated from the formula.

Figure 51: Example of the error propagation for using SET3 formula in deriving the j_T and zk_T. The extracted j_T(top left panel) and corresponding three different type of errors (bottom left panel) propagated from the formula. The extracted zk_T(top right panel) and corresponding four different types of errors (bottom right panel) propagated from the formula.

be taken into account. Most noticeability are the errors due to limited PHENIX acceptance, which we obtained by comparing the true and derived values on the jet width from pythia simulation. From Fig.42, we conclude that the errors are on the order of 5% in the away side width, which simply translate to 5% error on the zk_T value. [2]

5.4   Trigger bias

See Jan's analysis note[10] and nathan's [11]

6   Results

We present the results on CY as function of $\Delta\phi$, p_T, x_E or p_{out} and jet width, j_T, k_T. In each case, we compare the data between minimum bias $d - Au$, centrality selected $d - Au$ and $p - p$ collisions.

6.1   Correlation function(CY as function of $\Delta\phi$)

Fig.52-Fig.56 shows the absolutely corrected $\Delta\phi$ distribution ($\frac{1}{N_{trig}}\frac{dN}{d\Delta\phi}$) with trigger pions $5 < p_T < 10$ GeV/c, for minimum bias, 0-20%, 20-40%, 40-88% $d - Au$ collisions and $p - p$ collisions, respectively. In each figure, the $\Delta\phi$ distribution were plotted for 9 different associated charged hadron p_T ranges: 0.4-0.6 GeV/c, 0.6-0.8 GeV/c, 0.8-1.0 GeV/c, 1.0-1.5 GeV/c, 1.5-2.0 GeV/c, 2.0-2.5 GeV/c, 2.5-3.0 GeV/c, 3.0-4.5 GeV/c and 2.0-4.0 GeV/c. The near side ($|\Delta\phi| < 1.57$) yield has been corrected to full jet yield assuming the jet shape in $\Delta\eta$ is the same as in $\Delta\phi$, the away side($|\Delta\phi| > 1.57$) has been corrected to the jet yield with in $|\Delta\eta| < 0.7$.

---

[2]Note that the background in trigger pion will not affect the jet width because they are mostly uncorrelated with jet.
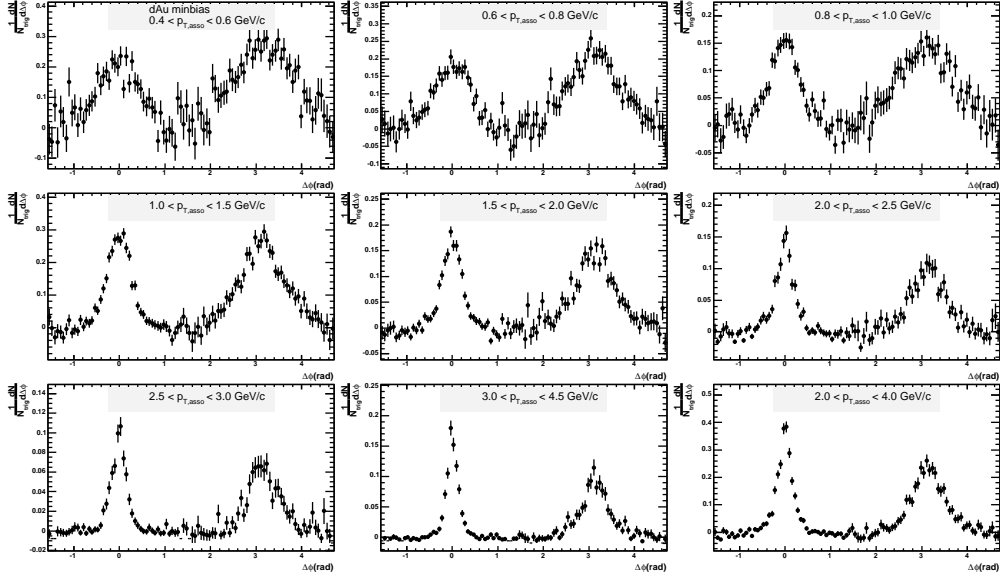
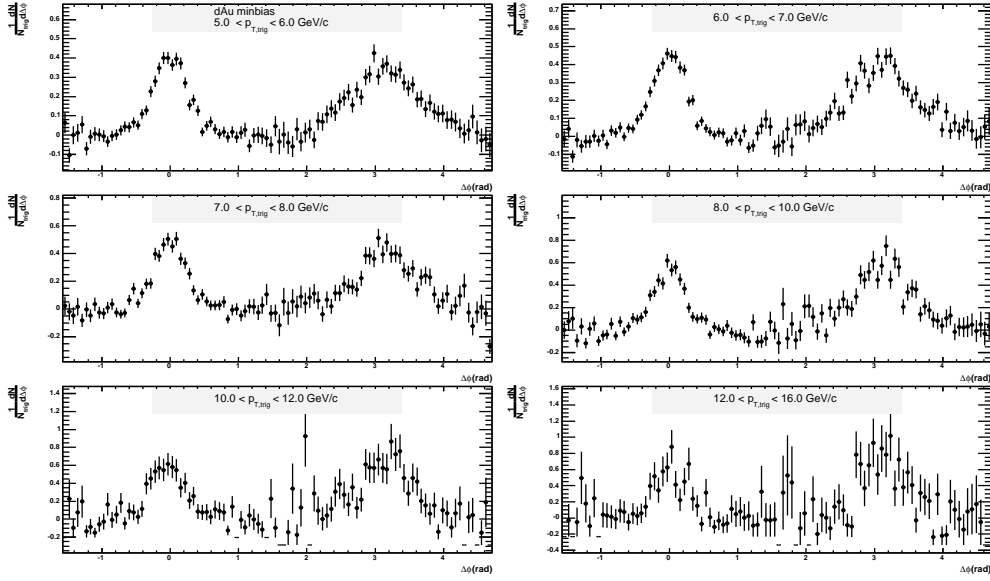Figure 52: The efficiency corrected $\frac{1}{N_{trig}}\frac{dN}{d\Delta\phi}$ distribution from $d - Au$ minimum collisions with trigger pions 5-10 GeV/c and 9 different associated charged hadron p_T ranges. The near side jet yield has been corrected to the full jet yield; while the away side jet yield has been corrected to $|\Delta\eta| < 0.7$.
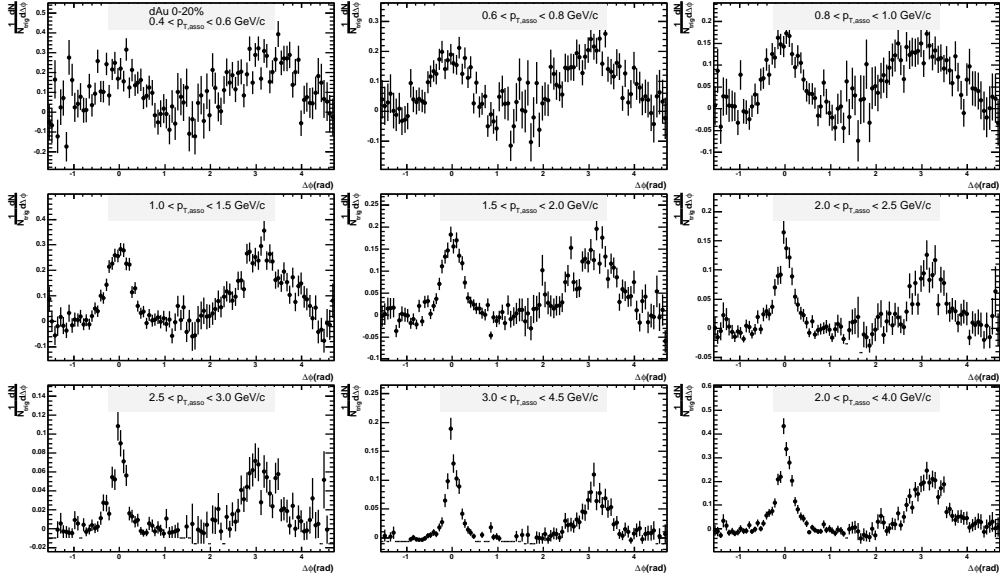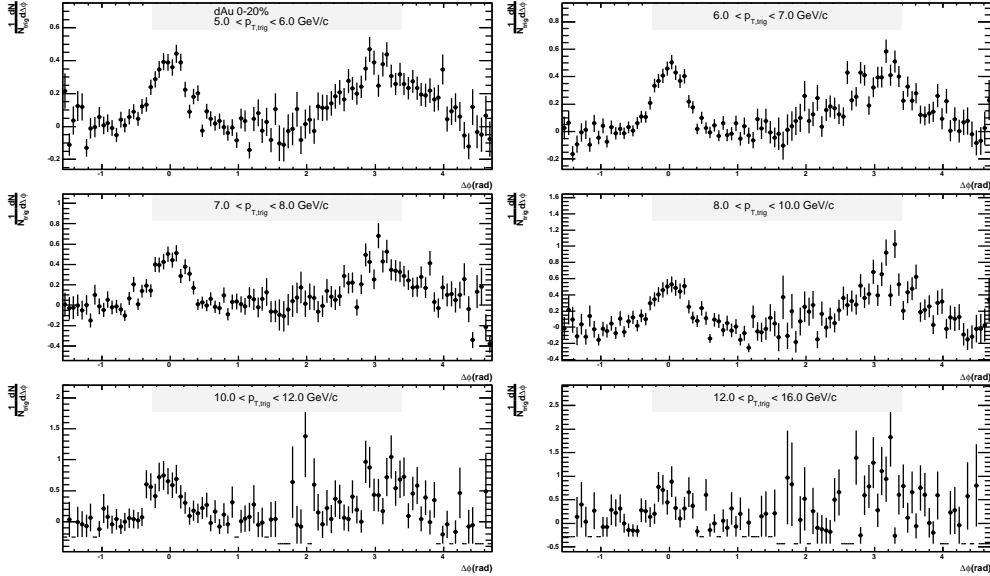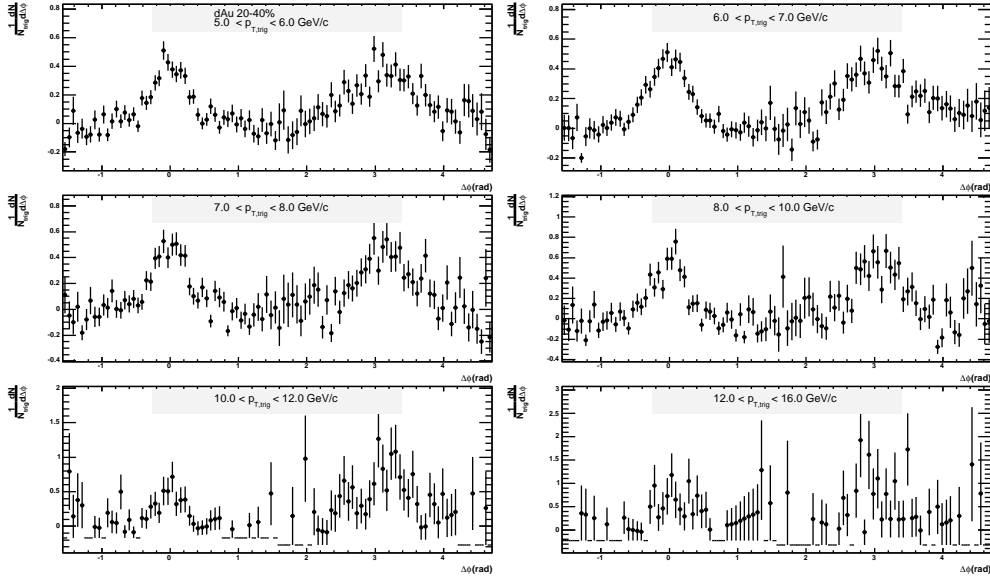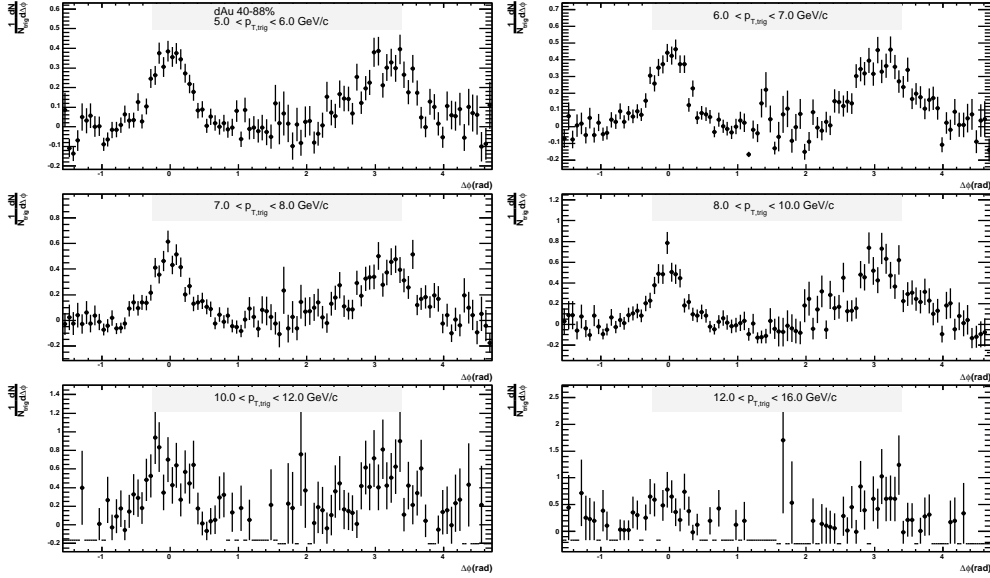

Figure 53: The efficiency corrected $\frac{1}{N_{trig}}\frac{dN}{d\Delta\phi}$ distribution from 0-20% $d - Au$ collisions with trigger pions 5-10 GeV/c and 9 different associated charged hadron p_T ranges. The near side jet yield has been corrected to the full jet yield; while the away side jet yield has been corrected to $|\Delta\eta| < 0.7$.
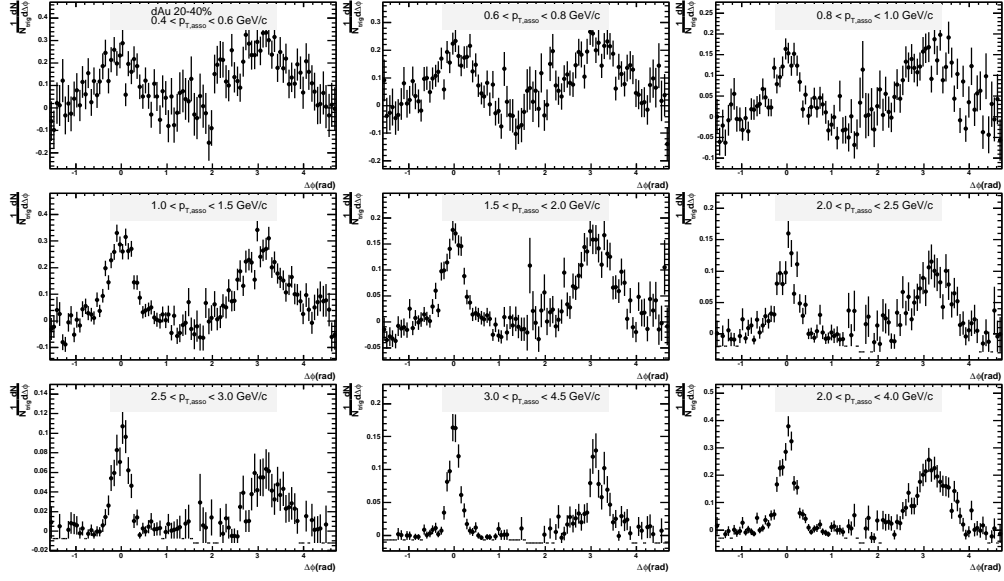
Figure 54: The efficiency corrected $\frac{1}{N_{trig}}\frac{dN}{d\Delta\phi}$ distribution from 20-40% $d-Au$ collisions with trigger pions 5-10 GeV/c and 9 different associated charged hadron p_T ranges. The near side jet yield has been corrected to the full jet yield; while the away side jet yield has been corrected to $|\Delta\eta| < 0.7$.
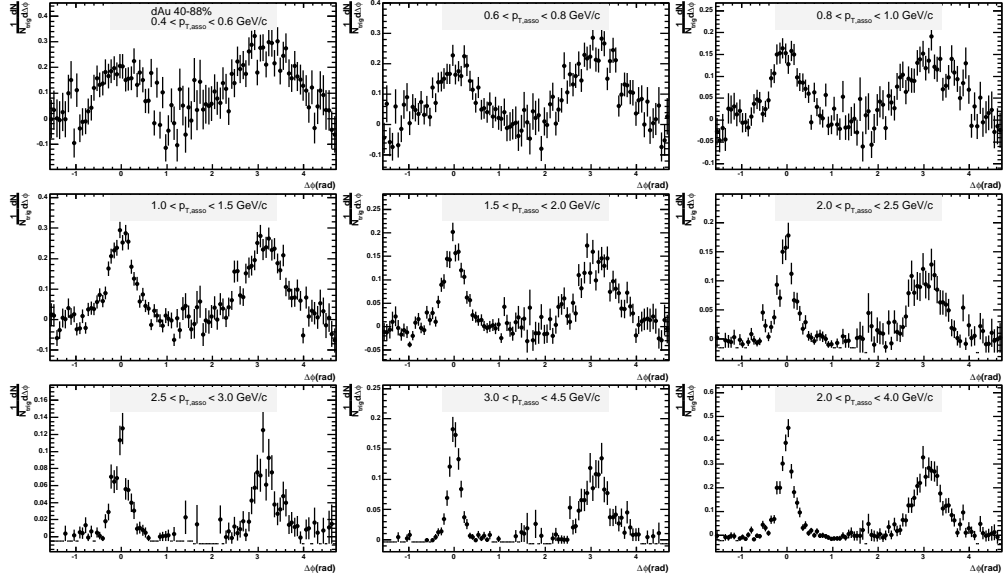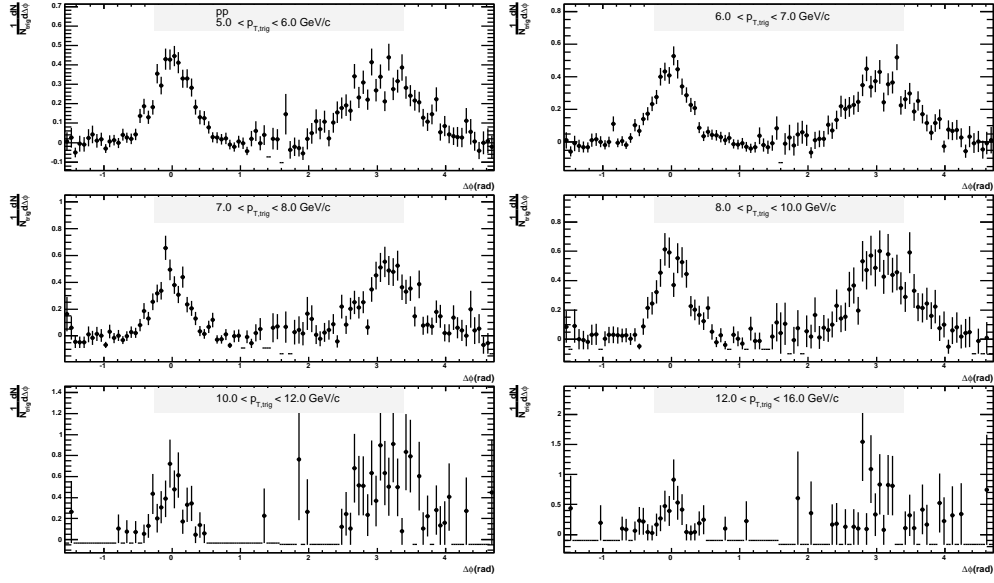

Figure 55: The efficiency corrected $\frac{1}{N_{trig}}\frac{dN}{d\Delta\phi}$ distribution from 40-88% $d-Au$ collisions with trigger pions 5-10 GeV/c and 9 different associated charged hadron p_T ranges. The near side jet yield has been corrected to the full jet yield; while the away side jet yield has been corrected to $|\Delta\eta| < 0.7$.
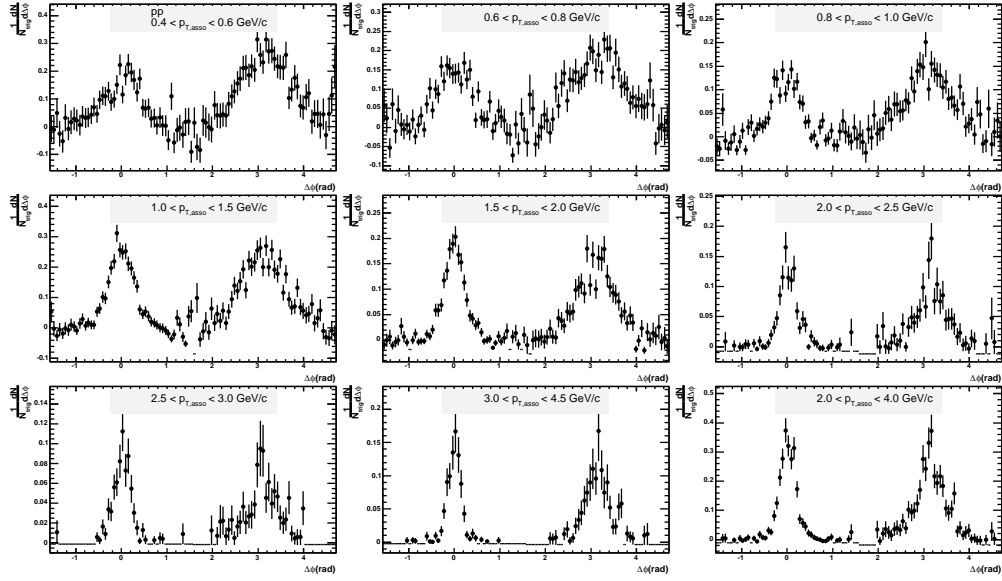
Figure 56: The efficiency corrected $\frac{1}{N_{trig}}\frac{dN}{d\Delta\phi}$ distribution from $p-p$ collisions with trigger pions 5-10 GeV/c and 9 different associated charged hadron p_T ranges. The near side jet yield has been corrected to the full jet yield; while the away side jet yield has been corrected to $|\Delta\eta| < 0.7$.

In addition, Fig.57-Fig.61 shows the efficiency corrected $\Delta\phi$ distribution with associated charged hadron $1 < p_T < 2$ GeV/c, for minimum bias, 0-20%, 20-40%, 40-88% $d-Au$ collisions and $p-p$ collisions, respectively. In each figure, the $\Delta\phi$ distribution were plotted for 6 different trigger pion p_T ranges: 5.0-6.0 GeV/c, 6.0-7.0 GeV/c, 7.0-8.0 GeV/c, 8.0-10.0 GeV/c, 10.0-12.0 GeV/c and 12.0-16.0 GeV/c.
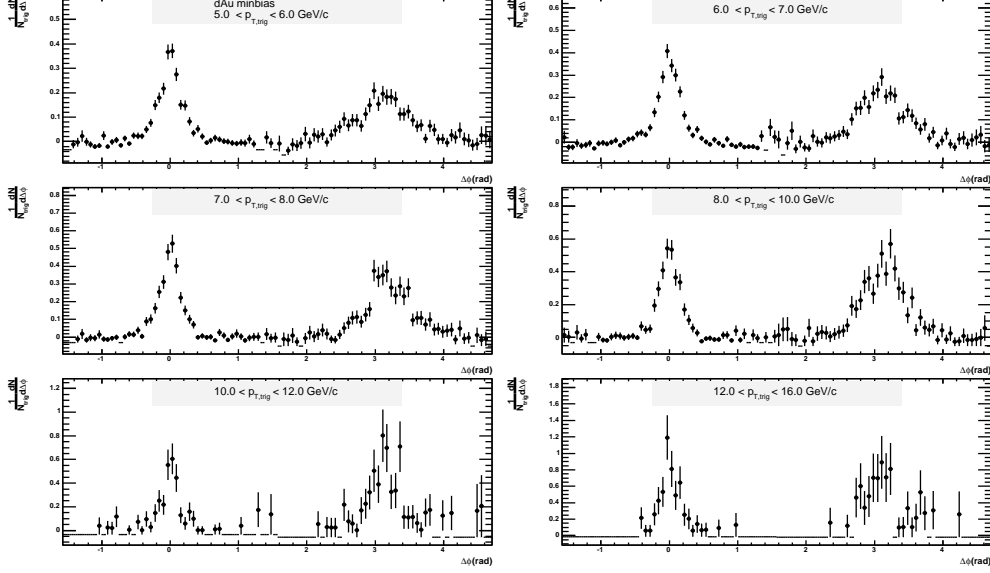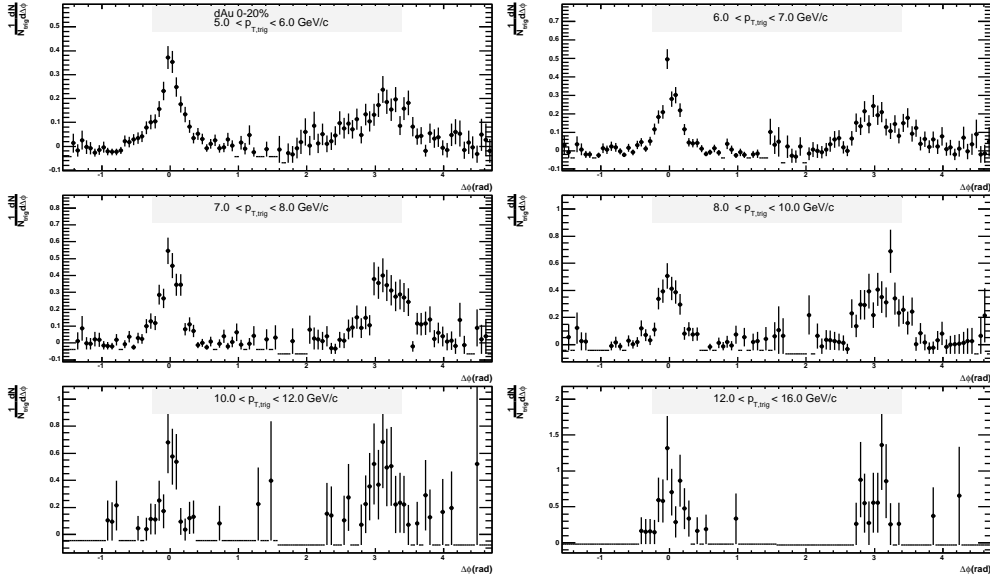
47

Figure 57: The efficiency corrected $\frac{1}{N_{trig}}\frac{dN}{d\Delta\phi}$ distribution from minimum bias $d-Au$ collisions with associated charged hadrons 1-2 GeV/c and 6 different trigger charged pion p_T ranges. The near side jet yield has been corrected to the full jet yield; while the away side jet yield has been corrected to $|\Delta\eta| < 0.7$.
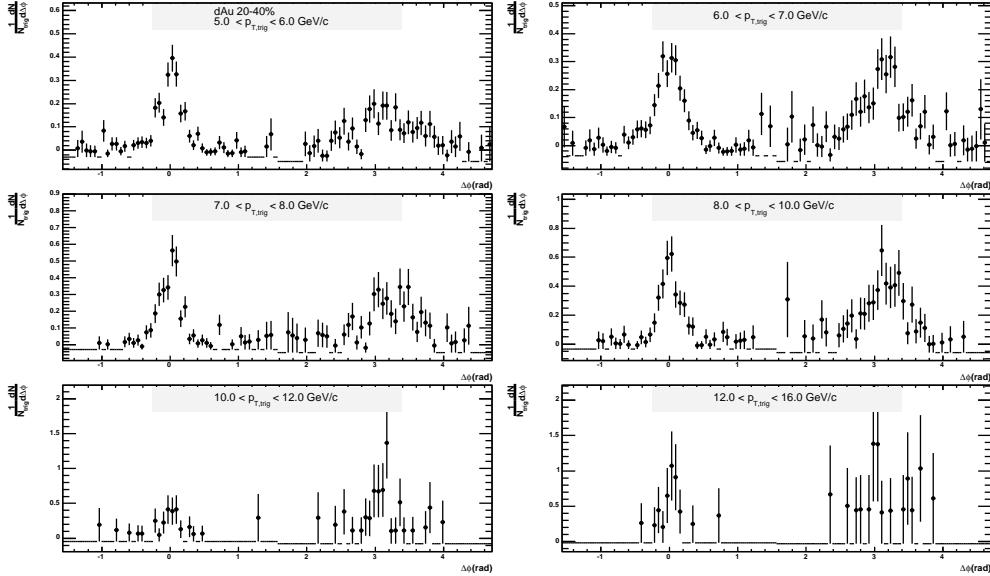

Figure 58: The efficiency corrected $\frac{1}{N_{trig}}\frac{dN}{d\Delta\phi}$ distribution from 0-20% $d-Au$ collisions with associated charged hadrons 1-2 GeV/c and 6 different trigger charged pion p_T ranges. The near side jet yield has been corrected to the full jet yield; while the away side jet yield has been corrected to $|\Delta\eta| < 0.7$.
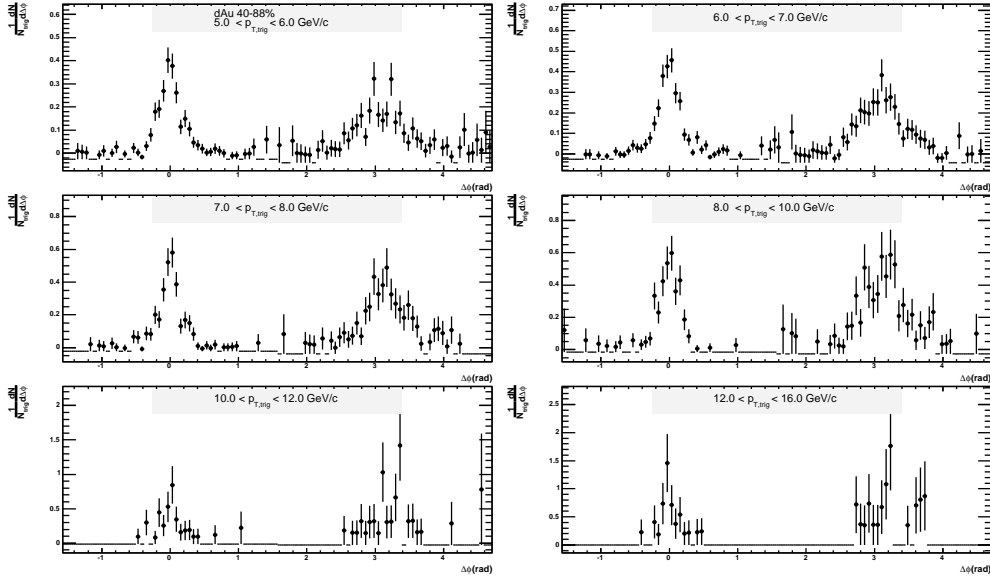
Figure 59: The efficiency corrected $\frac{1}{N_{trig}}\frac{dN}{d\Delta\phi}$ distribution from 20-40% $d - Au$ collisions with associated charged hadrons 1-2 GeV/c and 6 different trigger charged pion p_T ranges. The near side jet yield has been corrected to the full jet yield; while the away side jet yield has been corrected to $|\Delta\eta| < 0.7$.
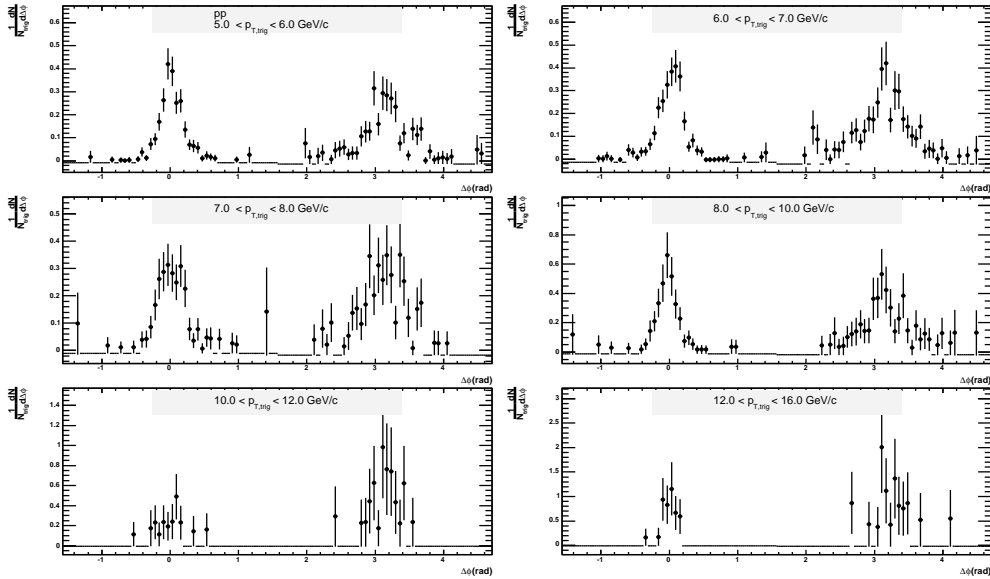

Figure 60: The efficiency corrected $\frac{1}{N_{trig}}\frac{dN}{d\Delta\phi}$ distribution from 40-88% $d - Au$ collisions with associated charged hadrons 1-2 GeV/c and 6 different trigger charged pion p_T ranges. The near side jet yield has been corrected to the full jet yield; while the away side jet yield has been corrected to $|\Delta\eta| < 0.7$.

49

Figure 61: The efficiency corrected $\frac{1}{N_{trig}}\frac{dN}{d\Delta\phi}$ distribution from $p-p$ collisions with associated charged hadrons 1-2 GeV/c and 6 different trigger charged pion p_T ranges. The near side jet yield has been corrected to the full jet yield; while the away side jet yield has been corrected to $|\Delta\eta| < 0.7$.

Then from Fig.62-Fig.66, we show the efficiency corrected $\Delta\phi$ distribution with associated charged hadron $2 < p_T < 4.5$ GeV/c, for minimum bias, 0-20%, 20-40%, 40-88% $d - Au$ collisions and $p - p$ collisions, respectively. In each figure, the $\Delta\phi$ distribution were plotted for 6 different trigger pion p_T ranges: 5.0-6.0 GeV/c, 6.0-7.0 GeV/c, 7.0-8.0 GeV/c, 8.0-10.0 GeV/c, 10.0-12.0 GeV/c and 12.0-16.0 GeV/c.

Figure 62: The efficiency corrected $\frac{1}{N_{trig}}\frac{dN}{d\Delta\phi}$ distribution from minimum bias $d - Au$ collisions with associated charged hadrons 2-4.5 GeV/c and 6 different trigger charged pion p_T ranges. The near side jet yield has been corrected to the full jet yield; while the away side jet yield has been corrected to $|\Delta\eta| < 0.7$.

Figure 63: The efficiency corrected $\frac{1}{N_{trig}}\frac{dN}{d\Delta\phi}$ distribution from 0-20% $d-Au$ collisions with associated charged hadrons 2-4.5 GeV/c and 6 different trigger charged pion p_T ranges. The near side jet yield has been corrected to the full jet yield; while the away side jet yield has been corrected to $|\Delta\eta| < 0.7$.

Figure 64: The efficiency corrected $\frac{1}{N_{trig}}\frac{dN}{d\Delta\phi}$ distribution from 20-40% $d-Au$ collisions with associated charged hadrons 2-4.5 GeV/c and 6 different trigger charged pion p_T ranges. The near side jet yield has been corrected to the full jet yield; while the away side jet yield has been corrected to $|\Delta\eta| < 0.7$.

Figure 65: The efficiency corrected $\frac{1}{N_{trig}}\frac{dN}{d\Delta\phi}$ distribution from 40-88% $d-Au$ collisions with associated charged hadrons 2-4.5 GeV/c and 6 different trigger charged pion p_T ranges. The near side jet yield has been corrected to the full jet yield; while the away side jet yield has been corrected to $|\Delta\eta| < 0.7$.

Figure 66: The efficiency corrected $\frac{1}{N_{trig}}\frac{dN}{d\Delta\phi}$ distribution from $p-p$ collisions with associated charged hadrons 2-4.5 GeV/c and 6 different trigger charged pion p_T ranges. The near side jet yield has been corrected to the full jet yield; while the away side jet yield has been corrected to $|\Delta\eta| < 0.7$.

6.2 p_T, x_E distribution

Fig.67-Fig.71 shows the p_T spectra with trigger pions $5 < p_T < 10$ GeV/c, for minimum bias, 0-20%, 20-40%, 40-88% $d - Au$ collisions and $p - p$ collisions, respectively. We have plotted the systematic errors due to the fit (in shaded band) and other errors (in boxes) separately.
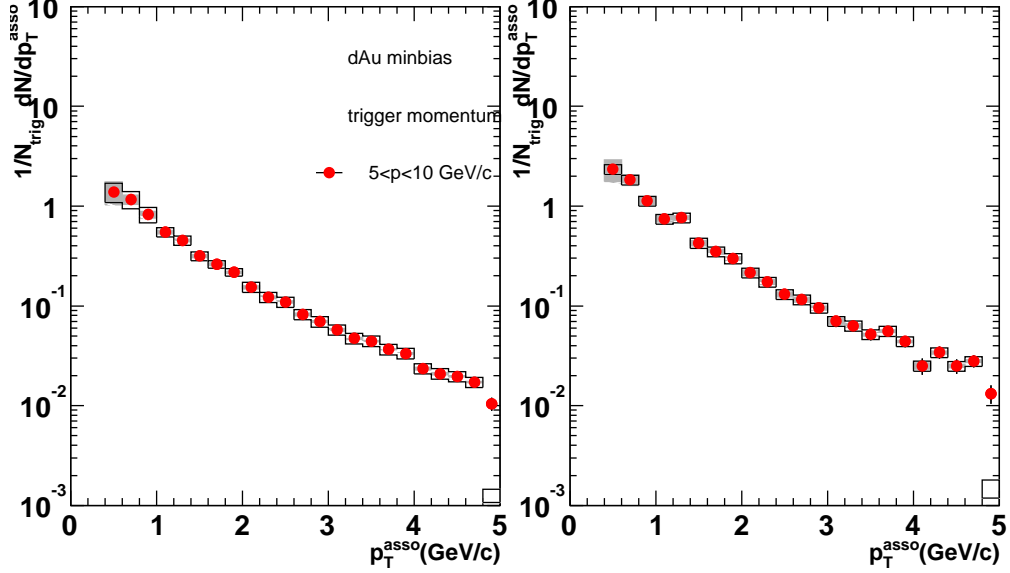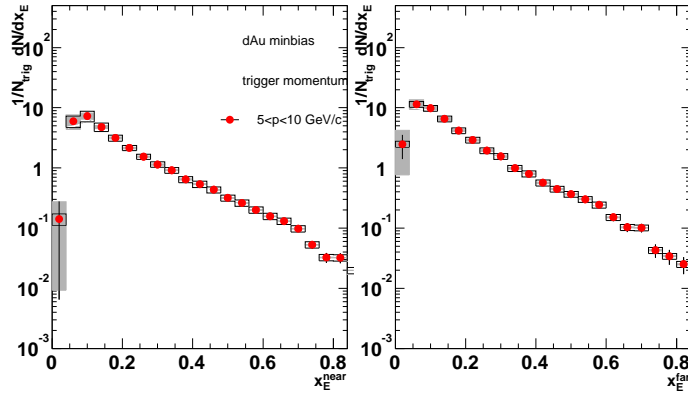

Figure 67: Near(left panel) and far(right panel) side CY for minimum bias $d - Au$ collisions as function of $p_{T,asso}$, trigger pion is from 5 to 10 GeV/c in p_T.
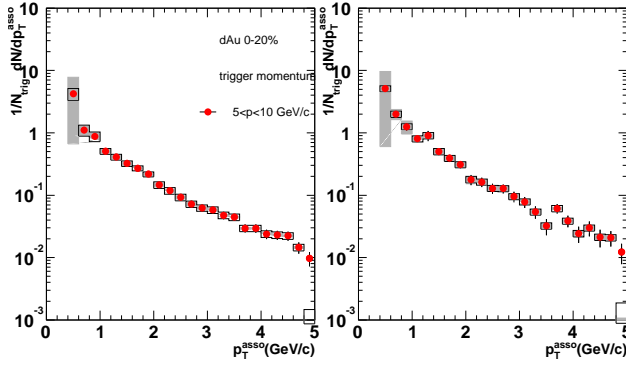
Figure 68: Near(left panel) and far(right panel) side CY for 0-20% most central $d - Au$ collisions as function of $p_{T,asso}$, trigger pion is from 5 to 10 GeV/c in p_T.
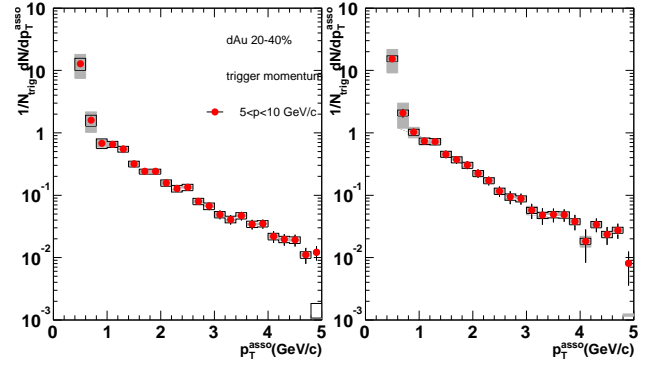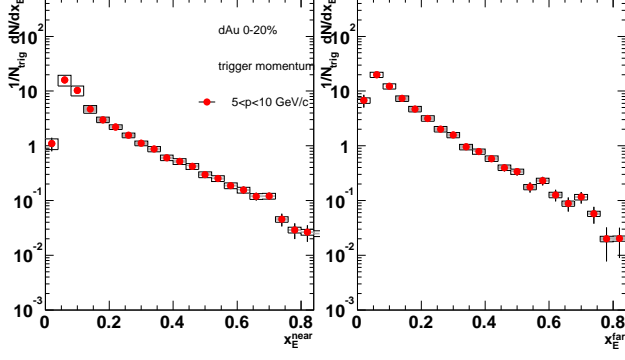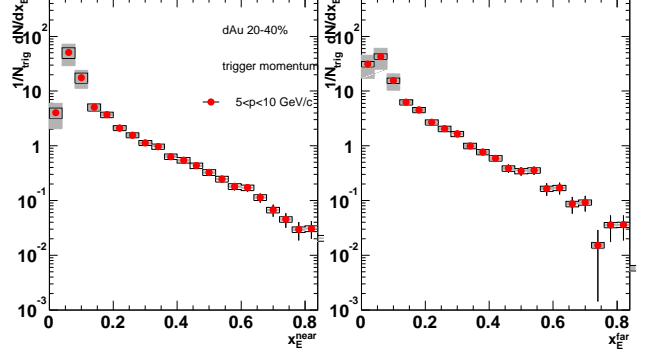
Figure 69: Near(left panel) and far(right panel) side CY for 20-40% $d - Au$ collisions as function of $p_{T,asso}$, trigger pion is from 5 to 10 GeV/c in p_T.

The corresponding x_E distribution is shown from Fig.6.2-Fig.76, as convention of this note, we always plot the away side x_E in negative axis unless specified otherwise.

Since $x_E = p_{T,asso}/p_{T,trig} cos(\Delta\phi)$, the x_E range depends on the trigger p_T. A better way to study the x_E distribution is to divide $p_{T,trig}$ in finer bins, which allows for more detailed

54
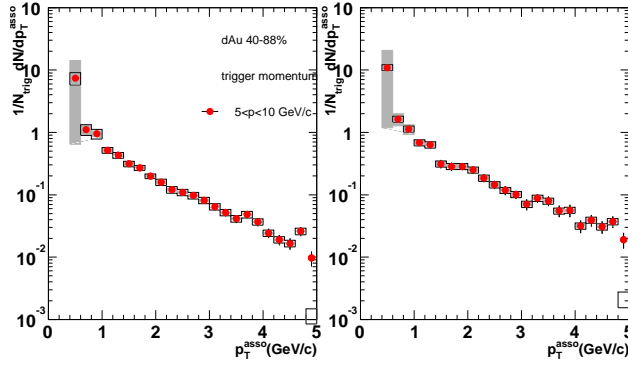
Figure 70: Near(left panel) and far(right panel) side CY for 40-88% $d - Au$ collisions as function of $p_{T,asso}$, trigger pion is from 5 to 10 GeV/c in p_T.
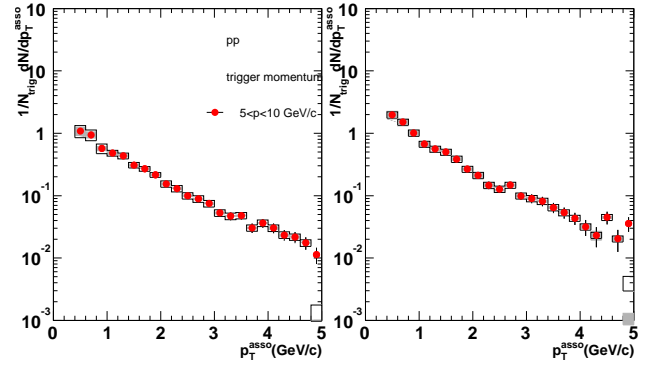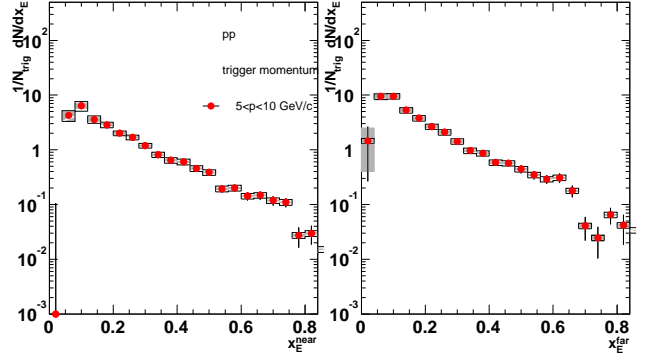

Figure 71: Near(left panel) and far(right panel) side CY for $p - p$ collisions as function of $p_{T,asso}$, trigger pion is from 5 to 10 GeV/c in p_T.
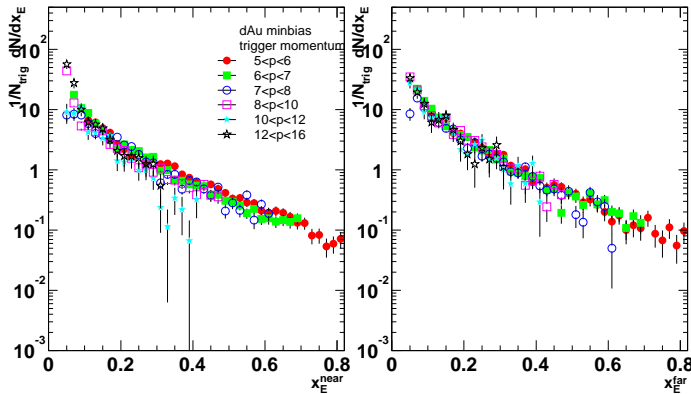

Figure 72: Near(left panel) and far(right panel) side CY for minimum bias $d - Au$ collisions as function of x_E, trigger pion is from 5 to 10 GeV/c in p_T.

study of the scale dependence.

The x_E distributions with five trigger p_T ranges are shown in Fig.6.2-81 for minimum bias, 0-20%, 20-40%, 40-88% $d - Au$ collisions and $p - p$ collisions, respectively. For each set of data points, the range of x_E is determined as $x_E^{max} = p_{T,asso}^{max}/p_{T,trig}^{max}, x_E^{min} = p_{T,asso}^{min}/p_{T,trig}^{min}$

Figure 73: Near(left panel) and far(right panel) side CY for 0-20% $d-Au$ collisions as function of x_E, trigger pion is from 5 to 10 GeV/c in p_T.

Figure 74: Near(left panel) and far(right panel) side CY for 20-40%$d-Au$ collisions as function of x_E, trigger pion is from 5 to 10 GeV/c in p_T.
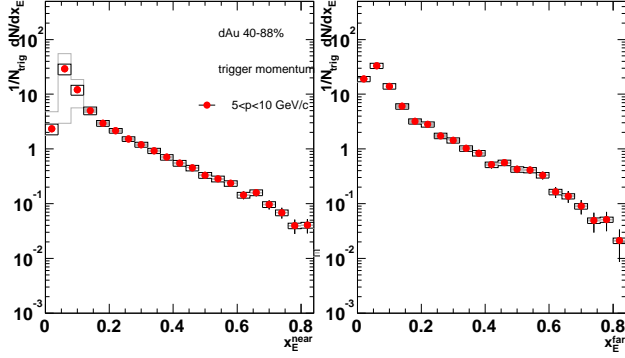
Figure 75: Near(left panel) and far(right panel) side CY for 40-88% $d-Au$ collisions as function of x_E, trigger pion is from 5 to 10 GeV/c in p_T.

Figure 76: Near(left panel) and far(right panel) side CY for $p-p$ collisions as function of x_E, trigger pion is from 5 to 10 GeV/c in p_T.

Figure 77: Near(left panel) and far(right panel) side CY for minimum bias $d-Au$ collisions as function of x_E, results for 5 different ranges of trigger pion are shown.
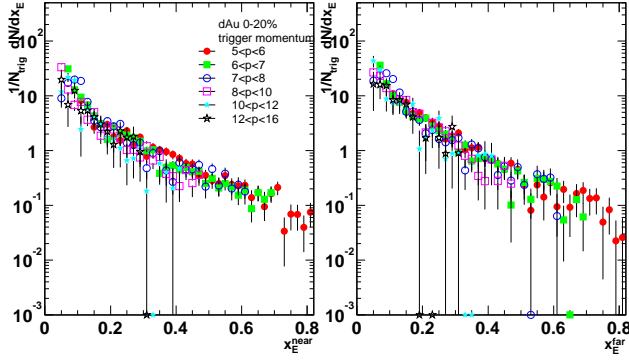
Figure 78: Near(left panel) and far(right panel) side CY for 0-20% $d - Au$ collisions as function of x_E, results for 5 different ranges of trigger pion are shown.
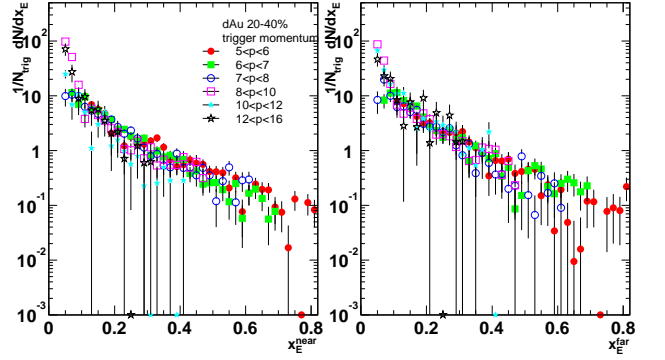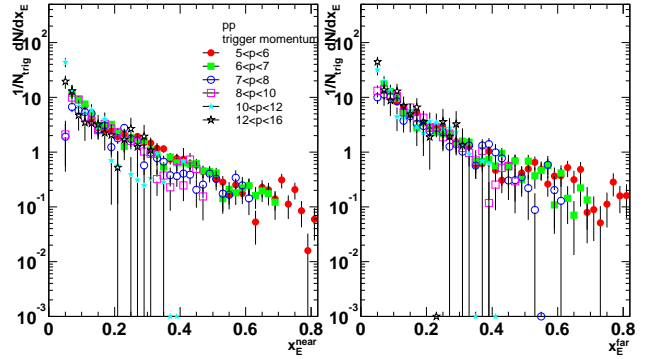

Figure 79: Near(left panel) and far(right panel) side CY for 20-40% $d - Au$ collisions as function of x_E, results for 5 different ranges of trigger pion are shown.
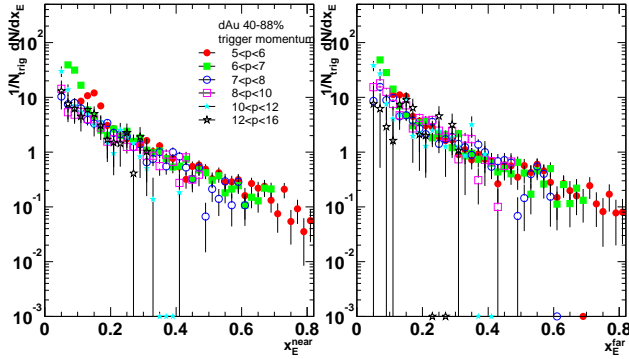
Figure 80: Near(left panel) and far(right panel) side CY for 40-88% $d - Au$ collisions as function of x_E, results for 5 different ranges of trigger pion are shown.

Figure 81: Near(left panel) and far(right panel) side CY for $p - p$ collisions as function of x_E, results for 5 different ranges of trigger pion are shown.

6.3 p_{out} distribution

We use the same statistical method discussed in section to extract p_{out} distribution. Fig.82 shows the near side(open symbols) and away side(filled symbols) p_{out} distribution for $5 < p_{T,trig} < 10$ GeV/c and $0.4 < p_{T,asso} < 4.5$ GeV/c. One see that the away side p_{out} distribution is broader than that for the near side, indicative of the contribution from k_T. However both curves have power law like tails at large p_{out}, which might be caused by the radiation contribution.
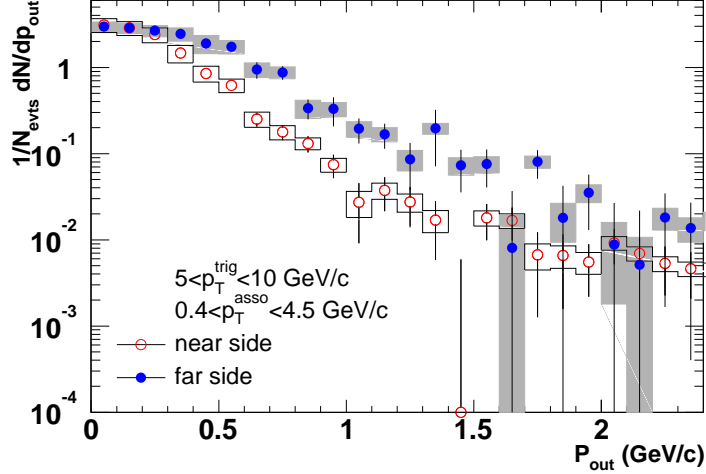
Figure 82: p_{out} distribution for $5 < p_{T,trig} < 10$ GeV/c and $0.4 < p_{T,asso} < 4.5$. The open and filled symbols represent the near side p_{out} and far side p_{out}, respectively.

The difference between same side and away side p_{out} distribution reflects the k_T broadening effects. The p_{out} distributions contain more information about di-jet correlation than the RMS value of j_T and k_T. Fig.83-85 shows the comparison of the p_{out} distribution between centrality selected $d - Au$ and $p - p$ collisions. The p_T ranges are $5 < p_{T,trig} < 10$ GeV/c and $0.4 < p_{T,asso} < 4.5$. No obvious difference is seen between the two.
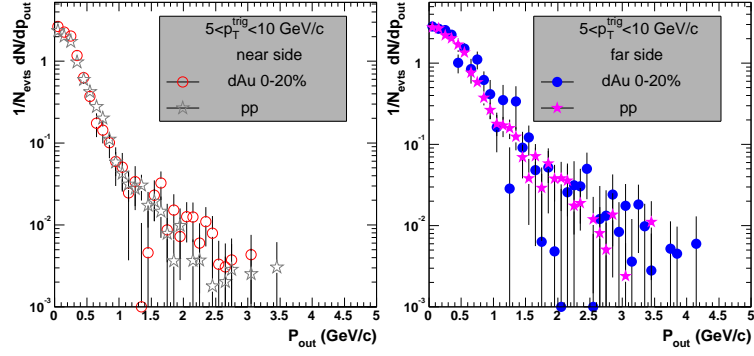
Figure 83: comparison of the p_{out} distribution between 0-20% central $d - Au$ and $p - p$ collisions.
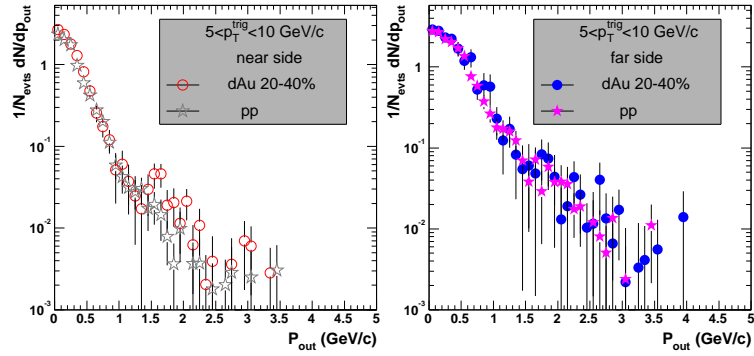

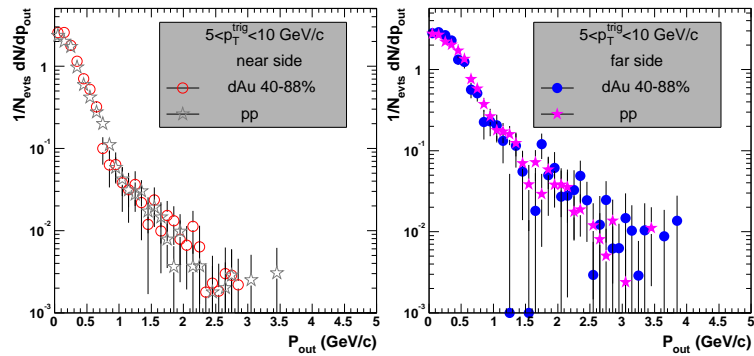Figure 84: comparison of the p_{out} distribution between 20-40% central $d - Au$ and $p - p$ collisions.

Figure 85: comparison of the p_{out} distribution between 40-88% central $d - Au$ and $p - p$ collisions.

6.4 width, j_T and zk_T distributions

Fig.86 shows the near side jet width, away side jet width, 1D RMS j_T and 1D RMS zk_T as function of $p_{T,asso}$ for trigger $5 < p_T < 10$ GeV/c for minimum bias $d - Au$ collisions. As we discussed in section, the rising trend of the zk_T as function of $p_{T,asso}$ is due to trigger bias. For completeness, Fig.87-90 show the results for centrality selected $d - Au$ and $p - p$ collisions.
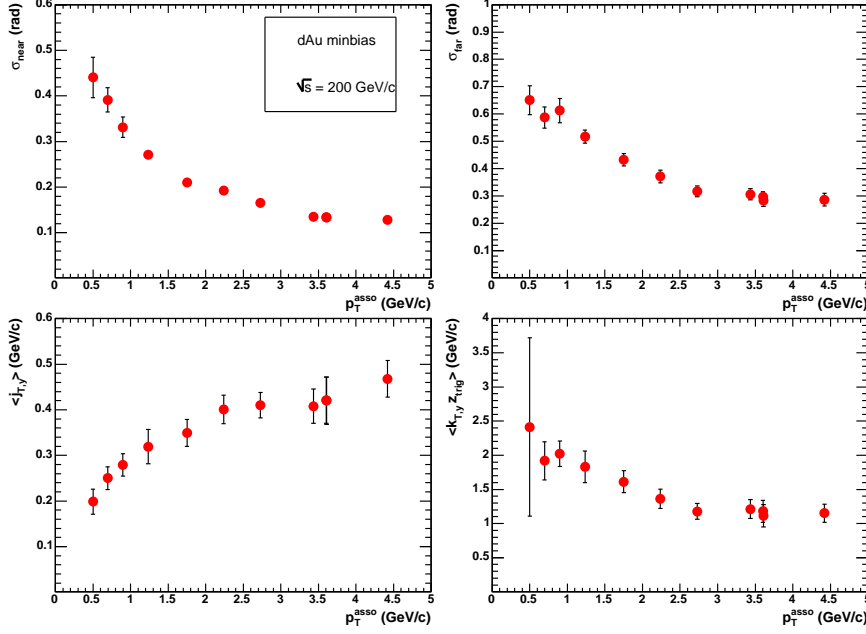
Figure 86: minimum bias $d - Au$, near side jet width(top left panel), far side jet width (top right panel), j_T 1D RMS value (bottom left panel) and zk_T 1D RMS values (bottom right panel) are shown as function of $p_{T,asso}$.
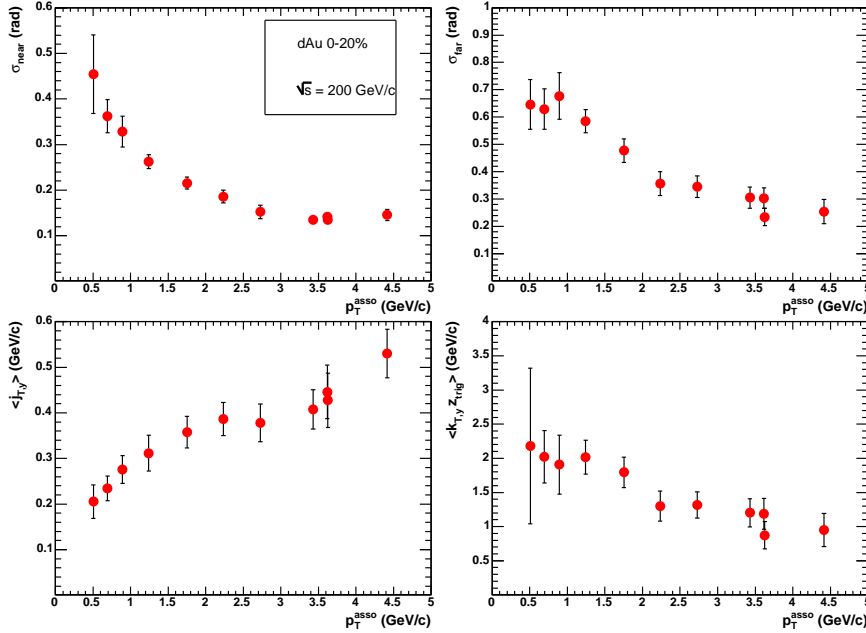
Figure 87: 0-20% $d - Au$, near side jet width(top left panel), far side jet width (top right panel), j_T 1D RMS value (bottom left panel) and zk_T 1D RMS values (bottom right panel) are shown as function of $p_{T,asso}$.

zk_T as function of trigger p_T reflects jet energy dependence. Our results are summarized in Fig.91-95
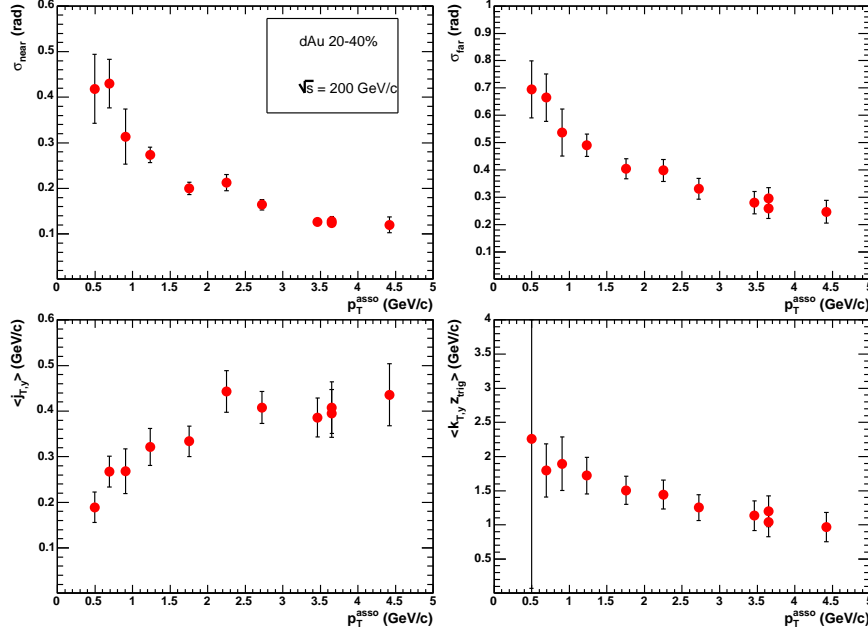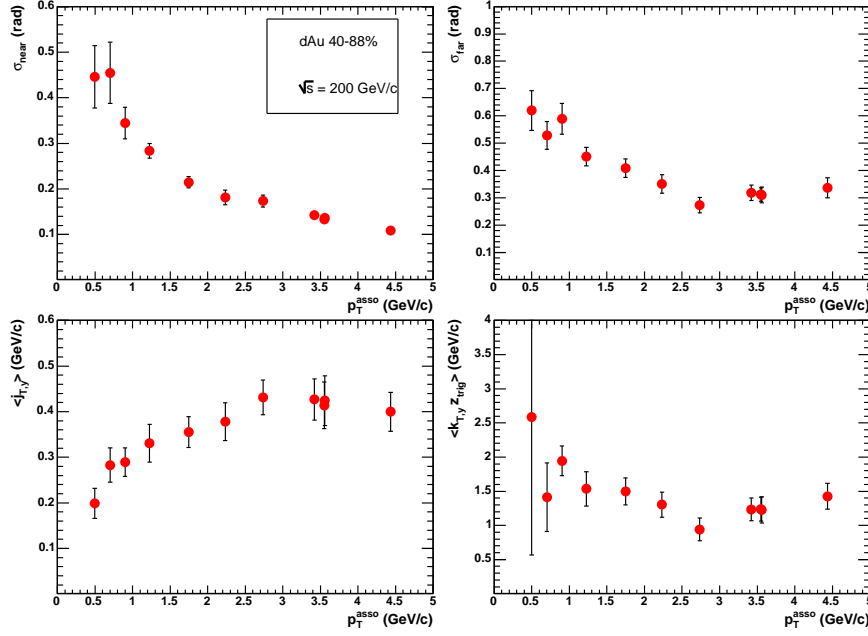
Figure 88: 20-40% $d - Au$, near side jet width(top left panel), far side jet width (top right panel), j_T 1D RMS value (bottom left panel) and zk_T 1D RMS values (bottom right panel) are shown as function of $p_{T,asso}$.
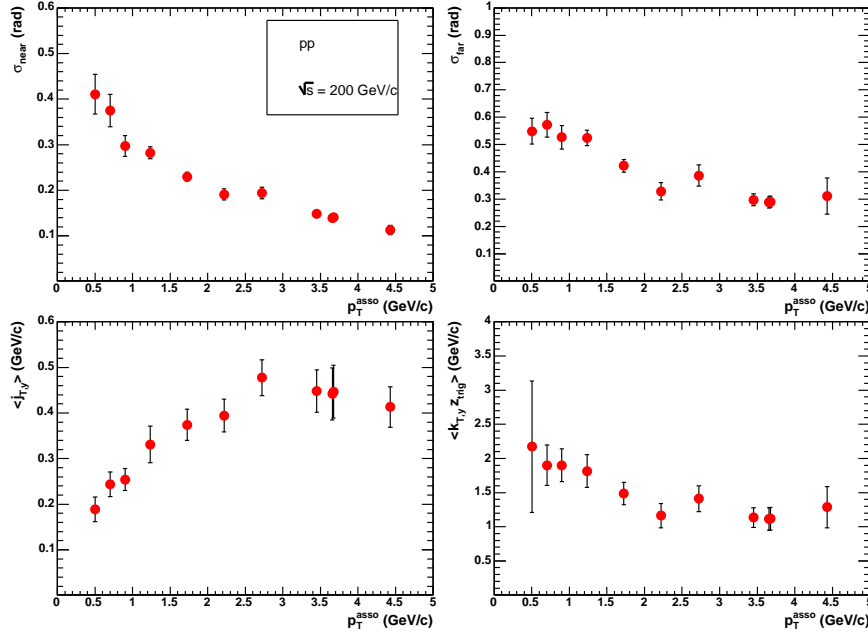

Figure 89: 40-88% $d - Au$, near side jet width(top left panel), far side jet width (top right panel), j_T 1D RMS value (bottom left panel) and zk_T 1D RMS values (bottom right panel) are shown as function of $p_{T,asso}$.
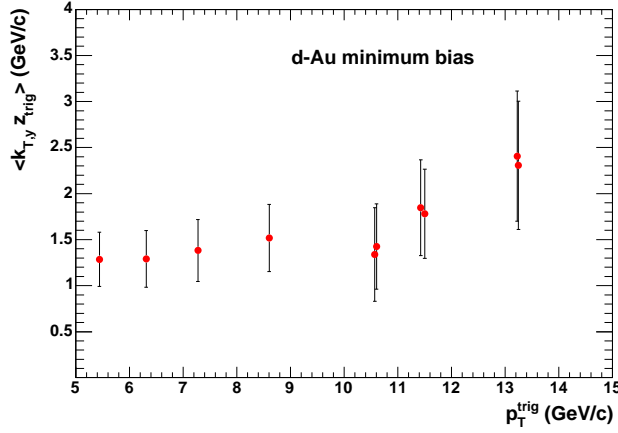
Figure 90: $p-p$, near side jet width(top left panel), far side jet width (top right panel), j_T 1D RMS value (bottom left panel) and zk_T 1D RMS values (bottom right panel) are shown as function of $p_{T,asso}$.

Figure 91: Minimum bias $d-Au$, zk_T 1D RMS value as function of trigger p_T. Associated particle p_T range is fixed at 2-4.5 GeV/c.
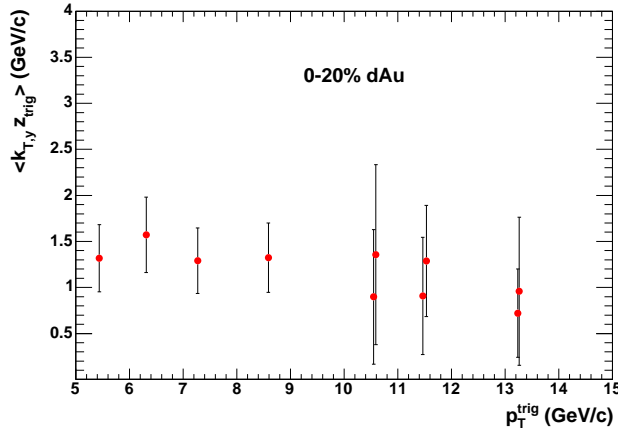

Figure 92: 0-20% $d-Au$, zk_T 1D RMS value as function of trigger p_T. Associated particle p_T range is fixed at 2-4.5 GeV/c.
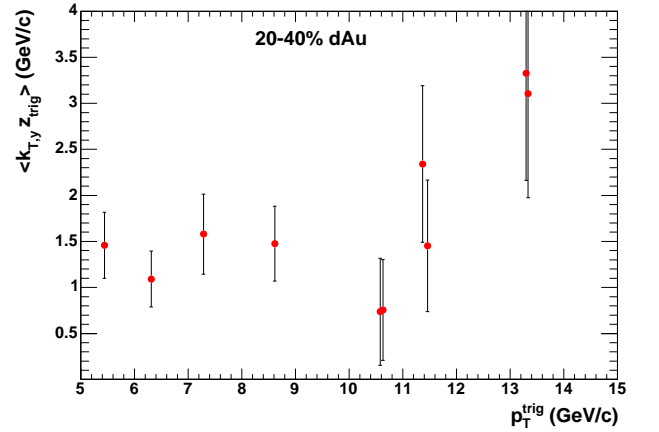
Figure 93: 20-40% $d-Au$, zk_T 1D RMS value as function of trigger p_T. Associated particle p_T range is fixed at 2-4.5 GeV/c.
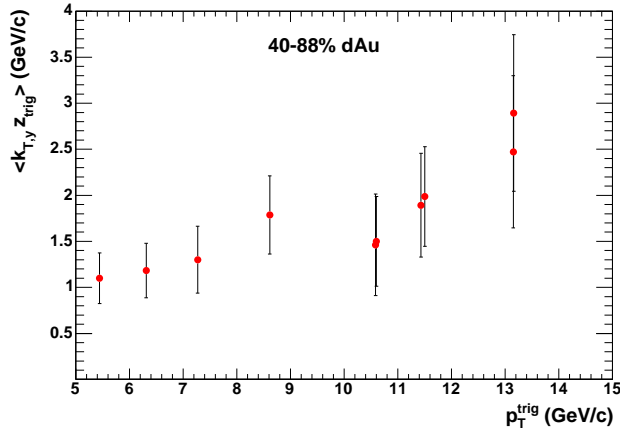
Figure 94: 40-88% $d - Au$, zk_T 1D RMS value as function of trigger p_T. Associated particle p_T range is fixed at 2-4.5 GeV/c.
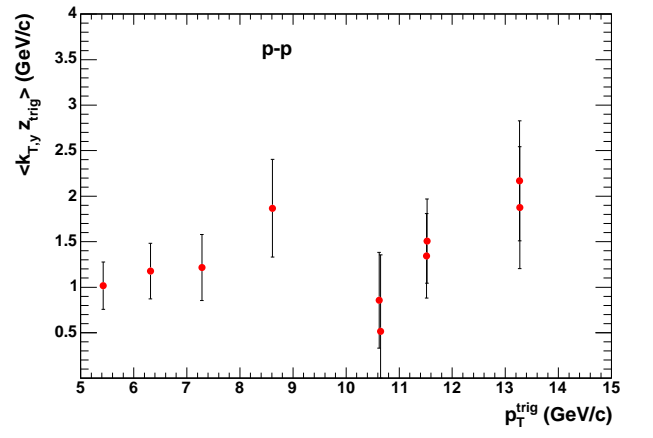

Figure 95: $p - p$, zk_T 1D RMS value as function of trigger p_T. Associated particle p_T range is fixed at 2-4.5 GeV/c.

63

6.5 Derived quantities

6.5.1 Jet multiplicity

6.5.2 Scaling plot

A better way to quantify the scaling behavior of the CY is to plot the CY as function of trigger p_T for a given x_E range. This is shown in Fig.96.
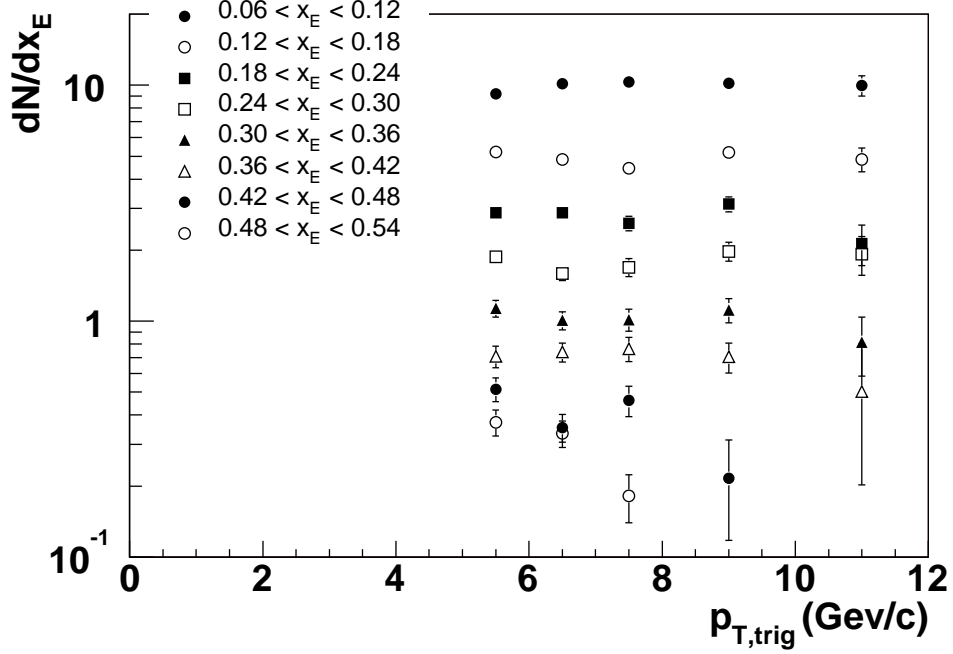

Figure 96: The trigger p_T dependence of the CY for various ranges of x_E for minimum bias $d - Au$ collisions.

6.6 $\langle z \rangle$ correction and k_T

The $\langle z \rangle$ correction has been derived by Nathan, Fig.97 shows the $\langle z \rangle$ as function of associated p_T (left) and trigger p_T (right) respectively. We use this correction to correct and derive the $(k_{T,y})_{RMS}$. An example is shown in Fig.98.
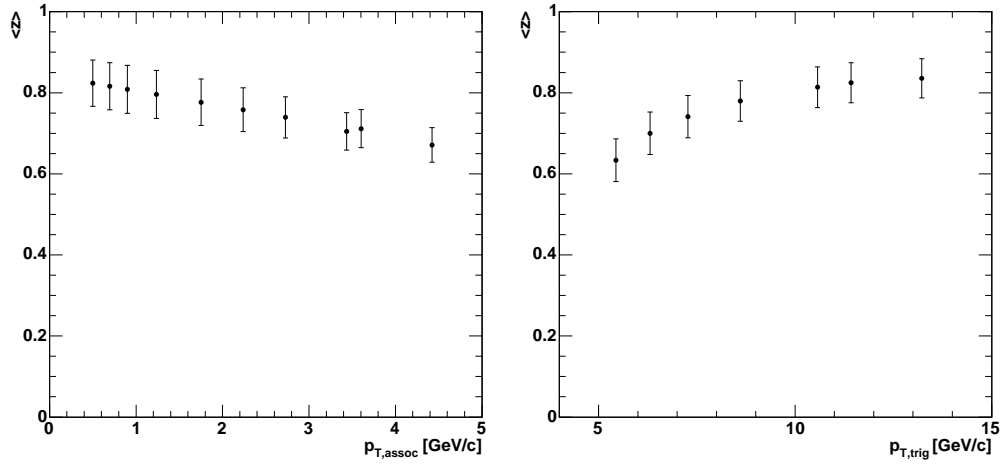
Figure 97: Left: $\langle z \rangle$ as function of associated p_T for trigger in $5 < p_{T,trig} < 10$ GeV/c. Right: $\langle z \rangle$ as function of trigger p_T for associated particle in $2 < p_{T,trig} < 2.5$ GeV/c.
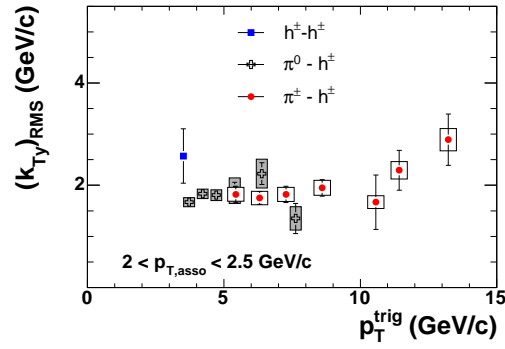

Figure 98: The $(k_{T,y})_{RMS}$ as function of trigger p_T for $\pi^{\pm} - h$ correlation (red) and $\pi^0 - h$ correlation (crosses).

References

[1] Analysis note 311, Jiangyong Jia and Brian Cole "R_{cp} for charged high p_T pions in $d - Au$ collisions at $sqrts_{NN} = 200$ GeV ".

[2] Analysis note 312, Jiangyong Jia and Brian Cole "Calculating $(j_T)_{RMS}$, $(k_T)_{RMS}$ from two particle correlations in $d - Au$ and $p - p$"

[3] Analysis note 313, Jiangyong Jia and Brian Cole "Mathematical framework on correlation function and conditional yield in $d - Au$ and $p - p$".

[4] Analysis note 202, J. Jia, S. Leckey, S. Milov, M. Reuter, A. Sickles, A. Drees, T. Hemmick, B. Jacak , Inclusive Charged Hadron p_T distribution in $d - Au$ collisions.

[5] Analysis note 276, J. Jia. K. Okada,Inclusive Charged Hadron Cross Section Measurement in Run2 $p - p$.

[6] A. Sickles, B. Jacak, M. Reuter, T. Hemmick "Conditional Yields with Identified Leading Particles in dAu and AuAu".

[7] M. Reuter, B. Jacak, A. Sickles, T. Hemmick, F. Matathias , "Conditional Yields for h-h Azimuthal Correlations in Au+Au and d+Au at 200 GeV"

[8] Analysis note 210, A.Drees, T.Hemmick, B.Jacak, J.Jia, S.Leckey, A.Milov, M.Reuter, A.Sickles, R.Soltz, Centrality determination and p_T centrality dependency in $d - Au$ collisions.

[9] S. Leckey, Centrality dependency of charged hadron production in $d - Au$, under preparation.

[10] Jan Rak /phenix/WWW/p/draft/rak/ppg029/note.ps; Jan Rak's final ananote for ppg029, to be published.

[11] analysis note 329, Nathan's note on $\pi^0 - h$ correlation.

[12] Jiangyong Jia http://www.phenix.bnl.gov/WWW/publish/jjia/2004/qm2004/qm2004.ppt; Nathan Grau http://www.phenix.bnl.gov/WWW/publish/ncgrau/QM04/QM04Poster.ppt; Paul Constantin http://www.phenix.bnl.gov/WWW/publish/pcon/QM04Poster.ppt.

[13] PPG29.

[14] W.G. Holzmann et. al, Two Particle Azimuthal Correlation Functions for Au-Au Collisions at $\sqrt{s_{NN}} = 200$ GeV